



저작자표시-비영리-변경금지 2.0 대한민국

이용자는 아래의 조건을 따르는 경우에 한하여 자유롭게

- 이 저작물을 복제, 배포, 전송, 전시, 공연 및 방송할 수 있습니다.

다음과 같은 조건을 따라야 합니다:



저작자표시. 귀하는 원저작자를 표시하여야 합니다.



비영리. 귀하는 이 저작물을 영리 목적으로 이용할 수 없습니다.



변경금지. 귀하는 이 저작물을 개작, 변형 또는 가공할 수 없습니다.

- 귀하는, 이 저작물의 재이용이나 배포의 경우, 이 저작물에 적용된 이용허락조건을 명확하게 나타내어야 합니다.
- 저작권자로부터 별도의 허가를 받으면 이러한 조건들은 적용되지 않습니다.

저작권법에 따른 이용자의 권리는 위의 내용에 의하여 영향을 받지 않습니다.

이것은 [이용허락규약\(Legal Code\)](#)을 이해하기 쉽게 요약한 것입니다.

[Disclaimer](#)

Doctor of Philosophy

**THERMOELECTRIC TRANSPORT PROPERTIES
OF LAYERED CHALCOGENIDES: CuAgSe, α -In₂Se₃, AND β -InSe**

**THE GRADUATE SCHOOL
OF THE UNIVERSITY OF ULSAN**

**Department of Physics
Nguyen, Thi Huong**

**THERMOELECTRIC TRANSPORT PROPERTIES
OF LAYERED CHALCOGENIDES: CuAgSe, α -In₂Se₃, AND β -InSe**

Supervisor: Prof. Sunglae Cho

A DISSERTATION

**Submitted to the Graduate School
In partial fulfillment of the Requirements
for the Degree of**

Doctor of Philosophy

Field of Physics

by

Nguyen, Thi Huong

**Department of Physics, University of Ulsan
Ulsan, Korea
November 2020**

**THERMOELECTRIC TRANSPORT PROPERTIES
OF LAYERED CHALCOGENIDES: CuAgSe, α -In₂Se₃, AND β -InSe**

This certifies that the dissertation

of Thi Huong Nguyen is approved.

Professor Soon-Cheol Hong, Soon Cheol Hong

Committee Chairman.

Professor Yong-Soo Kim, Kim Yong Soo

Committee Member.

Professor SuDong Park, SD Park

Committee Member.

Professor Jungdae Kim, Jungdae Kim

Committee Member.

Professor Sunglae Cho, Sunglae Cho

Committee Member.

Department of Physics

University of Ulsan, Ulsan, Korea

December 2020

Acknowledgments

First and foremost, I would like to express my sincere gratitude to my advisor, Professor Sunghae Cho, for giving me generous guidance, expert advice through all stages of this research and growing into a research scientist over the years.

I would like to thank all Professors in the Department of Physics, the University of Ulsan, who have lectured me and helped me during my Ph.D. period.

I would like to thank Professor Sudong Park, Dr. Jong Ho Park, and Dr. Ji Eun Lee (Korea Electrotechnology Research Institute) for their time and effort to help me with thermoelectric measurements. I would like to thank Professor Jungdae Kim and Ms. Thi Ly Trinh for their efforts and discussions on STM experiments. I also appreciated Professor Jong-Soo Rhyee and Ms. Song Yi Back (Kyung Hee University) for their time and effort to help me with heat capacity measurements.

I would like to especially thank Dr. Van Quang Nguyen as a teacher and brother, who teaches me to run the machine, discuss the results, and encourage me. I would also like to thank all lab-members for their help in growing, measuring samples, and sharing knowledge. All my friends are also thanked for all their encouragement.

Finally, I would like to thank my husband, Dr. Dac Dung Truong, for his encouragement and understanding. I would like to thank my grandparents, parents, sisters, and brothers, who always encourage me and help me take care of my lovely son, Dac Gia Bao Truong (Tom).

This work was supported by the National Research Foundation of Korea [NRF-2014R1A4A1071686], [NRF-2019R1F1A1058473 and NRF-2019R1A6A1A11053838].

Abstract

Due to the urgency of our energy and environmental issues, a variety of cost-effective and pollution-free technologies have attracted considerable attention, among which thermoelectric technology has made enormous progress. Thermoelectric modules interconvert heat energy and electrical energy, work without mechanical movement, safe, low cost, and environmentally friendly green technology. The efficiency of these devices is still very low due to the limit of the thermoelectric figure of merit ZT of the material. In addition to the hundred years' history of thermoelectric research, many efforts have been made to improve the efficiency of thermoelectric devices by improving the thermoelectric figure of merit ZT of materials. Unfortunately, the strong coupling between material parameters that determine thermoelectric efficiency, namely the Seebeck coefficient S , electrical conductivity σ , and thermal conductivity κ , complicates the optimization of thermoelectric energy converters. To optimize these parameters for maximizing ZT , band engineering, complex crystal, nano-structures, nano-wire, nano-tube, superlattices approaches have been made aiming at the phonon glass electron crystal and phonon liquid electron crystal concepts. However, with persistent efforts, the number of thermoelectric materials has been dramatically increased over the last two decades. Layered chalcogenide (group VI: S, Se, Te) semiconductors have been more and more attention in a variety of energy applications, including solar cells, phase change memory, thermoelectric energy conversion. For applications in thermoelectric energy converters, layered chalcogenides have many advantages, for instance, reducing thermal conductivity with weak van der Waals bonding and heavy atomic weight, possessing a variety of structures, easily doped into p-type or n-type, and low operating costs. CuAgSe is a layered chalcogenide material that is also a robust candidate for the phonon liquid-

like crystal concept with relatively high p-type and n-type ZT values (0.95 and 0.70, respectively). The stoichiometric CuAgSe has always been reported to show n-type conduction, while the p-type conduction is only present in the non-stoichiometric CuAgSe. However, it is difficult to synthesize the non-stoichiometric p-type CuAgSe without secondary phases. In 2009, single-crystalline and polycrystalline In_4Se_3 materials were reported with a high ZT of 1.53 at 425 °C and 1.4 at 460 °C. The physical properties of indium selenides were primarily determined by their intrinsic structural characteristics such as their composition, phase, crystal structure, and structural imperfections. From a structural point of view, indium selenides belong to a complex system with different stoichiometric ratios such as In_4Se_3 , In_2Se_3 , InSe , In_6Se_7 , and In_3Se_4 . However, the thermoelectric properties of In_2Se_3 and InSe single crystal have not been thoroughly investigated at low temperatures. In this study, the thermoelectric transport properties of the single-phase undoped, and Ni-, Co-, and Zn-doped poly-crystalline CuAgSe and the single-crystalline $\alpha\text{-In}_2\text{Se}_3$ and $\beta\text{-InSe}$, which were grown by using the temperature gradient technique, were carried out. The carrier control in CuAgSe by growth process or doping was achieved. The maximum ZT value of 0.69 (0.56) at 623 K (673 K) in undoped n-type (p-type) CuAgSe was obtained. Zn is a promising dopant for n-type CuAgSe with a ZT value of 0.68 at 623 K. Additionally, the huge anisotropy during transport of $\alpha\text{-In}_2\text{Se}_3$ single crystals were observed due to the anisotropic activation energy and anisotropic mobility between two directions. The $\beta\text{-InSe}$ single-crystal exhibited an instability characteristic, which can be modified by thermal energy and potential energy.

Approved: _____

Professor Sunghae Cho

Contents

Acknowledgments	i
Abstract	ii
Contents	iv
List of Tables	viii
List of Figures	ix
Chapter 1. Introduction	1
1.1 Description of the research.....	1
1.2 List of publications.....	4
1.3 References.....	5
Chapter 2. Background	8
2.1 Physical phenomena of thermoelectricity.....	8
2.1.1 The Seebeck effect.....	8
2.1.2 The Peltier effect.....	10
2.1.3 The Thomson effect.....	11
2.1.4 Kelvin relation.....	13
2.1.5 Thermoelectric figure of merit.....	14
2.2 Thermoelectric devices.....	15

2.2.1 Thermoelectric module	15
2.3 Thermoelectric material research	18
2.3.1 Brief thermoelectricity of layered chalcogenides.....	18
2.3.2 Overview of CuAgSe.....	20
2.3.3 Overview of In ₂ Se ₃	21
2.3.4 Overview of InSe	23
2.4 References	25
Chapter 3. Experiments	32
3.1 PID temperature controller	32
3.2 Heat transfer mechanism	33
3.3 Single crystal growth.....	35
3.3.1 Bridgman technique (Bridgman-Stockbarger technique)	35
3.3.2 Temperature gradient technique.....	38
3.4 Transport properties measurement system in our lab.....	39
3.4.1 Low-temperature measurement system.....	39
3.4.2 High-temperature measurement system	42
3.5 Characterizations	42
3.5.1 X-ray diffraction (XRD).....	42
3.5.2 Scanning Tunneling Microscope(STM).....	44
3.5.3 Raman spectroscopy	45

3.5.4 Photoluminescence (PL)	46
3.5.5 Specific heat capacity	47
3.5.6 Thermal diffusivity and thermal conductivity: LFA, ZEM 3.....	48
3.6 Measurement's errors	49
3.6.1 Electrical conductivity measurement's errors	50
3.6.2 Seebeck coefficient measurement's errors	51
3.6.3 Thermal conductivity measurement's errors	52
3.6.4 Power factor's errors	52
3.6.5 Figure of merit's error	53
3.6.6 Errors of ZEM 3	53
3.7 References	53
Chapter 4. Carrier control in CuAgSe by growth process or doping	55
4.1 Introduction	55
4.2 Experiments	58
4.3 Results and discussion	59
4.4 Conclusions	70
4.5 References	70
Chapter 5. Huge anisotropy transport properties in α-In₂Se₃ single crystal.....	74
5.1 Introduction	74
5.2 Experiments	76

5.3 Results and discussion.....	77
5.4 Conclusion.....	87
5.5 Supplementary figures.....	87
5.6 References.....	87
Chapter 6. Growth & Un-stability characteristic of β-InSe single crystal.....	92
6.1 Introduction.....	92
6.2 Experimental.....	94
6.3 Results.....	96
6.4 Conclusion.....	103
6.5 Supplementary figures.....	104
6.6 References.....	104
Chapter 7. Conclusions.....	109

List of Tables

Table 2.1 Temperature ranges for materials considered for segmentation in a typical p-leg with their respective compatibility factors[3].	18
Table 4.1 The soaking time and room temperature electrical conductivity, carrier density, and carrier mobility for all samples.	59
Table 4.2 Lattice parameters of CAS-1, CAS-2, CAS-3, and Ni-, Co-, Zn-doped CAS-2 samples.	60

List of Figures

Fig. 2.1 Accumulation of charge carriers at the ends of p-type (up) and n-type (down) material.	10
Fig. 2.2 Schematic diagram of a simple thermoelectric refrigerator.....	11
Fig. 2.3 Schematic diagram of the Thomson effect.	12
Fig. 2.4 Relation of thermoelectric transport parameters via carrier concentration[1].	15
Fig. 2.5 Schematic of (a) a thermoelectric module, (b) single-stage, (c) segment type, and (d) cascade type of the thermocouple.	16
Fig. 2.6 Plot of reduced efficiency as a function of u, normalized by the Carnot efficiency, for material listed in Table 2.1. Black dots indicate a maximization/compatibility factor[3]	17
Fig. 2.7 Schematic drawing of lattice structures of compound α -Cu ₂ Se (a), β -CuAgSe (b), and α -CuAgSe (c).....	20
Fig. 2.8 Crystal structure model of α -In ₂ Se ₃ (a), β - In ₂ Se ₃ (b), γ - In ₂ Se ₃ (c), and δ - In ₂ Se ₃ (d).....	22
Fig. 2.9 Crystal structure models of ϵ -InSe (a), β -InSe (b), and γ -InSe (c)	24
Fig. 2.10 Formation energies as a function of chemical potential for intrinsic defects[38].....	25
Fig. 3.1 A block diagram of a PID controller in a feedback loop.	32
Fig. 3.2 Step response of P, PI, and PID controller.....	33
Fig. 3.3 The schematic of the Brigman technique and the Stockbarger technique.	37
Fig. 3.4 (a) The furnace in the temperature gradient technique; (b) Heating wire of the furnace; (c) The photo of InSe single crystal.....	39

Fig. 3.5 Our home-made low-temperature physical properties measurement system (PPMS)	41
Fig. 3.6 The photo of our home-build high-temperature transport measurement system.	42
Fig. 3.7 The schematic of STM.....	44
Fig. 3.8 Energy-level diagrams showing the states involved in Raman spectra	45
Fig. 3.9 Schematic representation of the photoluminescence excitation	47
Fig. 3.10 (a) ΔV vs. ΔT at 300 K of polycrystalline Bi and (b) measurement' error.	52
Fig. 4.1 (a) Powder XRD patterns of all CAS samples and (b) enlarged XRD patterns in the 2θ angle range from 31° to 34° for the CAS-2 sample and the Ni-, Co-, Zn-doped CAS-2 samples.	61
Fig. 4.2 Temperature dependence of (a) Seebeck coefficient (S), (b) electrical conductivity (σ), and (c) power factor (PF) of the CAS-1, CAS-2, CAS-3, and the Ni-, Co-, Zn-doped CAS-2 samples.	63
Fig. 4.3 Temperature dependence of (a) thermal diffusivity (D) and (b) thermal conductivity (κ) of the CAS-1, CAS-2, CAS-3, and the Ni-, Co-, Zn-doped CAS-2 samples.	67
Fig. 4.4 (a) Thermoelectric figure of merit (ZT) value and (b) the thermoelectric compatibility factor as a function of temperature for the CAS-1, CAS-2, CAS-3, and the Ni-, Co-, Zn-doped CAS-2 samples.	69
Fig. 5.1 XRD pattern of single-crystalline α -In ₂ Se ₃ . The photo is of α -In ₂ Se ₃ single crystals.	77
Fig. 5.2 FE-SEM image of single-crystalline α -In ₂ Se ₃	78
Fig. 5.3 Room temperature photoluminescence of single-crystalline α -In ₂ Se ₃	79

Fig. 5.4 Raman shift of single-crystalline α -In₂Se₃..... 80

Fig. 5.5 (a) Temperature dependence of the in-plane and out-of-plane electrical resistivity of single-crystalline α -In₂Se₃. (b) Arrhenius plot of the in-plane and out-of-plane electrical resistivity values of single-crystalline α -In₂Se₃ from 300 to 400 K..... 81

Fig. 5.6 Temperature dependence of the in-plane and out-of-plane (a) Seebeck coefficient and (b) power factor..... 84

Fig. 5. 7 (a) V_H/I vs. magnetic field curves for single-crystalline α -In₂Se₃ at various temperatures. (b) The temperature-dependent carrier concentration of α -In₂Se₃ single crystals. (c) Temperature dependence of the in-plane and out-of-plane electrical mobilities. 86

Fig. S5.1 Powder XRD of powdered α -In₂Se₃..... 87

Fig. 6.1 (a) X-ray diffraction pattern taken on the β -InSe cleaved plane; (b) Powder X-ray diffraction pattern of ground β -InSe sample; (c) Raman spectrum taken on the β -InSe cleaved plane; (d) FE-SEM image of the cleaved β -InSe single crystal. 97

Fig. 6.2 (a) Temperature dependence of the in-plane electrical resistivity; (b) the reversibility of the in-plane electrical resistivity with the temperature of the β -InSe single crystal. 99

Fig. 6.3 Temperature dependence of (a) XRD patterns taken on the β -InSe cleaved plane and (b) specific heat capacity of the β -InSe single crystal. 100

Fig. 6.4 STM images taken on the cleaved plane of the β -InSe single crystal and high-resolution STM image taken at one of the defects (marked with a dotted ellipse) at (a) 280 K and (b) 80 K. 102

Fig. 6.5 STM images of sample taken at same positions using the same scanning conditions at (a) 280 K ($V = 10$ mV, $I_t = 50$ pA); (b) 80 K ($V = 3$ V, $I_t = 50$ pA); (c) 280 K ($V = 10$ mV, $I_t = 50$ pA); and (d) 80 K ($V = 1$ V, $I_t = 50$ pA)..... 103

Fig. S6.1 Temperature dependence of the in-plane and out-of-plane (a) electrical resistivity, (b) Seebeck coefficient, and (c) power factor of the β -InSe single crystal..... 104

Chapter 1. Introduction

1.1 Description of the research

Recently, CuAgSe has created a sensation as an excellent thermoelectric material in the medium temperature range as both n-type and p-type thermoelectric materials. Qiu et al.[1] have reported that the thermal conductivity was reduced due to the doping Te into Se-sites, and a maximum ZT value of 0.7 at 450 K of n-type CuAgSe_{0.95}Te_{0.05} was obtained. Hong's group[2] has reported on the thermoelectric properties of p-type CuAgSe with $ZT = 0.95$ at 623 K. Producing both n-type and p-type conduction in the same semiconductor material is ideal for thermoelectric applications due to their similar thermal and mechanical properties, such as melting point, thermal expansion coefficient, etc.,. The stoichiometric CuAgSe has always been reported to show n-type conduction, while the p-type conduction is only present in the non-stoichiometric CuAgSe. However, it is difficult to synthesize the non-stoichiometric p-type CuAgSe without secondary phases. To the best of my knowledge, there have been no reports focusing on the control of the carrier type in CuAgSe.

In this study, a simple and effective way to control the carrier type of single-phase CuAgSe by adjusting the soaking time during growth has been reported. The samples changed from the native n-type characteristic into the non-stoichiometric p-type characteristic with increasing soaking time. On the other hand, it has been found that the n-type characteristic could be preserved with enhanced ZT values in Ni-, Co-, and Zn-doped CuAgSe samples. The maximum thermoelectric figure of merit, ZT value of 0.69 (0.56) at 623 K (673 K) in undoped n-type (p-type) CuAgSe were obtained. Zn is a promising dopant for n-type CuAgSe as it enhances the ZT value.

Single crystalline α -In₂Se₃ possesses a layered structure with tetrahedral covalent bonding between In and Se of Se-In-Se-In-Se, whereas the bonding between two adjacent layers is the weak Van der Waals type[3,4]. Therefore, α -In₂Se₃ usually presents highly anisotropic structural, electrical, optical, and mechanical properties[5–7]. Recently, many defects in In₂Se₃ crystals[8] and their effect on anisotropic charge transport properties have been reported. The anisotropic conductivity in Mn, Cd, I, and Cu-doped In₂Se₃ has also been observed by Kaminskii et al.[7,9] and Zaslokin et al.[6]. The electrical conductivity along layers is much larger than across layers. The anisotropy in temperature-dependent conductivity has been used to evaluate the energy barrier height between the layers in the crystal. In layer-structured In₂Se₃ nanowires, Peng et al.[4] observed a large anisotropy of electrical conductivity up to $10^3 - 10^6$ at room temperature. Nevertheless, the anisotropic ratio about the electrical resistivity of the α -In₂Se₃ bulk single crystals was not high, and the anisotropic Seebeck coefficient has not been thoroughly investigated. To the best of our knowledge, there have been no reports focusing on the control of the carrier type in CuAgSe.

In this thesis, the growth of In₂Se₃ single crystals by the temperature gradient method is presented. The crystal structure, optical properties, and anisotropic transport properties of single-crystalline α -In₂Se₃ were experimentally investigated. A robust electrical resistivity and Seebeck coefficient dependence about crystallographic directions was concluded to be observed.

InSe is a new promising platform for developing high-speed electronic devices due to its small effective mass ($m^* = 0.14m_0$), high electron mobility (exceeds $10^3 \text{ cm}^2 \text{ V}^{-1} \text{ s}^{-1}$ and $10^4 \text{ cm}^2 \text{ V}^{-1} \text{ s}^{-1}$ at room and liquid-helium temperatures, respectively)[10], flexibility, and ambient stability[11]. Recently, InSe has been reported with outstanding efficiency optoelectronic devices[12,13]. InSe-based photodetectors have been reported as the most efficient among 2D

materials[14]. So far, β -InSe has been known as the most stable phase of InSe. The ambient stability of InSe-based FETs has been demonstrated. The FET with uncapped InSe active channel exhibits a p-type transport due to environmental doping (H_2O) at defects sites, while FET with hBN capped InSe active channel exhibit ambipolar transport[11]. However, more insightful investigations on this issue under different applied extreme conditions are needed to be revealed. On the other hand, β -InSe has attracted more and more attention in the thermoelectric (TE) field because of its layered crystal structure. Zhai *et al.*[15] have reported that the substitution of Sn into In sites can help to enhance the TE power factor and reduce the thermal conductivity of β -InSe, resulting in an improvement the value of the thermoelectric figure of merit, ZT , from 0.42 (undoped) to 0.66 (5% Sn doped) at 700 K. Haleoot's group[16] have predicted that doping Bi into Se sites also helps to improve the TE performance of β -InSe with the maximum ZT value of 0.65 for β -InSe_{0.75}Bi_{0.25} alloy at 800 K. However, among limited publications, focusing on TE properties of InSe, a study on low-temperature TE transport properties of single-crystalline β -InSe has not been reported, yet.

This study provides more insight investigations from macroscopic to microscopic scale on InSe single-crystal stability, grown by using a temperature gradient technique. The temperature gradient technique provided excellent InSe ingot, which crystallized in the hexagonal β -InSe phase. Scanning tunneling microscopy (STM) studies demonstrated an un-stability characteristic of the β -InSe single crystal where defects and surface of InSe can be modified under an applied bias voltage and a change of temperature. This un-stability characteristic of InSe led to a discontinuity in its transport property.

1.2 List of publications

1. **Thi Huong Nguyen**, Van Quang Nguyen, Anh Tuan Duong, and Sunglae Cho, “2D semiconducting α -In₂Se₃ single crystals: Growth and huge anisotropy during transport”, J. Alloys Compd., **810**, 151968 (2019).
2. **Thi Huong Nguyen**, Van Quang Nguyen, Anh Tuan Pham, Jong Ho Park, Ji Eun Lee, Jae Ki Lee, Sudong Park, and Sunglae Cho, “Carrier control in CuAgSe by growth process or doping”, J. Alloys Compd., **852**, 157094 (2021).
3. **Thi Huong Nguyen**, Thi Ly Trinh, Van Quang Nguyen, Anh Duc Nguyen, Van Thiet Duong, Tran Van Tam, Song Yi Back, Kyuwook Ihm, Jong-Soo Rhyee, Jungdae Kim, and Sunglae Cho, “Growth & Un-stability characteristic of β -InSe single crystal”, **TO BE SUBMITTED** (2020).
4. Van Quang Nguyen, **Thi Huong Nguyen**, Van Thiet Duong, Ji Eun Lee, Su-Dong Park, Jae Yong Song, Hyun-Min Park, Anh Tuan Duong, and Sunglae Cho, “Thermoelectric properties of hot-pressed Bi-doped n-type polycrystalline SnSe”, Nanoscale Res. Lett., **13**, 200, (2018).
5. Van Thiet Duong, Van Quang Nguyen, Thi Minh Hai Nguyen, **Thi Huong Nguyen**, Anh Tuan Duong, Duc Dung Dang, Tam Tran Van, and Sunglae Cho, “Optimizing the Carrier Density and Thermoelectric Properties of Sb₂Te₃ Films by Using the Growth Temperature”, J. Korean. Phys. Soc. **72**, 915, (2018).
6. Van Quang Nguyen, Van Thiet Duong, **Thi Huong Nguyen**, Rakwon Kang, Anh Tuan Pham, Van Tam Tran, Cao Khang Nguyen, Anh Tuan Duong, Thang Bach Phan, Jungdae Kim, and Sunglae Cho, “Se/Sn flux ratio effects on epitaxial SnSe thin films; crystallinity & domain rotation”, J. Alloys Compd., **840**, 155680 (2020).

1.3 References

- [1] P.F. Qiu, X.B. Wang, T.S. Zhang, X. Shi, L.D. Chen, Thermoelectric properties of Te-doped ternary CuAgSe compounds, *J. Mater. Chem. A*. 3 (2015) 22454–22461. <https://doi.org/10.1039/c5ta06780d>.
- [2] A.J. Hong, L. Li, H.X. Zhu, X.H. Zhou, Q.Y. He, W.S. Liu, Z.B. Yan, J.M. Liu, Z.F. Ren, Anomalous transport and thermoelectric performances of CuAgSe compounds, *Solid State Ionics*. 261 (2014) 21–25. <https://doi.org/10.1016/j.ssi.2014.03.025>.
- [3] N.D. Raranskii, V.N. Balazyuk, Z.D. Kovalyuk, N.I. Mel’Nik, V.B. Gevik, Crystal growth and elastic properties of In_2Se_3 , *Inorg. Mater.* 47 (2011) 1174–1177. <https://doi.org/10.1134/S0020168511110203>.
- [4] H. Peng, C. Xie, D.T. Schoen, Y. Cui, Large anisotropy of electrical properties in layer-structured In_2Se_3 nanowires, *Nano Lett.* 8 (2008) 1511–1516. <https://doi.org/10.1021/nl080524d>.
- [5] M. Ishikawa, T. Nakayama, Stacking and Optical Properties of Layered In_2Se_3 , *Jpn J. Appl. Phys.* 37 (1998) 1122–1124.
- [6] A. V. Zaslonskiy, Z.D. Kovalyuk, I. V. Mintyanskiy, Electrical properties of In_2Se_3 layered crystals doped with Cadmium, Iodine, or Copper, *Inorg. Mater.* 43 (2007) 1271–1274. <https://doi.org/10.1134/S0020168507120011>.
- [7] V.M. Kaminskii, Z.D. Kovalyuk, A. V. Zaslonskiy, V.I. Ivanov, Electrical properties of $\text{In}_2\text{Se}_3\langle\text{Mn}\rangle$ and $\text{InSe}\langle\text{Mn}\rangle$ crystals, *Inorg. Mater.* 48 (2012) 103–105. <https://doi.org/10.1134/S0020168512020112>.
- [8] J. Cui, L. Wang, Z. Du, P. Ying, Y. Deng, High thermoelectric performance of a defect

- in α -In₂Se₃-based solid solution upon substitution of Zn for In, *J. Mater. Chem. C.* **3** (2015) 9069–9075. <https://doi.org/10.1039/c5tc01977j>.
- [9] V.M. Kaminskii, Z.D. Kovalyuk, A. V. Zaslonskiy, V.I. Ivanov, Structure and electrical properties of In₂Se₃<Mn> layered crystals, *Semicond. Physics, Quantum Electron. Optoelectron.* **12** (2009) 290–293. <https://doi.org/10.15407/spqeo12.03.290>.
- [10] D.A. Bandurin, A. V. Tyurnina, G.L. Yu, A. Mishchenko, V. Zólyomi, S. V. Morozov, R.K. Kumar, R. V. Gorbachev, Z.R. Kudrynskiy, S. Pezzini, Z.D. Kovalyuk, U. Zeitler, K.S. Novoselov, A. Patanè, L. Eaves, I. V. Grigorieva, V.I. Fal'ko, A.K. Geim, Y. Cao, High electron mobility, quantum Hall effect and anomalous optical response in atomically thin InSe, *Nat. Nanotechnol.* **12** (2017) 223–227. <https://doi.org/10.1038/nnano.2016.242>.
- [11] A. Politano, G. Chiarello, R. Samnakay, G. Liu, B. Gürbulak, S. Duman, A.A. Balandin, D.W. Boukhvalov, The influence of chemical reactivity of surface defects on ambient-stable InSe-based nanodevices, *Nanoscale.* **8** (2016) 8474–8479. <https://doi.org/10.1039/c6nr01262k>.
- [12] S. Sucharitakul, N.J. Goble, U.R. Kumar, R. Sankar, Z.A. Bogorad, F.C. Chou, Y.T. Chen, X.P.A. Gao, Intrinsic Electron Mobility Exceeding 10³ cm²/(V s) in Multilayer InSe FETs, *Nano Lett.* **15** (2015) 3815–3819. <https://doi.org/10.1021/acs.nanolett.5b00493>.
- [13] Z. Chen, J. Biscaras, A. Shukla, A high performance graphene/few-layer InSe photodetector, *Nanoscale.* **7** (2015) 5981–5986. <https://doi.org/10.1039/c5nr00400d>.
- [14] F.H.L. Koppens, T. Mueller, P. Avouris, A.C. Ferrari, M.S. Vitiello, M. Polini, Photodetectors based on graphene, other two-dimensional materials and hybrid systems,

Nat. Nanotechnol. 9 (2014) 780–793. <https://doi.org/10.1038/nnano.2014.215>.

- [15] Y. Zhai, Q. Zhang, J. Jiang, T. Zhang, Y. Xiao, S. Yang, G. Xu, Thermoelectric properties of $\text{In}_{1.3-x}\text{Sn}_x\text{Se}$ prepared by spark plasma sintering method, *J. Alloys Compd.* 553 (2013) 270–272. <https://doi.org/10.1016/j.jallcom.2012.11.139>.
- [16] R. Haleoot, B. Hamad, Thermoelectric properties of doped β -InSe by Bi: First principle calculations, *Phys. B Condens. Matter.* 587 (2020) 412105. <https://doi.org/10.1016/j.physb.2020.412105>.

Chapter 2. Background

2.1 Physical phenomena of thermoelectricity

The thermoelectric effect is the direct conversion of temperature differences to electric voltage and vice versa. When the side of a substance is exposed to a different temperature, a voltage difference is produced across the two sides of the materials, called thermal voltage. Conversely, when a voltage applies to its ends, a temperature difference is created. The thermoelectric effect consists of three distinct effects: the Seebeck effect, invented by Thomas Johann Seebeck – A baltic German physicist; the Peltier effect by Jean Charles Peltier – a French physicist; and the Thomson effect by Lord Kelvin (Irish-born William Thomson).

The thermoelectric effect can use to generate electricity (thermoelectric generator), which directly convert heat to electricity, measure temperature (e.g., thermocouple), and change the temperature of objects (e.g., thermoelectric refrigerator).

2.1.1 The Seebeck effect

In 1821, a well-respected German physicist Thomas Johann Seebeck found that a compass needle would be deflected by a circuit formed by two different metals (copper and bismuth) joined in two places an applied temperature difference between the joints. A thermoelectric voltage is created at two joints, and a current is generated. This phenomenon is because of the difference in the number of electrons moved in the different metals. When an electrical current is created through the wires, it causes a magnetic field around the wires. Seebeck did not recognize the electric current's existence at that time, so he called the phenomenon "thermomagnetic effect". Afterward, a Danish physicist Hans Christian Ørsted regulated the omission and proposed the term "thermoelectricity".

The Seebeck effect represents the buildup of a potential difference ΔV across a semiconductor or conductor (metal) due to the diffusion of charge carriers along the temperature gradient $\Delta T = T_{\text{hot}} - T_{\text{cold}}$, in which one side of the material is heated or cooled. The charge carriers move from the hot end to the cold end, creating a gradient in the number of charge carriers, leading to generating the potential difference, at equilibrium, balanced by the resulting internal electrical field. The larger the temperature gradient, the more charge carriers moved to the cooler side, the higher the potential difference is created. The melting point of the material limits this potential difference. The Seebeck coefficient S is the ratio of potential difference and temperature gradient between two ends; it is given by

$$S = \frac{\Delta V}{\Delta T} \quad (2.1)$$

where S is the Seebeck coefficient (or thermopower), ΔV is the thermal voltage, ΔT is the temperature difference between cold and hot ends. Depending on the type of majority carriers (i.e., holes or electrons), the potential difference (and hence the Seebeck coefficient) can be positive or negative, i.e., $S > 0$ for p-type semiconductors and $S < 0$ for n-type semiconductors and metals (Fig. 2.1). Another definition of the Seebeck coefficient is the entropy per charge carrier related to the density of states (DOS).

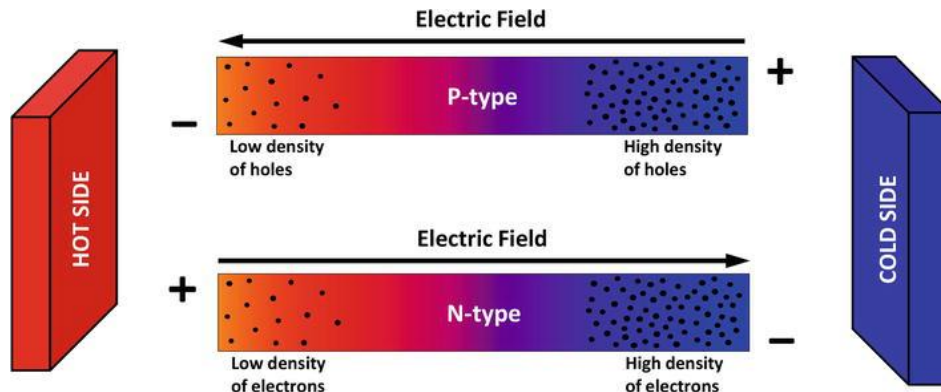


Fig. 2.1 Accumulation of charge carriers at the ends of p-type (up) and n-type (down) material.

The Seebeck coefficient generally varies as a function of temperature and depends strongly on the substance's composition. The Seebeck coefficient is very low for metal at room temperature due to the high mobility of free electrons (only a few $\mu\text{V K}^{-1}$) and much more extensive for semiconductors (from -100 to $1000 \mu\text{V K}^{-1}$). The Seebeck effect's main application is thermoelectric generator, thermocouple (to measure a temperature difference), and to classify an unknown composition metal (if it is kept at a constant temperature and held in contact with a well-known metal and heated to probe temperature).

2.1.2 The Peltier effect

The Peltier effect is the reverse phenomenon of the Seebeck effect; the electrical current flowing through the junction connecting two materials will emit or absorb heat per unit time at the junction to balance the difference in the chemical potential of two materials.

Similarly to the Seebeck coefficient, the Peltier coefficient Π_{AB} is defined as the coefficient of the thermal current Q to the electrical current I , given by

$$Q = \Pi_{AB} I = (\Pi_A - \Pi_B) I \quad (2.2)$$

The Peltier effect is superimposed by simultaneous Joule heating and Thomson heating or cooling so that the Peltier coefficient can be difficultly measured with accuracy.

Figure 2.2 shows a thermoelectric device using the Peltier effect (thermoelectric refrigerator). The device consists of a pair of n- and p-type semiconductors electrically connected in series and thermally connected in parallel. When a current I is applied from n- to p-type semiconductors, electrons in the n-type and holes in the p-type semiconductors move down; heat is dissipated at the bottom surface. As a result, the top surface is cooled. The heating and cooling surfaces are changed if we change the current direction. It is a part of the thermoelectric module, where many pairs are electrically connected in series and thermally connected in parallel. It is also the principle of a thermoelectric refrigerator.

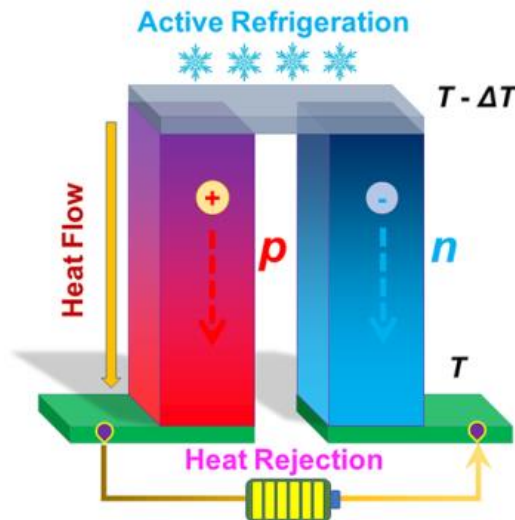


Fig. 2.2 Schematic diagram of a simple thermoelectric refrigerator.

2.1.3 The Thomson effect

The Seebeck and Peltier effects are different demonstrations of the same physical process, often referred to as the Peltier-Seebeck effect. The Thomson effect is an extension of the Peltier-Seebeck model and is discovered by Lord Kelvin.

The effect has occurred when an electric current and a temperature gradient co-exist in a single homogeneous conductor, leading to the generation of reversible cooling or heating, as illustrated in Fig. 2.3.

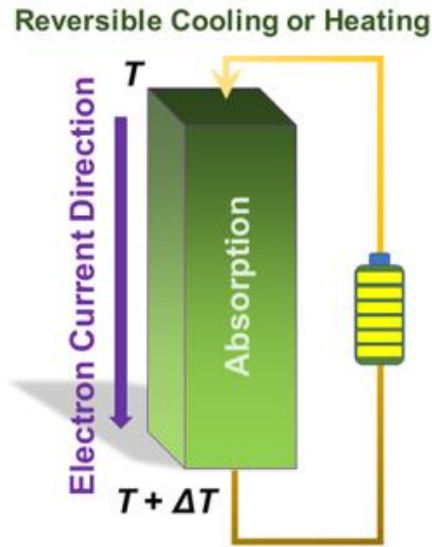


Fig. 2.3 Schematic diagram of the Thomson effect.

The Thomson effect can be described

$$\tau = \frac{dq/dx}{I dT/dx} \quad (2.3)$$

where τ is the Thomson factor, I is the current, dq/dx is the rate of heating or cooling per unit length, dT/dx is the temperature gradient. This equation, however, neglects Joule heating and ordinary thermal conductivity.

Compared with the Seebeck and Peltier effects, the Thomson effect is often ignored in thermoelectric device design and energy conversion analysis. Nevertheless, when a large temperature gradient exists in actual thermoelectric devices, the Thomson effect cannot be neglected and should be carefully considered.

2.1.4 Kelvin relation

In 1954, Lord Kelvin found the relationships of these three effects using the first and second thermodynamics laws to a simple thermoelectric circuit, assuming it to be a reversible system.

The first Kelvin relation is:

$$\tau_{ab} = \frac{d\pi_{ab}}{dT} - S_{ab} \quad (2.4)$$

where τ_{ab} , π_{ab} , S_{ab} are the Thomson, Peltier, and Seebeck coefficients, respectively, T is the absolute temperature.

The second Kelvin relation is:

$$\pi_{ab} = TS_{ab} \quad (2.5)$$

Using the second Kelvin relation, the first one can be written as

$$\tau_{ab} = T \frac{dS_{ab}}{dT} \quad (2.6)$$

Therefore, if one thermoelectric coefficient is completely known, the other two can be calculated with these equations. The second relation implies that the integral

$$S = \int_0^T \frac{d\tau}{dT} dT \quad (2.7)$$

makes possible the determination of absolute S on a single conductor, provided the Thomson coefficient is known. Here $S(T=0)$ has been set equal to zero under the third law of thermodynamics. Because these measurements are complicated, they have been performed for only a few substances, such as lead and platinum, thus serving as references.

2.1.5 Thermoelectric figure of merit

A TE generator directly generates electricity from the temperature gradient through the TE material. The maximum efficiency of a TE generator is given by,

$$\eta_{max} = \frac{\Delta T}{T_h} \frac{\sqrt{1 + ZT_{avg}} - 1}{\sqrt{1 + ZT_{avg}} + \frac{T_c}{T_h}} \quad (2.8)$$

where T_h and T_c are the hot- and cold-side temperature, and ΔT and T_{avg} are their difference, $T_h - T_c$ and the average $(T_h + T_c)/2$, respectively. The TE conversion efficiency by Eq. 2.8 is the product of the Carnot efficiency $\Delta T/T_h$ and a reduction factor as a function of the material's figure of merit,

$$Z = \frac{S^2 \sigma}{\kappa} \quad (2.9)$$

where S is the Seebeck coefficient, σ is the electrical conductivity, and κ is the thermal conductivity.

The dimensionless figure of merit is calculated by,

$$ZT = \frac{S^2 \sigma}{\kappa} T \quad (2.10)$$

From Eq. 2.8, the conversion efficiency is proportioned to the ZT. The high ZT is made of high efficiency. Generally, a high $S^2 \sigma$ and low κ are required to ensure high ZT. However, it is difficult to meet these requirements due to the interdependence of the parameters. To enhance ZT, we need to consider the relationships between n or p (here n is taken as an example) and S , σ , and κ .

$$S = \frac{8\pi^2 k_B^2}{3eh^2} m^* T \left(\frac{\pi}{3n}\right)^{\frac{2}{3}} \quad (2.11)$$

$$\sigma = ne\mu \quad (2.12)$$

$$\kappa = D_T C_p \rho = \kappa_e + \kappa_l \quad (2.13)$$

$$\kappa_e = L\sigma T = ne\mu LT \quad (2.14)$$

where, k_B is the Boltzmann constant, e is the electrical charge, h is the Planck constant, m^* is the carrier's effective mass, μ is the carrier mobility, D_T is the thermal diffusivity, C_p is the specific heat, ρ is the mass density, and L is the Lorentz number. These equations show that the values of S , σ , and κ should be balanced to optimize ZT , as presented in Fig. 2.4[1].

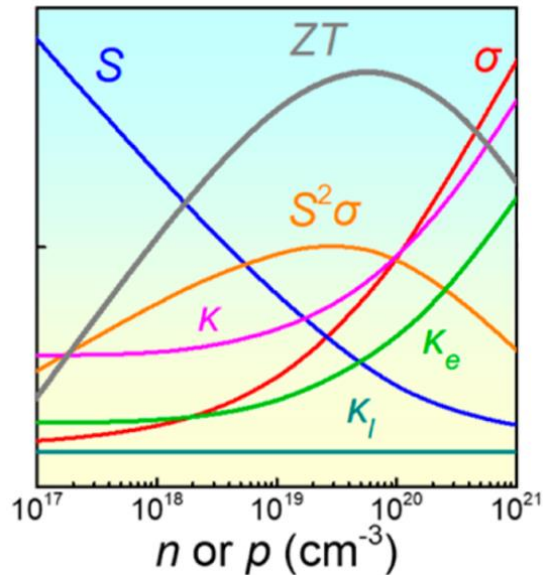


Fig. 2.4 Relation of thermoelectric transport parameters via carrier concentration[1].

The optimized carrier concentration is 10^{19} to 10^{20} cm^{-3} between common metals and semiconductors or in heavily doped semiconductors.

2.2 Thermoelectric devices

2.2.1 Thermoelectric module

The actual maximum conversion efficiency usually is lower than the calculated value due to parasitic ohmic loss at the electrode interface and heat loss at various parts of the module. Fig.

2.5a shows a thermoelectric module schematic containing many couples of p- and n-type thermoelectric legs. The interconnect electrodes must have low electrical contact resistance to draw sufficient electric power from the legs and high thermal conductivity to effectively deliver thermal power to the legs. An effective way to increase conversion efficiency is connected modules using the segment type or cascade type, as shown in Fig. 2.5c and Fig. 2.5d. In a segment module, it is fabricated by using different n-type (p-type) TE materials with different working temperature ranges that were segmented together in the n-type (p-type) leg[2]. Cascade modules are manufactured using at least two different modules. The first is a module with high efficiency at a higher temperature and is stacked on top of a second module with high efficiency at lower temperatures[1].

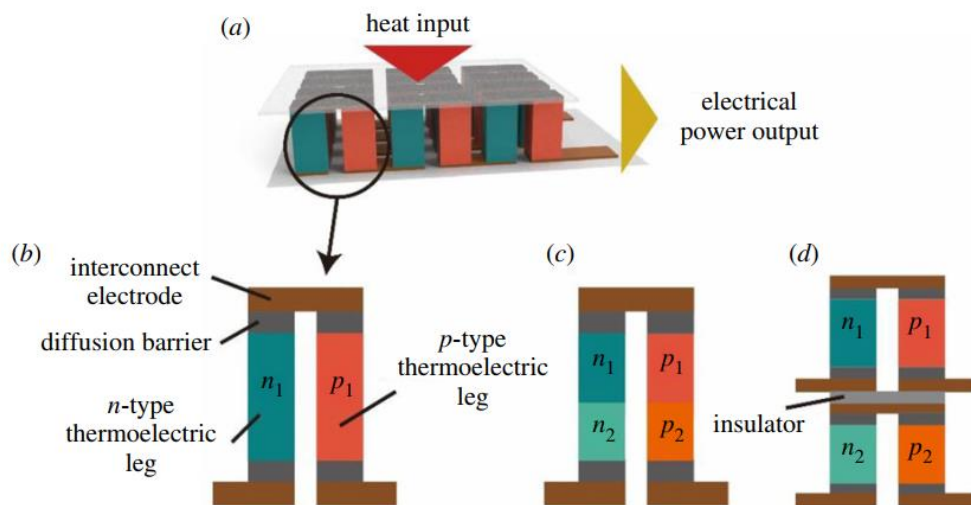


Fig. 2.5 Schematic of (a) a thermoelectric module, (b) single-stage, (c) segment type, and (d) cascade type of the thermocouple.

2.2.2 Thermoelectric compatibility factor

To determine suitable segmentation partners for a TE material, the thermoelectric (power generation) compatibility factor of a TE material was calculated using Eq. (2)[3],

$$\alpha = \frac{\sqrt{1 + ZT} - 1}{ST} \quad (2)$$

where S is the Seebeck coefficient, and T is the absolute temperature.

From Eq. (2), it is clear that the compatibility factor α is a temperature-dependent material property derived from the properties of the temperature-dependent material S , σ , and κ . Thus, α cannot be changed with device geometry or the alteration of electrical or thermal currents.

Two TE materials are suitable for segmentation if their TE compatibility factor ratio is smaller than 2. Smaller TE compatibility factor ratios indicate that the materials are more suitable for segmentation. For instance, despite the high figure of merit, SiGe cannot be efficiently segmented with the other thermoelectric materials shown in Fig. 2.6. Since the compatibility factor ratio between SiGe and others is larger than 2, the maximum efficiency can decrease by segmentation[3].

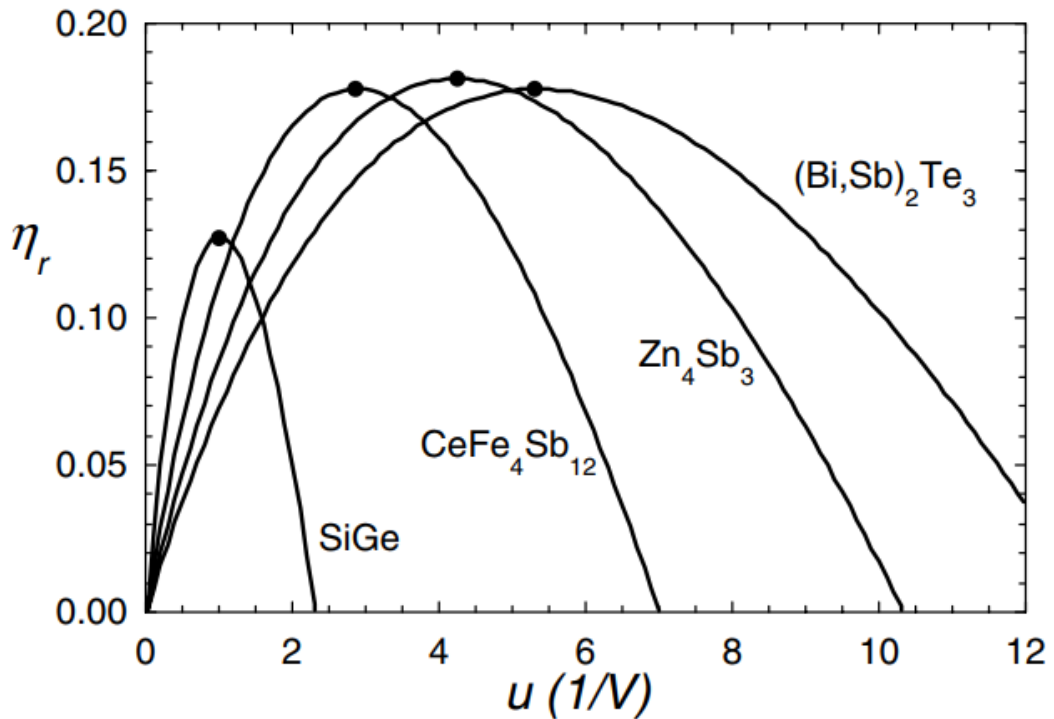


Fig. 2.6 Plot of reduced efficiency as a function of u , normalized by the Carnot efficiency, for material listed in Table 2.1. Black dots indicate a maximization/compatibility factor[3]

Table 2.1 Temperature ranges for materials considered for segmentation in a typical p-leg with their respective compatibility factors[3].

p-leg	T_c (K)	T_H (K)	α (V^{-1})
1-(Sb,Bi) ₂ Te ₃	300	451	2.900
2-Zn ₄ Sb ₃	451	677	2.119
3-CeFe ₄ Sb ₁₂	677	973	1.558
Segs. 1+2+3	300	973	2.011
4-SiGe	973	1300	0.4116

2.3 Thermoelectric material research

2.3.1 Brief thermoelectricity of layered chalcogenides

Layered chalcogenides have long been recognized as excellent TE materials due to their unique crystal structure and the potential for manipulating charge carrier transport and phonon transport by different crystal plane modulation. In the tetradymites family, Bi₂Te₃ and Sb₂Te₃, the best candidates for TE materials at room temperature, were commercialized and used in TE refrigerators several decades ago. In 2000, the ZT values of 2.4 at 300 K in the superlattice film Bi₂Te₃-Sb₂Te₃ had reported, which was attracted more and more effort to improve conventional TE materials and research on the TE nanomaterials[4]. In 2014 and 2015, the maximum ZT for bulk p-type Bi_{0.5}Sb_{1.5}Te₃ and n-type Bi₂Se_{0.3}Te_{2.7} obtained 1.86 at 320 K and 1.2 at 445 K, respectively[5,6]. Bi₂Se₃ has a layered structure similar to that of Bi₂Te₃, and the elements Se is less expensive and less toxic than Te, so much effort has been put into investigating the TE performance of the Bi-Se system. Ali's group[7] and Gupta's group[8] have reported that the maximum ZT values for p- and n-type Bi₂Se₃ have reached 0.41 and 0.75, respectively. Besides the traditional TE materials, Sn-X and In-X systems are typical TE materials with excellent performance and low cost. Significantly, the layered structure of SnSe and In₄Se₃ is a distorted

quasi-one-dimensional chain-like structure. Along with this chainlike structure, the charge transport is inherently low dimensional with strong electron-phonon coupling (a structure called the Peierls distortion), leading to a decrease in the thermal conductivity. The occurrence of this phenomenon distorts the chain to form a two-dimensional superlattice structure and charge density wave (CDW) states. Simultaneously, the weak van der Waals bonding in the out-of-plane direction helps reduce the lattice thermal conductivity. Due to the combination of these factors, the SnSe and $\text{In}_4\text{Se}_{3-x}$ single crystals showed good thermoelectric performance, with a maximum ZT values of 2.6 at 923 K (p-type) and 1.48 at 705 K (n-type), respectively[9,10]. As a group of layered superionic conductors, MCrX_2 ($\text{M} = \text{Ni, Cu, or Ag}$; $\text{X} = \text{S/Se}$) compounds possess polar layered crystal structure ($\text{R}\bar{3}\text{m}$) at room temperature, which has been exhibited very low lattice thermal conductivity, hence can be regarded as potential candidates for TE applications. A high ZT of 1.4 was achieved in sandwich-like $(\text{AgCrSe}_2)_{0.5}(\text{CuCrSe}_2)_{0.5}$ at 773 K[11]. TiS_2 , a transition metal dichalcogenide, has a layered structure with a wide van der Waals gap. A high power factor has been observed in $\text{Ti}_{1+x}\text{S}_2$ due to the excess Ti atoms inserted into the layers. A maximum ZT value of 0.34 was obtained in $\text{Ti}_{1.008}\text{S}_2$ at 663 K[12]. Additionally, the alloying effect and Cu intercalation to improve TE efficiency, the highest ZT value of 0.54 in TiS_2 was observed at 700 K[13]. On the other hand, the concept PLEC simultaneously exhibits high electrical conductivity, and low thermal conductivity was proposed in binary or ternary chalcogenides of Cu or Ag. The PLEC compounds exhibit excellent thermoelectric performance, as indicated by the high ZT values of Cu_2Se and Cu_2S . Liu et al.[14] reported a maximum ZT value of 2.3 at 400 K for an I-doped Cu_2Se sample due to the critical scattering of electrons and phonons, which means achieving minimum thermal conductivity and maximum electrical conductivity at the same time. Due to the liquid behavior of Cu^+ , even the polycrystalline bulk $\text{Cu}_{1.97}\text{S}$ produced by a simple melt-solidification method achieved a maximum ZT of 1.9 at 970 K[15].

2.3.2 Overview of CuAgSe

The good TE performances of the Cu_2Se compound have stimulated substantial efforts in searching for more TE materials with similar superionic structure and preferred TE performances. An immediate candidate is CuAgSe , i.e., randomly Ag-substituted Cu_2Se compounds. Similar to Cu_2Se , CuAgSe also has two phases: the low-temperature β -phase and the high-temperature α -phase[16]. At temperatures below 470 K, β -phase is a semimetal with a unique layered structure consisting of alternating stacking of the Ag and CuSe layers,

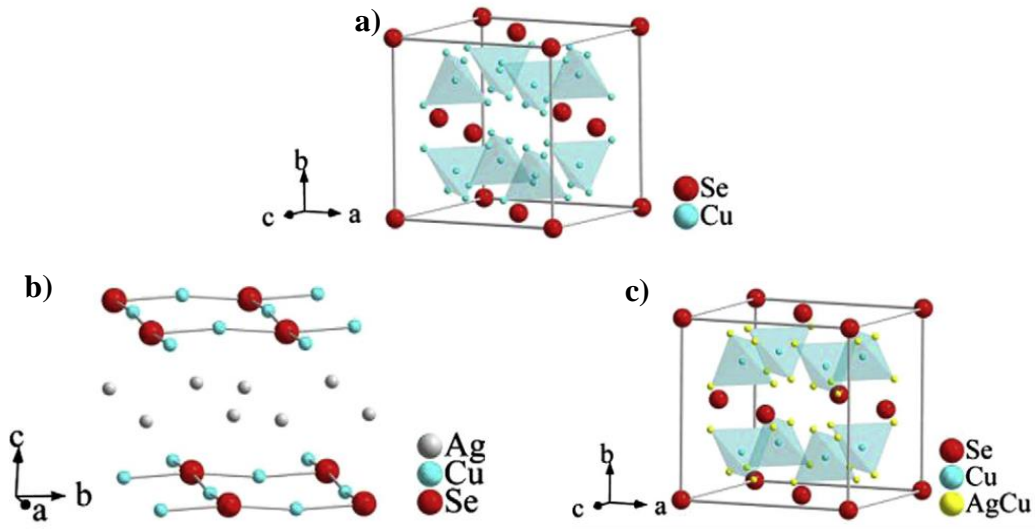


Fig. 2.7 Schematic drawing of lattice structures of compound α - Cu_2Se (a), β - CuAgSe (b), and α - CuAgSe (c)

allowing probably high mobility of about $20,000 \text{ cm}^2\text{V}^{-1}\text{s}^{-1}$ at 10 K[17]. At temperatures above 470 K, the α -phase is a semiconductor with a crystal structure similar to the superionic Cu_2Se with the mobile Ag/Cu cations randomly distributing among the tetrahedral sites (Fig. 2.7)[18]. This crystal structure may allow even lower lattice thermal conductivity than α - Cu_2Se , due to the random half-substitution of Cu ions by Ag ions and a higher degree of occupation disorder. Thus an investigation of the structural and TE behaviors is interested.

Recently, Hong et al.[18] measured the TE properties of CuAgSe up to 623 K and found that its ZT value is low at room temperature but high at elevated temperatures ($ZT \sim 0.95$ at 623

K). Furthermore, as the temperature increases, both Ishiwata et al.[17] and Hong et al.[18] observed an n- to p-type carrier transition due to the existence of two types of charge carriers (electrons and holes), which can lower the thermopower and ZT value. Qiu's group[19] has doped Te into Se-sites and observed a maximum ZT value of 0.7 at 450 K for n-type $\text{CuAgSe}_{0.95}\text{Te}_{0.05}$.

Producing both n-type and p-type conduction in the same semiconductor material is ideal for thermoelectric applications due to their similar physical and chemical properties, such as melting points, thermal expansion coefficient. The stoichiometric CuAgSe has always been reported to show n-type conduction, while the p-type conduction is only present in the non-stoichiometric CuAgSe . However, it is difficult to synthesize the non-stoichiometric p-type CuAgSe without secondary phases. Controlling the carrier type in CuAgSe is an unsolved question.

2.3.3 Overview of In_2Se_3

In_2Se_3 is likely the most complex compound among indium selenides; exists many phases, such as the rhombohedral α -phase, the rhombohedral β -phase, the defect wurtzite γ -phase, and the hexagonal δ -phase[20,21], as depicted in Fig. 2.8. The rhombohedral α - In_2Se_3 crystallizes in a layered structure with each layer consisting of Se-In-Se-In-Se, belongs to space group $R\bar{3}m$ with lattice parameters $a = 4.05 \text{ \AA}$ and $c = 28.77 \text{ \AA}$. Within the layer, In and Se atoms are covalently bonded, while the neighboring layers are bonded by the weak van der Waals interaction[20,22]. The rhombohedral β - In_2Se_3 was formed after the phase transformation of α - In_2Se_3 above $200 \text{ }^\circ\text{C}$. Osamura et al.[21] obtained the XRD pattern (collected at $250 \text{ }^\circ\text{C}$) of β - In_2Se_3 and indexed the crystal structure belongs with a space group of $R\bar{3}m$ and lattice parameters of $a = 4.05 \text{ \AA}$ and $c = 29.41 \text{ \AA}$. The defect wurtzite γ - In_2Se_3 can be formed by further heating β - In_2Se_3 at a higher temperature, such as $350 \text{ }^\circ\text{C}$, $520 \text{ }^\circ\text{C}$, and 650

°C[23]. γ - In_2Se_3 was a vacancy ordered in the screw form phase, in which vacancies on 1/3 of the cation site were ordered in vacancy ordered in the screw form along the c-axis. The early investigations on γ - In_2Se_3 presented lattice parameters of $a = 7.11 \text{ \AA}$ and $c = 19.30 \text{ \AA}$. Further heating γ - In_2Se_3 can obtain the hexagonal δ - In_2Se_3 at even higher temperatures, such as $550 \text{ }^\circ\text{C}$ and $730 \text{ }^\circ\text{C}$ [23]. Popovic et al.[24] reported the lattice parameters of δ - In_2Se_3 as $a = 4.014 \text{ \AA}$ and $c = 9.64 \text{ \AA}$ with a space group $P3m1$.

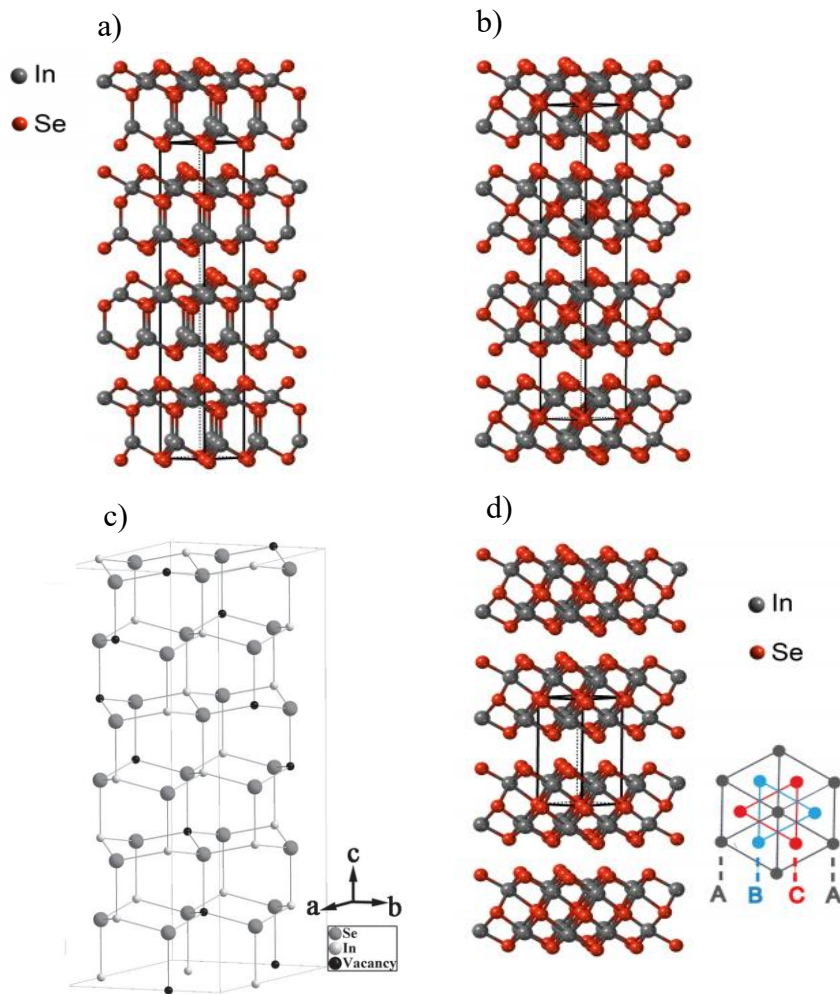


Fig. 2.8 Crystal structure model of α - In_2Se_3 (a), β - In_2Se_3 (b), γ - In_2Se_3 (c), and δ - In_2Se_3 (d)

Several studies were performed to measure and improve the TE properties of In_2Se_3 . Due to the low thermal conductivity, the maximum ZT values of 0.25 and 0.2 were observed in α - In_2Se_3 and γ - In_2Se_3 at 884 and 673 K, respectively[25,26]. Melting was applied to synthesize Ag incorporated In_2Se_3 and ZT of 0.63 at 884 K. However, Ag incorporated In_2Se_3 samples

were mainly composed of ternary phases In_5AgSe_8 . To the best of our knowledge, there have not been reported on the low-temperature TE transport properties and the anisotropy during transport of the single-crystalline In_2Se_3 sample.

2.3.4 Overview of InSe

InSe is a member of the III-monochalcogenide semiconductor group and promising material for developing high-speed electronic devices due to its small effective mass ($m^* = 0.14m_0$), high electron mobility (exceeds $10^3 \text{ cm}^2 \text{ V}^{-1} \text{ s}^{-1}$ and $10^4 \text{ cm}^2 \text{ V}^{-1} \text{ s}^{-1}$ at room and liquid-helium temperatures, respectively)[27], flexibility, and ambient stability[28]. InSe exhibits a layered structure, where each layer contains sublayers, closely packed with two In and two Se in a stacking sequence Se-In-In-Se, whereas the bonding between two adjacent layers is the weak Van der Waals type[29]. Therefore, InSe usually presents a strong anisotropy characteristic. On the other hand, InSe can crystallize in hexagonal (β - and ϵ -InSe) or rhombohedral (γ -InSe) layered crystal structures that differ stacking of the quadruple-layers, as presented in Fig. 2.9[30]. The crystal structure of β - and ϵ -InSe shows ABAB stacking, while the ABCABC stacking exists in the rhombohedral γ -InSe structure. The hexagonal β - and ϵ -InSe phases show similar lattice parameters of $a = 4.005 \text{ \AA}$ and $c = 16.640 \text{ \AA}$. They can be distinguished by using the Raman technique[30,31]. The rhombohedral γ -InSe belongs to the $R\bar{3}m$ space group with lattice parameters of $a = 4.005 \text{ \AA}$ and $c = 24.960 \text{ \AA}$ [32].

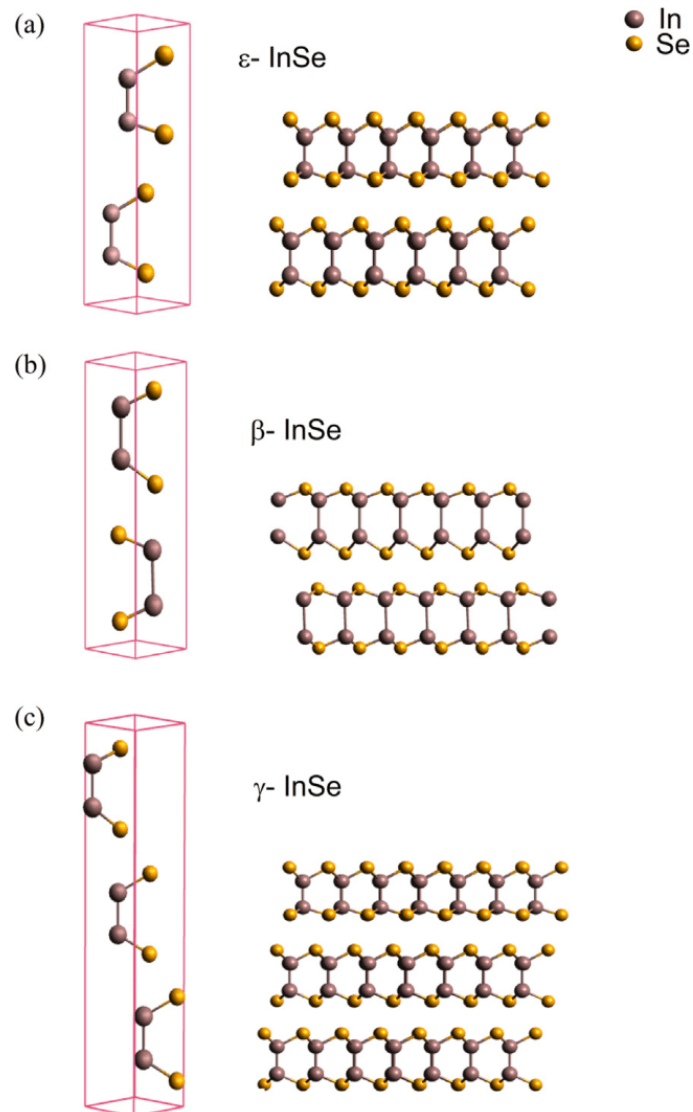


Fig. 2.9 Crystal structure models of ϵ -InSe (a), β -InSe (b), and γ -InSe (c)

Furthermore, the β and γ -InSe phases exhibit direct bandgap ($E_g = 1.25$ and 1.29 eV), an essential concern for InSe-based optoelectronic devices[23,33–35].

Zhai et al.[36] investigated the TE properties of n-type β -InSe and Sn-doped β -InSe polycrystalline samples fabricated by melting and spark plasma sintering. TE property evaluations showed that Sn-doping slightly enhanced the power factor and reduced the thermal conductivity of β -InSe; therefore, an enhanced maximum ZT of 0.66 was achieved at 700 K, representing 57% improvement to the un-doped sample. Haleoot's group[37] have predicted

that doping Bi into Se sites also helps to improve the TE performance of β -InSe with a maximum ZT value of 0.65 for β -InSe_{0.75}Bi_{0.25} alloy at 800 K. To the best of our knowledge, there have been no reports about the low-temperature TE properties of the β -InSe single crystal.

Additionally, a study on defects and their effects on the physical properties of InSe is a desirable work for realizing the material in various applications. Xiao et al.[38] have been reported that the dominant intrinsic defects in In-rich material are the In interstitial, a shallow donor, and the Se vacancy, which introduces deep traps. In Se-rich material, the Se_{In} antisite is the dominant defect. Formation energies as a function of chemical potential for intrinsic defects in InSe were shown in Fig. 2. 10[38].

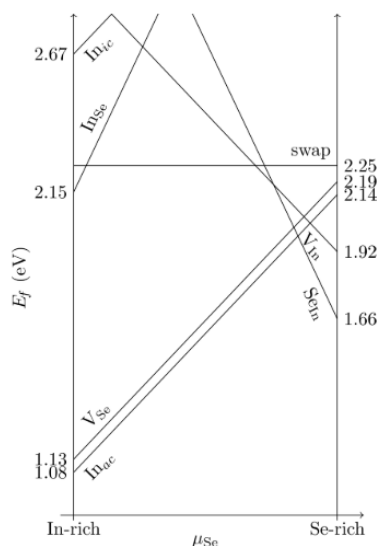


Fig. 2.10 Formation energies as a function of chemical potential for intrinsic defects[38].

2.4 References

- [1] X.-L. Shi, J. Zou, Z.-G. Chen, Advanced Thermoelectric Design: From Materials and Structures to Devices, Chem. Rev. (2020). <https://doi.org/10.1021/acs.chemrev.0c00026>.
- [2] P.H. Ngan, D.V. Christensen, G.J. Snyder, L.T. Hung, S. Linderorth, N. Van Nong, N. Pryds, Towards high efficiency segmented thermoelectric uncouples, Phys. Status

- Solids Appl. Mater. Sci. 211 (2014) 9–17. <https://doi.org/10.1002/pssa.201330155>.
- [3] G.J. Snyder, T.S. Ursell, Thermoelectric efficiency and compatibility, *Phys. Rev. Lett.* 91 (2003) 148301/1-148301/4. <https://doi.org/10.1103/PhysRevLett.91.148301>.
- [4] R. Venkatasubramanian, E. Siivola, T. Colpitts, B. O' Quinn, Thin-film thermoelectric devices with high room-temperature figures of merit, *Mater. Sustain. Energy A Collect. Peer-Reviewed Res. Rev. Artic. from Nat. Publ. Gr.* (2010) 120–125. https://doi.org/10.1142/9789814317665_0019.
- [5] L. Hu, T. Zhu, X. Liu, X. Zhao, Point defect engineering of high-performance bismuth-telluride-based thermoelectric materials, *Adv. Funct. Mater.* 24 (2014) 5211–5218. <https://doi.org/10.1002/adfm.201400474>.
- [6] S. Il Kim, K.H. Lee, H.A. Mun, H.S. Kim, S.W. Hwang, J.W. Roh, D.J. Yang, W.H. Shin, X.S. Li, Y.H. Lee, G.J. Snyder, S.W. Kim, Dense dislocation arrays embedded in grain boundaries for high-performance bulk thermoelectrics, *Science* (80-.). 348 (2015) 109–114. <https://doi.org/10.1126/science.aaa4166>.
- [7] Z. Ali, S. Butt, C. Cao, F.K. Butt, M. Tahir, M. Tanveer, I. Aslam, M. Rizwan, F. Idrees, S. Khalid, Thermochemically evolved nanoplatelets of bismuth selenide with enhanced thermoelectric figure of merit, *AIP Adv.* 4 (2014). <https://doi.org/10.1063/1.4902159>.
- [8] S. Gupta, N. Vijayan, A. Krishna, K. Thukral, K.K. Maurya, S. Muthiah, A. Dhar, B. Singh, G. Bhagavannarayana, Enhancement of thermoelectric figure of merit in Bi₂Se₃ crystals through a necking process, *J. Appl. Crystallogr.* 48 (2015) 533–541. <https://doi.org/10.1107/S1600576715003350>.
- [9] L.D. Zhao, S.H. Lo, Y. Zhang, H. Sun, G. Tan, C. Uher, C. Wolverton, V.P. Dravid, M.G. Kanatzidis, Ultralow thermal conductivity and high thermoelectric figure of merit

- in SnSe crystals, *Nature*. 508 (2014) 373–377. <https://doi.org/10.1038/nature13184>.
- [10] J.S. Rhyee, K.H. Lee, S.M. Lee, E. Cho, S. Il Kim, E. Lee, Y.S. Kwon, J.H. Shim, G. Kotliar, Peierls distortion as a route to high thermoelectric performance in In₄Se₃ crystals, *Nature*. 459 (2009) 965–968. <https://doi.org/10.1038/nature08088>.
- [11] S. Bhattacharya, A. Bohra, R. Basu, R. Bhatt, S. Ahmad, K.N. Meshram, A.K. Debnath, A. Singh, S.K. Sarkar, M. Navneethan, Y. Hayakawa, D.K. Aswal, S.K. Gupta, High thermoelectric performance of (AgCrSe₂)_{0.5}(CuCrSe₂)_{0.5} nano-composites having all-scale natural hierarchical architectures, *J. Mater. Chem. A*. 2 (2014) 17122–17129. <https://doi.org/10.1039/c4ta04056b>.
- [12] M. Ohta, S. Satoh, T. Kuzuya, S. Hirai, M. Kunii, A. Yamamoto, Thermoelectric properties of Ti_{1+x}S₂ prepared by CS₂ sulfurization, *Acta Mater.* 60 (2012) 7232–7240. <https://doi.org/10.1016/j.actamat.2012.09.035>.
- [13] R. Nunna, F. Gascoin, E. Guilmeau, Tuned thermoelectric properties of TiS_{1.5}Se_{0.5} through copper intercalation, *J. Alloys Compd.* 634 (2015) 32–36. <https://doi.org/10.1016/j.jallcom.2015.02.021>.
- [14] H. Liu, X. Yuan, P. Lu, X. Shi, F. Xu, Y. He, Y. Tang, S. Bai, W. Zhang, L. Chen, Y. Lin, L. Shi, H. Lin, X. Gao, X. Zhang, H. Chi, C. Uher, Ultrahigh thermoelectric performance by electron and phonon critical scattering in Cu₂Se_{1-x}I_x, *Adv. Mater.* 25 (2013) 6607–6612. <https://doi.org/10.1002/adma.201302660>.
- [15] L. Zhao, X. Wang, F.Y. Fei, J. Wang, Z. Cheng, S. Dou, J. Wang, G.J. Snyder, High thermoelectric and mechanical performance in highly dense Cu_{2-x}S bulks prepared by a melt-solidification technique, *J. Mater. Chem. A*. 3 (2015) 9432–9437. <https://doi.org/10.1039/c5ta01667c>.

- [16] K. Chrissafis, N. Vouroutzis, K.M. Paraskevopoulos, N. Frangis, C. Manolikas, Phase transformation in CuAgSe: A DSC and electron diffraction examination, *J. Alloys Compd.* 385 (2004) 169–172. <https://doi.org/10.1016/j.jallcom.2004.04.119>.
- [17] S. Ishiwata, Y. Shiomi, J.S. Lee, M.S. Bahramy, T. Suzuki, M. Uchida, R. Arita, Y. Taguchi, Y. Tokura, Extremely high electron mobility in a phonon-glass semimetal, *Nat. Mater.* 12 (2013) 512–517. <https://doi.org/10.1038/nmat3621>.
- [18] A.J. Hong, L. Li, H.X. Zhu, X.H. Zhou, Q.Y. He, W.S. Liu, Z.B. Yan, J.M. Liu, Z.F. Ren, Anomalous transport and thermoelectric performances of CuAgSe compounds, *Solid State Ionics.* 261 (2014) 21–25. <https://doi.org/10.1016/j.ssi.2014.03.025>.
- [19] P.F. Qiu, X.B. Wang, T.S. Zhang, X. Shi, L.D. Chen, Thermoelectric properties of Te-doped ternary CuAgSe compounds, *J. Mater. Chem. A.* 3 (2015) 22454–22461. <https://doi.org/10.1039/c5ta06780d>.
- [20] N.D. Raranskii, V.N. Balazyuk, Z.D. Kovalyuk, N.I. Mel’Nik, V.B. Gevik, Crystal growth and elastic properties of In_2Se_3 , *Inorg. Mater.* 47 (2011) 1174–1177. <https://doi.org/10.1134/S0020168511110203>.
- [21] K. Osamura, Y. Murakami, Y. Tomiie, Crystal structure of α - and β -Indium Selenide, In_2Se_3 , *J. Phys. Society Japan.* 21 (1966) 1848.
- [22] H. Peng, C. Xie, D.T. Schoen, Y. Cui, Large anisotropy of electrical properties in layer-structured In_2Se_3 nanowires, *Nano Lett.* 8 (2008) 1511–1516. <https://doi.org/10.1021/nl080524d>.
- [23] G. Han, Z.G. Chen, J. Drennan, J. Zou, Indium selenides: Structural characteristics, synthesis and their thermoelectric performances, *Small.* 10 (2014) 2747–2765. <https://doi.org/10.1002/sml.201400104>.

- [24] S. Popovic, A. Tonejc, B. Grzeta-Plenkovic, B. Celustka, R. Trojko, Revised and new crystal data for indium selenides, *J. Appl. Cryst.* 12 (1979) 416–420.
- [25] J.L. Cui, X.J. Zhang, Y. Deng, H. Fu, Y.M. Yan, Y.L. Gao, Y.Y. Li, Modified structures and improved thermoelectric property in Ag-added polycrystalline In_2Se_3 , *Scr. Mater.* 64 (2011) 510–512. <https://doi.org/10.1016/j.scriptamat.2010.11.026>.
- [26] J.H. Yim, H.H. Park, H.W. Jang, M.J. Yoo, D.S. Paik, S. Baek, J.S. Kim, Thermoelectric properties of indium-selenium nanocomposites prepared by mechanical alloying and spark plasma sintering, *J. Electron. Mater.* 41 (2012) 1354–1359. <https://doi.org/10.1007/s11664-012-1940-x>.
- [27] D.A. Bandurin, A. V. Tyurnina, G.L. Yu, A. Mishchenko, V. Zólyomi, S. V. Morozov, R.K. Kumar, R. V. Gorbachev, Z.R. Kudrynskyi, S. Pezzini, Z.D. Kovalyuk, U. Zeitler, K.S. Novoselov, A. Patanè, L. Eaves, I. V. Grigorieva, V.I. Fal'Ko, A.K. Geim, Y. Cao, High electron mobility, quantum Hall effect and anomalous optical response in atomically thin InSe , *Nat. Nanotechnol.* 12 (2017) 223–227. <https://doi.org/10.1038/nnano.2016.242>.
- [28] A. Politano, G. Chiarello, R. Samnakay, G. Liu, B. Gürbulak, S. Duman, A.A. Balandin, D.W. Boukhvalov, The influence of chemical reactivity of surface defects on ambient-stable InSe -based nanodevices, *Nanoscale.* 8 (2016) 8474–8479. <https://doi.org/10.1039/c6nr01262k>.
- [29] M. Küpers, P.M. Konze, A. Meledin, J. Mayer, U. Englert, M. Wuttig, R. Dronskowski, Controlled Crystal Growth of Indium Selenide, In_2Se_3 , and the Crystal Structures of α - In_2Se_3 , *Inorg. Chem.* 57 (2018) 11775–11781. <https://doi.org/10.1021/acs.inorgchem.8b01950>.

- [30] I. Grimaldi, T. Gerace, M.M. Pipita, I.D. Perrotta, F. Ciuchi, H. Berger, M. Papagno, M. Castriota, D. Pacilé, Structural investigation of InSe layered semiconductors, *Solid State Commun.* 311 (2020) 113855. <https://doi.org/10.1016/j.ssc.2020.113855>.
- [31] S. Lei, L. Ge, S. Najmaei, A. George, R. Kappera, J. Lou, M. Chhowalla, H. Yamaguchi, G. Gupta, R. Vajtai, A.D. Mohite, P.M. Ajayan, Evolution of the electronic band structure and efficient photo-detection in atomic layers of InSe, *ACS Nano.* 8 (2014) 1263–1272. <https://doi.org/10.1021/nn405036u>.
- [32] J. Felton, J. Felton, E. Blundo, S. Ling, J. Glover, Z.R. Kudrynskyi, O. Makarovskiy, Z.D. Kovalyuk, E. Besley, G. Walker, A. Polimeni, A. Patané, The interaction of hydrogen with the van der Waals crystal γ -InSe, *Molecules.* 25 (2020) 1–16. <https://doi.org/10.3390/molecules25112526>.
- [33] X. Hou, S. Chen, Z. Du, X. Liu, J. Cui, Improvement of the thermoelectric performance of InSe-based alloys doped with Sn, *RSC Adv.* 5 (2015) 102856–102862. <https://doi.org/10.1039/c5ra23023c>.
- [34] M. Alidoosti, D.N. Esfahani, R. Asgari, Charge density wave and superconducting phase in monolayer InSe, (2020) 1–10.
- [35] H. Henck, D. Pierucci, J. Zribi, F. Bisti, E. Papalazarou, J.C. Girard, J. Chaste, F. Bertran, P. Le Fèvre, F. Sirotti, L. Perfetti, C. Giorgetti, A. Shukla, J.E. Rault, A. Ouerghi, Evidence of direct electronic band gap in two-dimensional van der Waals indium selenide crystals, *Phys. Rev. Mater.* 3 (2019) 1–6. <https://doi.org/10.1103/PhysRevMaterials.3.034004>.
- [36] Y. Zhai, Q. Zhang, J. Jiang, T. Zhang, Y. Xiao, S. Yang, G. Xu, Thermoelectric properties of $\text{In}_{1.3-x}\text{Sn}_x\text{Se}$ prepared by spark plasma sintering method, *J. Alloys Compd.*

553 (2013) 270–272. <https://doi.org/10.1016/j.jallcom.2012.11.139>.

- [37] R. Haleoot, B. Hamad, Thermoelectric properties of doped β -InSe by Bi: First principle calculations, *Phys. B Condens. Matter.* 587 (2020) 412105. <https://doi.org/10.1016/j.physb.2020.412105>.
- [38] K.J. Xiao, A. Carvalho, A.H. Castro Neto, Defects and oxidation resilience in InSe, *Phys. Rev. B.* 96 (2017) 1–8. <https://doi.org/10.1103/PhysRevB.96.054112>.

Chapter 3. Experiments

3.1 PID temperature controller

The Proportional-Integral-Derivative (PID) controller is an instrument used in industrial control applications to regulate temperature, flow, pressure, and other process variables [1]. PID controllers use a control loop feedback mechanism to control process variables and are the most accurate and stable controller. A PID temperature controller, as its name implies, is a device used primarily to control temperature without extensive operator involvement. The principle is that the PID temperature controller continuously calculates an error value $e(t)$ as the difference between the setpoint value (SP) and the current measured value (PV) by a thermocouple. This error is used for three purposes; i) to process the present through the proportional term, ii) to recover errors from the past through the integral term, and iii) to avoid future errors through the derivative term. The controller attempts to minimize the error over time by adjusting control variables.

Figure 3.1 shows the PID controller close loop and working principle, where K_p , K_i , and K_d are the time constants of proportional, integral, and derivative terms.

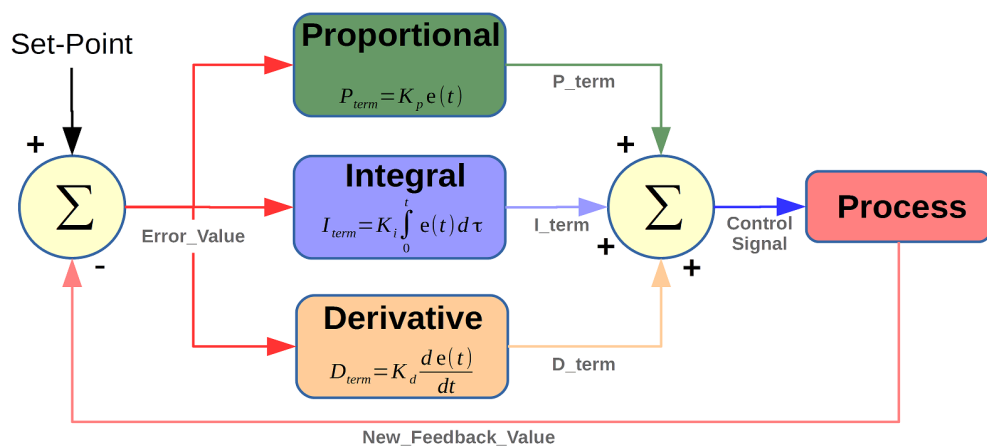


Fig. 3.1 A block diagram of a PID controller in a feedback loop.

Controllers that use PID programs can operate with a single term (P, I, D), a joined term (PI, PD), or all PID terms. However, the single and couple terms have many weaknesses, including the P controller cannot eliminate steady-state errors, a large D makes the system more sensitive to noise, and the PI controller can cause large overshoots and inadequate response. The controller's best performance can be obtained using these terms P, I, and D together, which are called PID controllers. The PI controller improves the PI controller by eliminating steady-state errors in the P controller, and the PID controller eliminates overshoots and speeds up response. The step response of the P, PI, and PID controllers is shown in Figure 3.2. This figure shows the best response and stability of a PID controller compared to other controllers.

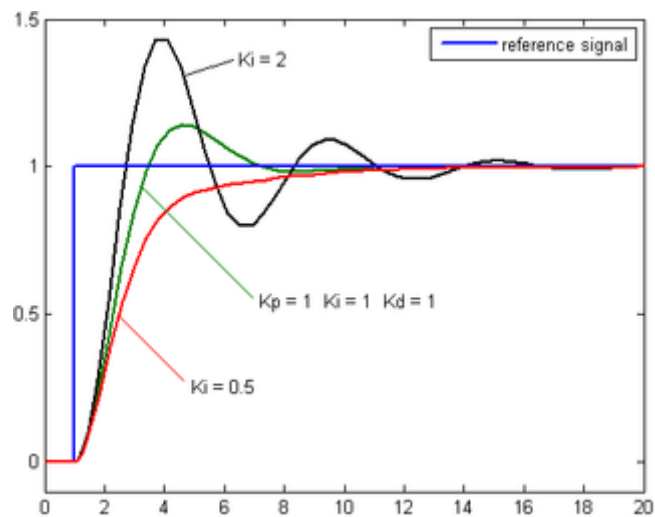


Fig. 3.2 Step response of P, PI, and PID controller.

3.2 Heat transfer mechanism

To use heat efficiently and control temperature accurately, it is necessary to understand the movement of heat and how it is transferred between objects. Heat transfer mechanisms are simply ways by which thermal energy can be transferred between objects, and they all rely on the basic principle that kinetic energy or heat wants to be at equilibrium or equal energy states. There are three different ways for heat transfer to occur: conduction, convection, and radiation.

First, heat conduction, also called diffusion, is the direct transfer of heat from one object to another. Conduction is the most effective means of heat transfer within a solid or between solid objects in thermal contact. The heat conduction is dependent on the thermal conductivity of materials. Materials can be classified into heat conductors and heat insulators. Metal is a perfect heat conductor with high thermal conductivity, while wood and glass fiber are excellent insulators. Second, convection is heat transfer through fluid (like air or water) motion. The difference between conduction and convection is the movement of the material carrier. Convection is the movement of thermal energy by moving a hot fluid. This movement usually occurs because of different densities. Warm particles are less dense, so hot particles move to cooler regions and cooler particles move to hotter regions. The fluid continues to move until equilibrium is reached. Third, radiation is the transfer of heat energy using photons in electromagnetic waves. All moving charged particles emit electromagnetic radiation. This emitted wave will travel until it hits another particle. The particle that receives this radiation will receive it as kinetic energy. Particles will receive and emit radiation even after everything is at the same temperature, but it is not noticed because the material is at equilibrium at this point. The Stefan-Boltzmann equation describes the rate of transfer of radiant energy:

$$Q = \varepsilon\sigma T^4$$

For the radiative transfer between two objects, the equation is as follows:

$$Q = \varepsilon\sigma F(T_a^4 - T_b^4)$$

Where Q is the heat flux, ε is the emissivity (unity for a black body), σ is the Stefan-Boltzmann constant, F is the view factor between two surfaces a and b , and T_a and T_b are the absolute temperatures for the two objects.

3.3 Single crystal growth

Growth from the melt by solidification is the most widely used method for preparing high-quality large single crystals. The fundamental concept of this technique has slowly cooled the liquid to its melting point. In this technique, apart from possible contamination from crucible materials and the surrounding atmosphere, no impurities are introduced in the growth process. The growth rate is usually much higher than possible by other methods. Single crystal defects strongly depend on how well the temperature is controlled. The growth from the melt can be sub-grouped into various techniques, such as Bridgman, Czochralski, Verneuil, Zone melting, Kyropoulos, and temperature gradient techniques. In this section, the Bridgman and the temperature gradient techniques are discussed in detail.

3.3.1 Bridgman technique (Bridgman-Stockbarger technique)

The Bridgman technique (also known as the Bridgman-Stockbarger technique) is one of the oldest techniques used to grow single crystals from the melt. This technique was invented by Bridgman in 1925 and modified by Stockbarger in 1936. Bridgman's technique's principle involves lowering a crucible through the furnace so that the solidification interface slowly rises along with the crucible, starting at the lowest point of the freezing crucible. First, the raw materials are weighed according to the appropriate stoichiometry, placed in an ampoule, evacuated, or added in an inert atmosphere, and sealed. Ampoules are usually made of quartz, Pyrex, alumina, graphite, and precious metals. After shielding, a hook is created at the top of the ampoule and connected to the motor via a high melting point wire. After maintaining the high temperature to complete the reaction between the elements to form the compound, slowly lower the ampoule from the hot part (above the melting point of the material) to the cold part (below the melting point of the material) of the furnace to solidify. The movement rates for such processes range from around 0.1 to 200 mm/h. A typical vertical Bridgman system is

shown in Fig. 3.1. A longitudinal temperature profile is established in the center of the furnace with a specific temperature gradient near the melting point of the material. The crystal growth with the vertical Bridgman method can use a seed or no seed. A without-seeded Bridgman method relies on random nucleation or self-nucleation to produce a single crystal that propagates to form one large crystal throughout the frozen charge. The formation of just one nucleus requires a small nucleation volume. Thus the crucibles are usually modeled with conical tips to meet nucleation criteria, as illustrated in Fig. 3.1. For a seeded Bridgman growth, the crucible shape is not essential. The flat bottom is usually made to contain the seed material. The most obvious requirement of the crucible is that it should not react with the crystal within the temperature range of crystal growth. It should also have a smaller thermal expansion coefficient than the crystal to avoid strain and stress-induced during the crucible cooling. There are two kinds of Bridgman furnaces; horizontal and vertical, corresponding to horizontal Bridgman technique and vertical Bridgman technique. Usually, the vertical Bridgman technique provides a higher quality crystal than the horizontal one.

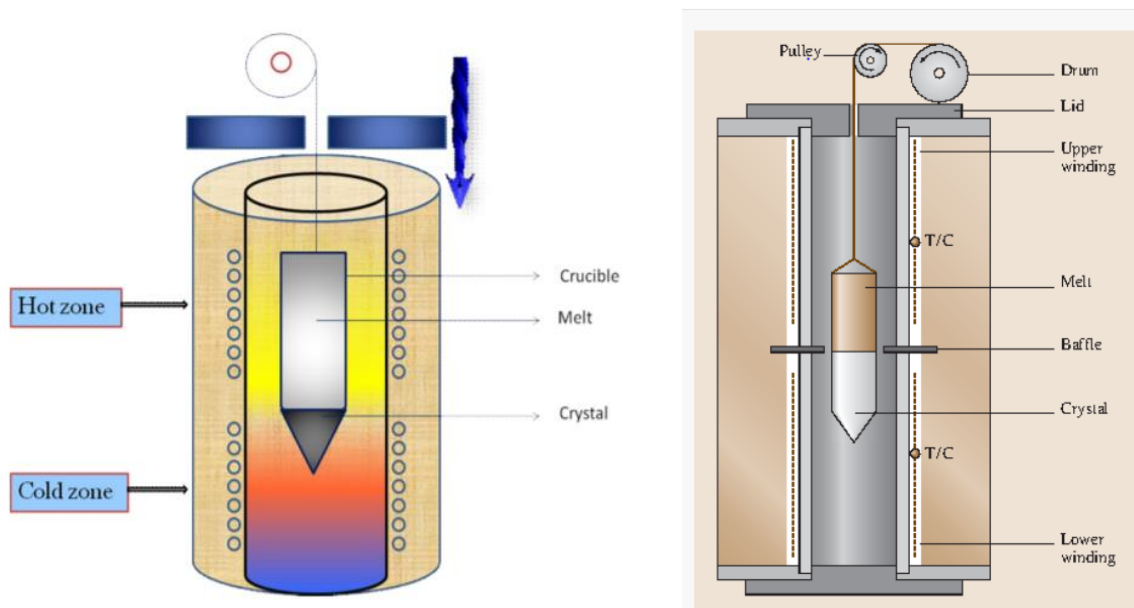


Fig. 3.3 The schematic of the Bridgman technique and the Stockbarger technique.

The Stockbarger technique is a modified Bridgman technique in which the furnace is divided into two zones, often separated by a baffle, producing a steeper temperature gradient between zones, as shown in Fig. 3.1b [2]. Note that the temperature gradient here can be adjusted by changing the density of the heating element or by using the convection phenomenon (for the vertical furnace). The Bridgman-Stockbarger technique exhibits many advantages: it does not require a seed to start growing, produces large and high-quality single crystal ingot, possibly grows sublimating material's compounds, and the crystal orientation can be controlled by adjusting the seed orientation (sharp tip of the ampoules). However, there are some disadvantages. The temperature and ampoule position is hard to adjust accurately due to ampoule fluctuations, manufacturing on an industrial scale is complex and challenging, and only one ampoule can be loaded at one time. As mentioned above, to produce an excellent thermoelectric single crystal ingot, we have to control well the defect type and defect density. Using the Bridgman-Stockbarger technique, we may optimize the amounts of elements loaded in the ampoule, the temperature gradient, and the speed of lowering the ampoule.

3.3.2 Temperature gradient technique

Using the same concept from the melt, the temperature gradient technique has been used to fabricate bulk single crystals. This technique uses the thermal convection phenomenon to create a temperature gradient. Figure 3.10a shows a schematic diagram of a vertical furnace. Without moving ampoules, the gradient temperature is only used for single crystal growth. The temperature was precisely controlled by an AC or DC power supply and a PID temperature controller. In the furnace, the heating wire is evenly wound around quartz. Due to the transparency of the quartz tube, heat radiation can efficiently conduct heat from the wire to the ampoule, creating a uniform cross-sectional temperature. A thermocouple is placed in the furnace near the ampoule to read the temperature at the sample location accurately. The following are the details of the growing process. First, the raw materials were weighted at the appropriate stoichiometry. The powders were then mixed, loaded into a quartz tube, evacuated, and sealed under the pressure of roughly 10^{-4} Torr. The ampoule was then evacuated and sealed inside another larger quartz ampoule to prevent oxidation that may occur when the inner ampoule is broken due to differences in the thermal expansion coefficients between materials and quartz and/or expansion of the material during the phase transition. The ampoule was then slowly heated to a high temperature above the melting point of materials. During the heating process, the raw materials interact to form a compound. To complete this reaction, the ampoule was kept at a high temperature for a long time. The ampoule was then slowly cooled down below the melting point of the compound. First, solidification occurs at the bottom of the ampoule, creating a single-crystal seed. As temperature continuously drops, a single crystal grows on the seed. Finally, a single crystal ingot is manufactured. Notice that the excess elements are floating on top of the ampoule. This method has many advantages over the Bridgeman method. Many ampoules can be loaded together in a single run with no moving

parts, making it extremely simple and easy to operate. Using the temperature gradient technique, we have successfully fabricated the excellent α -In₂Se₃ and β -InSe single crystals.

3.4 Transport properties measurement system in our lab

To determine the Seebeck coefficient, electrical conductivity, and carrier concentration in our lab, we have built our low- and high-temperature transport measurement systems. The low-

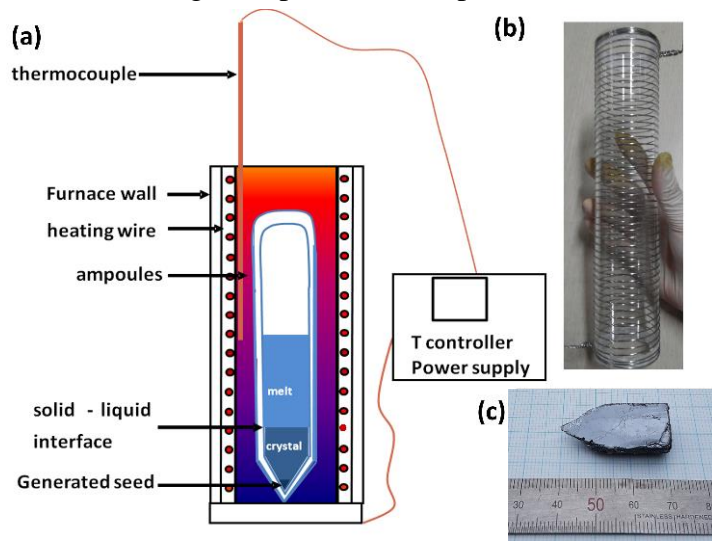


Fig. 3.4 (a) The furnace in the temperature gradient technique; (b) Heating wire of the furnace; (c) The photo of InSe single crystal.

temperature measurement system allows us to measure these parameters in the temperature range from 10 to 410 K (the extent to 450 K). The high-temperature measurement systems allow us to measure these transport parameters from room temperature to 1000 K (using liquid N₂ for cooling, the temperature can be started measure at 100 K).

3.4.1 Low-temperature measurement system

Electrical thermoelectric transport properties, including temperature-dependent Seebeck coefficient, electrical resistance, Hall effect, and magnetoresistance measurement, as a function of temperature, have been extensively studied in our home-made low-temperature physical properties measurement system (PPMS). The PPMS is composed of a vacuum chamber, rotary

pump, electro-magnet, cryostat system, Keithley source-meters. The photo image of PPMS equipment is presented in Fig 3.1. The rotary pump allows us to maintain the system under a low vacuum range of $\sim 10^{-3}$ Torr. The cryostat system includes the Lake Shore model 331 temperature controller, Displex (DE-202S, Advanced Research System, Inc.), heater, and temperature sensors (Silicon diode or resistance temperature detectors RTDs). The heater is designed after considering the impedance matching with the temperature controller and minimized its induced magnetic field. Keithley 182 nano voltmeter and model 2400 series source meter were set for electrical transport measurement. The Keithley 2400 source meter has the following capacity: source volt range (from 5 μ V to 200 V), measurement voltage (from 1 μ V to 211 V), source of current (from 50 pA to 1.05 A), measurement current (from 10 pA to 1.055 A), and measurement resistance (from 100 $\mu\Omega$ to 211 M Ω). The electromagnet (Walker LDJ Scientific Inc., USA) can generate a magnetic field to 1 Tesla (10000 Gauss). The model 182 sensitive digital voltmeter has the built-in standard IEEE-488 interface, which allows the instrument to communicate with a computer.

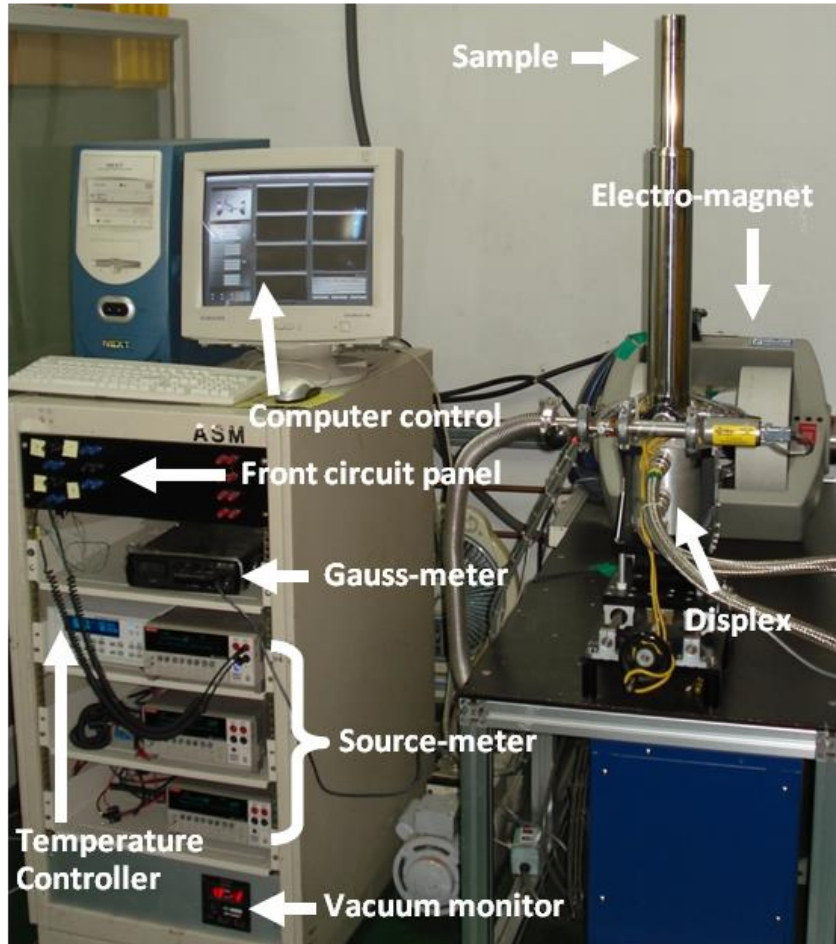


Fig. 3.5 Our home-made low-temperature physical properties measurement system (PPMS)

This measurement system can simultaneously measure two samples for resistance, Hall effect, and magnetoresistance measurements using a four-point probe configuration. Besides, Seebeck coefficient measurements using the two-probe method allow one sample each time. The schematic drawing of these measurements is shown in Fig. 3.2. In the Seebeck coefficient measurement, the ambient temperature is kept stable by the temperature controller. The temperature gradient is generated by a heater ($\sim 170 \Omega$) integrated into a cooper block. A K-type thermocouple is used to measure the temperature gradient. The thermoelectric voltage can be expressed by

$$\Delta V = S\Delta T + b(\Delta T)^2 + \dots \quad (3.1)$$

It measures steady-state thermoelectric voltages at exceedingly small intervals of gradient temperature to eliminate spurious thermal voltages in the circuit and ignore higher-order terms of ΔT . The Seebeck coefficient was determined by taking the slope of the ΔV vs. ΔT curve.

3.4.2 High-temperature measurement system

We designed the high-temperature transport measurement system with operating temperature from room temperature to 1000 K (using water for cooling) and from 100 K to 1000 K (using liquid N₂ for cooling).

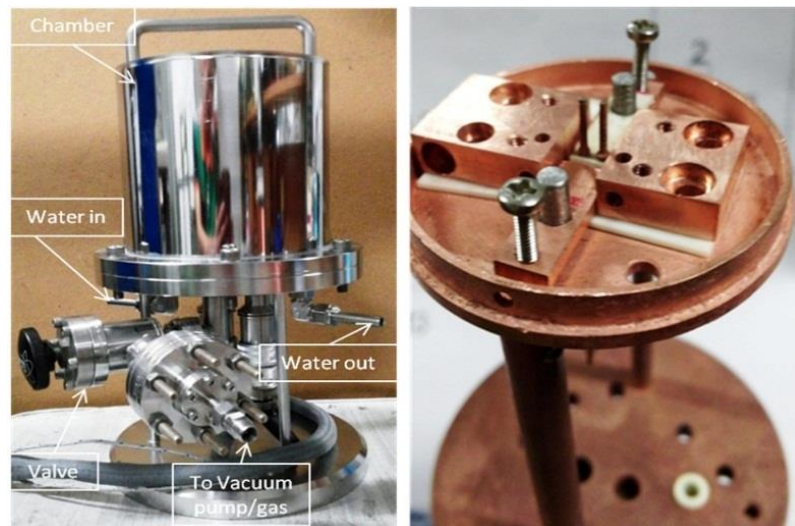


Fig. 3.6 The photo of our home-build high-temperature transport measurement system.

The measurement's principle was described as the same as a low-temperature system.

3.5 Characterizations

3.5.1 X-ray diffraction (XRD)

Our samples' crystal quality was examined by X-ray diffraction (XRD) experiments using Cu *K* α 1 radiation (0.154056 nm). The θ - 2θ scan was used to investigate the out of plane orientation and lattice constants of the samples.

In principle, in the XRD θ - 2θ scan, a diffraction peak appears when the incident beam satisfies two conditions: the diffraction plane has to be perpendicular to the crystallographic plane and the Bragg condition

$$2d \sin \theta = m\lambda \quad (3.32)$$

where d is the inter-planar distance, λ is the wavelength of the X-ray beam, and θ is the incident angle (angle between the incident beam and crystallographic plane). The position of peak (2θ) is dependent on d , while the intensity of peak is dependent on many factors: Structure factor (include form factor), Lorentz, polarization, multiplicity, temperature factors. The XRD peak's intensity is calculated as

$$I(hkl) = |S(hkl)|^2 \times M_{hkl} \times LP(\theta) \times TF(\theta) \quad (3.33)$$

where $S(hkl)$ is the structure factor, M_{hkl} is the multiplicity factor, $LP(\theta)$ is Lorentz, and Polarization factors, $TF(\theta)$ is the temperature factor (displacement parameter).

3.5.2 Scanning Tunneling Microscope (STM)

A scanning tunneling microscope (STM) is an instrument for imaging surfaces at the atomic level. The STM works by scanning an extremely sharp metal wire tip over a surface. We can image the surface at an extremely small scale – down to resolving individual atoms. Microscopes are built for use in ultra-high vacuum ($< 10^{-10}$ Torr) at liquid N₂ temperature (79 K), but variants exist for operating at room temperature.

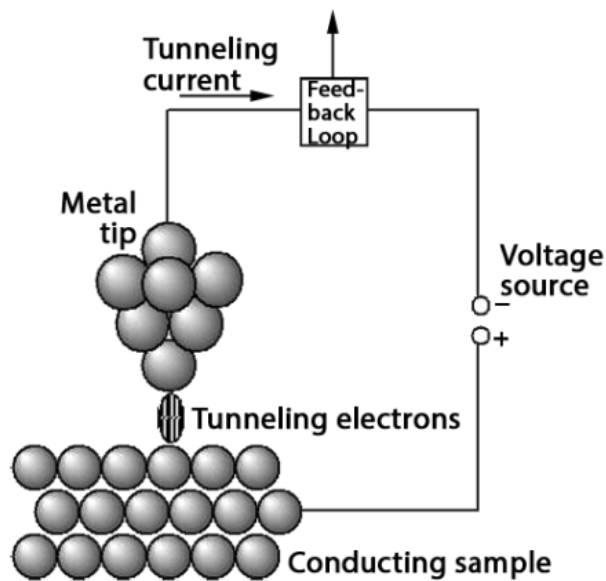


Fig. 3.7 The schematic of STM

The STM is based on several principles, including quantum tunneling and piezoelectric effect. One is the quantum mechanical effect of tunneling. When the tip is brought near the surface, an electrical voltage applied between the tip and surface sample allows electrons to tunnel through the vacuum, separating them. It is this effect that allows us to “see” the surface. Another principle is the piezoelectric effect that allows us to precisely scan the tip with angstrom-level control. Lastly, a feedback loop is required, which monitors the tunneling current and coordinates the current and the positioning of the tip.

In this work, we used the home-built low-temperature STM system ((base pressure of $\sim 7 \times 10^{-11}$ Torr) to investigate the surface structure of β -InSe single crystal at 280 and 80 K.

3.5.3 Raman spectroscopy

Raman spectroscopy is a non-destructive chemical analysis technique that provides detailed information about chemical structure, phase and polymorphy, crystallinity, and molecular interactions. It is based upon the interaction of light with the chemical bonds within a material.

Raman is a light scattering technique whereby a molecule scatters incident light from a high-intensity laser light source. Most of the scattered light is at the same wavelength (same energy) as the laser source and does not provide useful information – this is called Rayleigh Scatter. However, a small amount of light is scattered at a different wavelength (smaller or larger energy), which depends on the material’s chemical structure – this is called Raman Scatter [4].

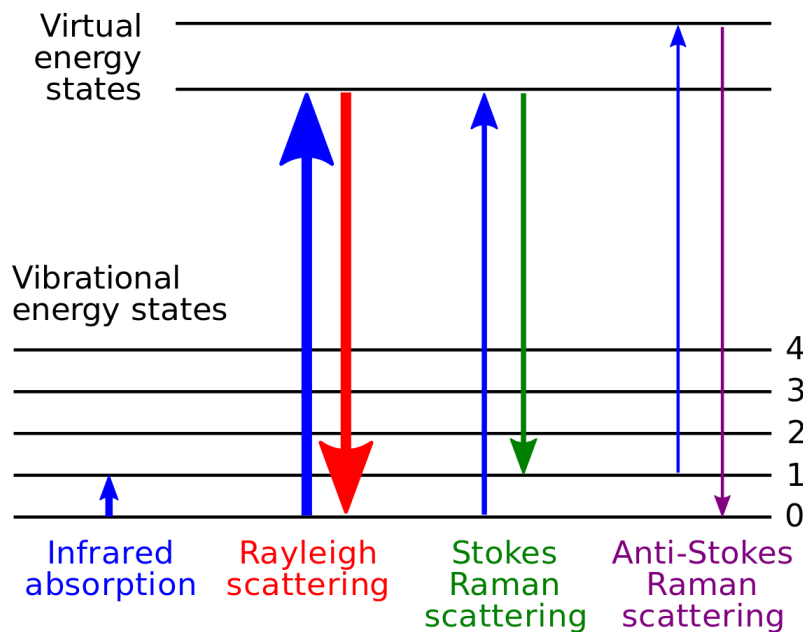


Fig. 3.8 Energy-level diagrams showing the states involved in Raman spectra

Raman shifts are typically reported in wavenumbers, which have units of inverse wavelength, as this value is directly related to energy. To convert between spectral wavelength and wavenumbers of the shift in the Raman spectrum, the following equation can be used:

$$\Delta\tilde{\nu} (cm^{-1}) = \left(\frac{1}{\lambda_0(nm)} - \frac{1}{\lambda_1(nm)} \right) \times \frac{10^7(nm)}{(cm)}$$

where, $\Delta\tilde{\nu}$ is the Raman shift expressed in wavenumber, λ_0 is the excitation wavelength, and λ_1 is the Raman scattering wavelength.

A Raman spectrum features a number of peaks, showing the intensity and wavelength position of the Raman scattered light. Each peak corresponds to a specific molecular bond vibration and provides information about chemical structure, phase, symmetry, and impurity, etc.[5]. In this work, this measurement was performed by the DXR Raman microscope (Thermo Scientific, USA), which was equipped with a 532 nm laser. The laser power was 5 mW to obtain a good signal to noise ratio.

3.5.4 Photoluminescence (PL)

Photoluminescence (PL) is when light energy, or photons, stimulate the emission of a photon from any matter. It is a non-contact, non-destructive method of probing the electronic structure of materials. In essence, light is directed onto a sample, where it is absorbed, and where a process called photo-excitation can occur. The photo-excitation causes the material to jump to a higher electronic state and then release energy (photons) as it relaxes and returns to a lower energy level. The emission of light or luminescence through this process is photoluminescence, PL [6,7].

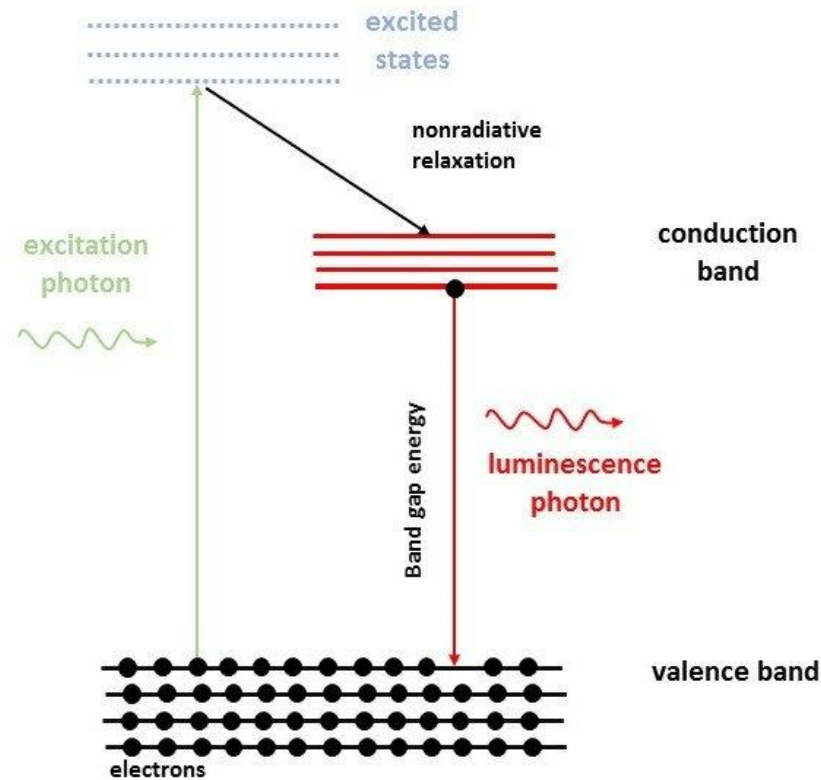


Fig. 3.9 Schematic representation of the photoluminescence excitation

PL spectroscopy is a widely used technique for characterizing the optical and electronic properties of the material, such as bandgap determination, impurity levels, defect detection, recombination mechanisms, material quality, and surface structure excited states. In this study, a 473 nm Ar-ion laser was used for PL studies at room temperature.

3.5.5 Specific heat capacity

Heat capacity is defined as the ratio of the amount of energy transferred to a material and the change in temperature that is produced:

$$C = Q/\Delta T$$

Where C is heat capacity, Q is energy, and ΔT is the temperature change.

The specific heat capacity (C_p) is the amount of energy that must be added to

3.5.6 Thermal diffusivity and thermal conductivity: LFA, ZEM 3

Thermal conductivity (κ W/m-K) is a thermophysical measure of how much heat is transferred through a material by the conductive flow. It can be determined the thermal conductivity as the ratio of the quantity of heat per unit area to the temperature gradient. Determining thermal conductivity is an indirect measurement. The thermal conductivity of a material is proportional to its thermal diffusivity. The thermal diffusivity (D with the unit mm^2/s) is a material-specific property for characterizing the unsteady state of heat transfer. This value describes how well the heat could diffuse through the material. In this work, this measurement was performed by Netzsch LFA457. The thermal conductivity is calculated by

$$\kappa = D\rho C_p \quad (3.35)$$

where D is thermal diffusivity, ρ is mass density, and C_p is specific heat.

The thermal diffusivity is measured with the flash method. The sample is selected so that its cross-section is large compared with its thickness. If a pulsed laser irradiates its face, the temperature fluctuations at the opposite face are observed using an infrared sensor. Thermal diffusivity is determined from the thickness (d) of the sample and the time taken to reach half of the maximal temperature increase ($t_{1/2}$) by following the equation

$$D = \frac{1.37d^2}{\pi^2 t_{1/2}}$$

The mass density can be determined by using an Archimedes' method with any shape. To do that, we measure the weight of samples in air and DI water (mass density = 1000 kg/m^3). The mass density of the sample is determined by

$$\rho_0 = \frac{m_0}{m_0 - m} \rho_{DI}$$

where ρ_0 is the mass density of the sample in air, ρ_{DI} is the mass density of DI water, m is the

weight of sample in DI water, and m_0 is the weight of the sample in the air. The primary source of error is bubbles on the surface of the sample. To conduct measurement accurately, we need a smooth surface and a large enough sample.

3.6 Measurement's errors

Every measurement has inherent uncertainty. Therefore, we need to indicate the reliability of measurements and the uncertainties of the results calculated from these measurements. To better understand the outcome of experimental data, the experimenter can only make sure the error is as small as possible and estimate the error's magnitude. There are generally two different types of errors: random (or chance) errors and systematic (or biased) errors. First, a random error makes the measured value both smaller and more extensive than the real value; precision errors. Random error often occurs when instruments are pushed to their limits. Random error cannot be avoided; it is part of the measuring process. Uncertainties are a measure of random errors. To minimize this kind of error, we may repeat the experiment often and take average by appropriate statistics equations. Second, systematic error is related to imperfect calibration of measurement instruments, changes in the environment that interfere with the measurement process, and imperfect observation methods. A systematic error makes the measured value always smaller or larger than the actual value, but not both. Accuracy is a measure of systematic error. To minimize this error, we can calibrate the measurement instruments or repeatedly repeat the experiment to be familiar with the experiment.

We used the home build high-temperature transport measurement system and UlvacRiko ZEM-3 instrument to measure the Seebeck coefficient and electrical conductivity in this work. The thermal diffusivities were measured by laser flash analysis LFA instrument (model: LFA-457, NETZSCH, Germany). The standard uncertainties of UlvacRiko ZEM-3 were reported by the company: 5% for Seebeck coefficient and electrical conductivity; and about 15% for power

factor. The LFA-457 instrument gave an uncertainty of thermal conductivity of 5% (estimated value). The uncertainties of our home build high-temperature transport measurement system were calculated and reported [3]. This section represents the calculation for these uncertainties.

3.6.1 Electrical conductivity measurement's errors

The electrical conductivity can be calculated by

$$\sigma = \frac{1}{\rho} = \frac{l}{Rab}$$

Where ρ is electrical resistivity, R is electrical resistance, l is length (distance between two voltage probes in the collinear four-probe configuration mentioned above), and a and b are the width and thickness of the sample. Take natural logarithm both sides of this equation we have

$$\sigma = \frac{1}{\rho} = \frac{l}{Rab}$$

$$\ln \sigma = \ln l - \ln R - \ln a - \ln b$$

Take derivative both sides

$$d(\ln \sigma) = d(\ln l) - d(\ln R) - d(\ln a) - d(\ln b)$$

$$\frac{d\sigma}{\sigma} = \frac{dl}{l} - \frac{dR}{R} - \frac{da}{a} - \frac{db}{b}$$

Use the letter “ Δ ” instead of the letter “ d ”, at average values of quantities, consider only maximum value, we have

$$\frac{\Delta\sigma}{\bar{\sigma}} = \frac{\Delta l}{\bar{l}} + \frac{\Delta R}{\bar{R}} + \frac{\Delta a}{\bar{a}} + \frac{\Delta b}{\bar{b}}$$

Here, we neglected the uncertainty of resistance given by the Keithley model 2400 (less than 0.1%). Our home build measurement system's typical sample size is $l = 2 \text{ mm}$, $a = 2 \text{ mm}$, and $b = 0.3 \text{ mm}$. The uncertainty of rulers is $\Delta l = \Delta a = \Delta b = 0.01 \text{ mm}$. We have

$$\frac{\Delta\sigma}{\bar{\sigma}} = \frac{0.01}{2} + \frac{0.01}{2} + \frac{0.01}{3} = 0.043 = 4.3\%$$

The error for electrical conductivity is 4.3%.

3.6.2 Seebeck coefficient measurement's errors

We used the repeating measurement method to determine the error at room temperature [3]. The reference material is Bismuth (Bi) polycrystalline. The measurement was repeated 18 times and was analyzed using the fitting data technique, as shown in Fig. 3.21. We determined Seebeck coefficients from the linear slope of ΔV vs. ΔT curves. The measured Seebeck coefficient of polycrystalline Bi is $-57.7 \pm 0.76 \mu\text{V/K}$. The standard error from the linear fitting is 1.3%. Note that the Seebeck coefficient of Bi single crystal is $-51.4 \mu\text{V/K}$ along the perpendicular to the three-fold axis and $-102.7 \mu\text{V/K}$ along parallel to the three-fold axis. The Seebeck coefficient of the reported polycrystalline Bi is $-60 \mu\text{V/K}$ at 300 K. The slight difference between the measured and reported values is due to the sample quality such as grain size, purity, etc.

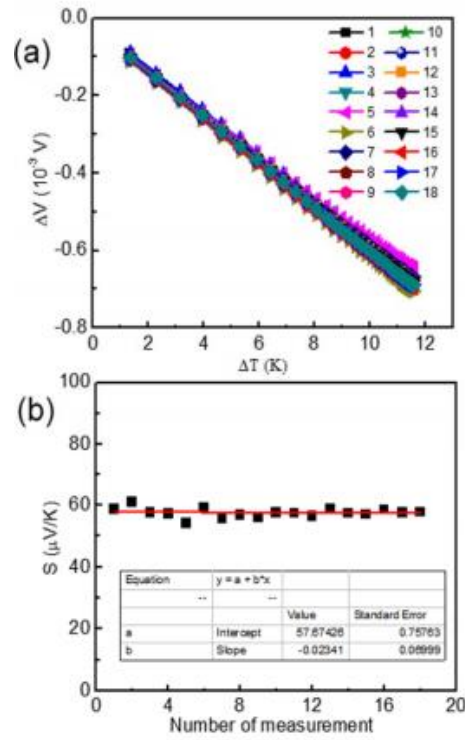


Fig. 3.10 (a) ΔV vs. ΔT at 300 K of polycrystalline Bi and (b) measurement' error.

3.6.3 Thermal conductivity measurement's errors

The laser flash analysis (LFA) Netzsch LFA 457 measurement system was used to determine the thermal diffusivity of samples. The reported error for this system is $\pm 3\%$.

3.6.4 Power factor's errors

The power factor is calculated from the Seebeck coefficient and electrical conductivity as

$$PF = S^2 \sigma$$

The uncertainty of the power factor is calculated using the rules of indirect measurement's error calculation.

$$PF = S^2 \sigma$$

$$\ln PF = 2 \ln S + \ln \sigma$$

$$\frac{\Delta PF}{PF} = 2 \frac{\Delta S}{S} + \frac{\Delta \sigma}{\sigma} = 2 \times 0.013 + 0.043 = 0.069 = 6.9\%$$

3.6.5 Figure of merit's error

The thermoelectric figure of merit is calculated by

$$ZT = \frac{PF}{\kappa} T$$

$$\ln ZT = \ln PF + \ln T - \ln \kappa$$

$$\frac{\Delta ZT}{ZT} = \frac{\Delta PF}{PF} + \frac{\Delta \kappa}{\kappa} = 0.069 + 0.03 = 0.099 = 9.9\%$$

Here κ is thermal conductivity, and T is the absolute temperature (the uncertainty of T is neglected).

3.6.6 Errors of ZEM 3

Apart from samples in this work, the electrical resistivity and Seebeck coefficient were measured using an Ulvac Riko ZEM-3 instrument under a helium atmosphere from room temperature to 923 K. The uncertainty for Seebeck coefficient, electrical conductivity, and ZT are 5%, 10%, and 20%, respectively.

3.7 References

[1] <http://www.digikey.com/en/pdf/a/atmel/avr221-discrete-pid-controller-on-tinyavr-and-megaavr-devices>.

[2] D. R. Lovett, semimetals, and narrow bandgap semiconductors, p. 28-30 London Pion limited (1977).

[3] A.T. Duong, V.Q. Nguyen, G. Duvjir, V.T. Duong, S. Kwon, J.Y. Song, J.K. Lee, J.E. Lee, S.D. Park, T. Min, J.W. Lee, J. Kim, S. Cho, *Nat. Commun.* **7**, 13713 (2016).

[4] https://en.wikipedia.org/wiki/Raman_spectroscopy.

[5] https://www.horiba.com/en_en/raman-imaging-and-spectroscopy/.

[6] <https://en.wikipedia.org/wiki/Photoluminescence>.

[7] <https://cnx.org/contents/uieDnVBC@25.2:gbsDEZju@2/Photoluminescence-Spectroscopy-and-its-Applications>.

Chapter 4. Carrier control in CuAgSe by growth process or doping

CuAgSe is a promising thermoelectric material whose p-type and n-type thermoelectric figure of merit, ZT , values are relatively high (0.95 and 0.70, respectively). It exhibits native n-type conduction, while p-type conduction is present in non-stoichiometric CuAgSe. Here, we report that the carrier type in CuAgSe semiconductors can be effectively controlled by changing the growth process or doping. We were able to switch the carrier type of CuAgSe from the native n-type to the non-stoichiometric p-type by increasing the soaking time during growth. In contrast, the n-type conduction was always observed when Ni, Co, and Zn were doped into the host lattices. We obtained a maximum ZT value of 0.69 at 623 K in undoped n-type CuAgSe. Zn is a promising dopant for n-type CuAgSe with a ZT value of 0.68 at 623 K, which can be further optimized. Our work provided a simple and effective technique for producing both single-phase n- and p-type CuAgSe.

4.1 Introduction

Thermoelectric (TE) materials have attracted interest for direct energy conversion between heat and electricity. The efficiency of heat conversion is proportional to the thermoelectric figure of merit of the TE material, ZT , which is defined as the relation, $ZT = (S^2\sigma/\kappa)T$, where S is the Seebeck coefficient, σ is the electrical conductivity, κ is the thermal conductivity ($\kappa = \kappa_e + \kappa_L$ where κ_e is the electronic thermal conductivity and κ_L is the lattice thermal conductivity), and T is the absolute temperature. A material with both a large Seebeck coefficient, high electrical conductivity, and low thermal conductivity is considered a good TE material [1,2]. However, such requirements are difficult to meet due to the interdependent relationship of the

parameters. One strategy of optimizing ZT proposed by Slack is based on the concept of phonon-glass electron-crystal (PGEC) [3]. The PGEC concept describes the essential features for an ideal TE material with both crystal-like features for good electronic properties and glass-like features for low lattice thermal conductivity [4,5].

Recently, an extension of the PGEC concept called phonon-liquid electron-crystal (PLEC) has been proposed. This concept is based on the liquid-like behavior of superionic conductors, which exhibit extremely low lattice thermal conductivity. By applying this concept, the lattice thermal conductivity of the material can be reduced significantly, while its power factor ($S^2\sigma$) is not seriously degraded. Non-stoichiometric superionic copper selenide (Cu_{2-x}Se) and copper sulfide (Cu_{2-x}S) are typical PLEC materials exhibiting maximum ZT values of 1.6 and 1.7 at 1000 K, respectively [6,7]. The high ZT values of the PLEC materials have stimulated the search for new high-performance TE materials in other superionic conductors.

CuAgSe (CAS) is a superionic material that is also a robust candidate for the PLEC concept [8–11]. Like Cu_2Se , CAS has two temperature-dependent phases: (i) a low-temperature β -phase and (ii) a high-temperature α -phase [12,13]. At temperatures below 470 K, the low-temperature β -CAS phase is a semi-metal with alternating stacks of the Ag and CuSe layers, allowing ultrahigh mobility of about $20,000 \text{ cm}^2\text{V}^{-1}\text{s}^{-1}$ at 10 K [14]. This characteristic provides the outstanding “electron-crystal” character of β -CAS. On the other hand, β -CAS is expected to display glass-like or even liquid-like thermal transport characteristics due to its complex crystal structure and atomic-lattice disorder [11]. At temperatures above 470 K, the high-temperature α -CAS phase is a semiconductor with a crystal structure similar to the superionic Cu_2Se . In the α -CAS, the mobile Ag/Cu cations randomly distribute among the Se face-centered cubic framework. This distribution results in a low lattice thermal conductivity in α -CAS (even lower than that of Cu_2Se) due to both the random half-substitution of Cu^+ ions by

Ag⁺ ions and the higher degree of occupation disorder [9,10]. To date, there have been some reports on the thermoelectric properties of CAS with both n-type and p-type conduction. Qiu's group [11] has doped Te into Se-sites and observed a maximum ZT value of 0.7 at 450 K for n-type CuAgSe_{0.95}Te_{0.05}. Hong et al. [12] have reported on the thermoelectric properties of p-type CuAgSe with $ZT = 0.95$ at 623 K. Producing both n-type and p-type conduction in the same semiconductor material is ideal for thermoelectric applications due to their similar physical and thermal properties, such as melting point, thermal expansion coefficient... It has been reported that Bi₂Te₃ exhibited n-type (p-type) conduction in Te (Bi) excessive conditions [15]. Recently, the p and n control was successfully achieved in Cr_{2+x}Se system. The material presented p-type conduction in stoichiometric, Cr deficient, and slight Cr excessive conditions ($x < 0.04$), while the n-type conduction was achieved in the larger Cr excessive conditions ($x > 0.06$) [16]. The stoichiometric CAS has been reported to always show n-type conduction, while the p-type conduction is only present in the non-stoichiometric CAS. However, it is difficult to synthesize the non-stoichiometric p-type CAS without secondary phases. To the best of our knowledge, there have been no reports focusing on the control of carrier type in CAS.

In this study, we report a simple and effective way to control the carrier type of single-phase CAS by adjusting the soaking time during growth. The samples changed from the native n-type characteristic into the non-stoichiometric p-type characteristic with increasing soaking time. On the other hand, we found that the n-type characteristic could be preserved with enhanced ZT values in Ni-, Co-, and Zn-doped CAS samples. We obtained a maximum thermoelectric figure of merit, ZT , the value of 0.69 at 623 K in n-type CuAgSe. We have found that Zn is a promising dopant for n-type CuAgSe as it enhances the ZT value.

4.2 Experiments

We fabricated single-phase polycrystalline CuAgSe using the ‘growth from the melt’ method. High-purity Cu, Ag, and Se powders were weighed at the appropriate stoichiometry. The powders were then mixed, loaded into a quartz tube, evacuated, and sealed under the pressure of roughly 10^{-4} Torr. The ampoule was then evacuated and sealed inside another larger quartz ampoule to prevent oxidation that may occur when the inner ampoule is broken due to differences in the thermal expansion coefficients between materials and quartz and/or expansion of the material during the phase transition. Subsequently, the ampoules were loaded into a vertical electrical furnace and slowly heated up to 1323 K over 120 h. To perform the reactions, the ampoules were maintained at this temperature for different times (soaking times): 130 h (CAS-1), 165 h (CAS-2), and 266 h (CAS-3) (Table 4.1). After that, the ampoules were slowly cooled down to room temperature over 250 h. The Ni-, Co-, and Zn-doped CAS samples were grown at the same growth conditions as the sample CAS-2 by adding 2 mol% of Ni, Co, and Zn powders, which will hereafter be referred to as Ni-doped CAS-2, Co-doped CAS-2, and Zn-doped CAS-2, respectively. CAS ingots with dimensions of 13.5 mm in diameter and 25 mm in length were obtained.

The middle parts of the ingots were used for various characterization experiments. The crystal structures of the samples were investigated using X-ray diffraction (XRD) along with small-angle X-ray diffraction operating at 40 kV and 30 mA. Cu K_{α} radiation ($\lambda = 0.154056$ nm) with a scanning rate of $2^{\circ} \text{ min}^{-1}$ was used to record the patterns in the angle range of 20 to 90° . Electrical conductivity and the Seebeck coefficient were simultaneously collected from room temperature to 773 K under an Ar atmosphere to prevent oxidation and evaporation of samples. The laser flash diffusivity method (model: LFA-457, NETZSCH, Germany) was used to determine the thermal diffusivity from room temperature to 773 K. Mass density was obtained

using the Archimedes method. Heat capacity was taken from Hong's work for CuAgSe compounds [ref. 12]. Thermal conductivity was calculated by the relationship $\kappa = DC_p\rho$, where D , C_p , and ρ are the thermal diffusivity, heat capacity, and mass density, respectively.

Table 4.1 The soaking time and room temperature electrical conductivity, carrier density, and carrier mobility for all samples.

	Soaking time (h)	σ (S cm ⁻¹)	$n \cdot 10^{18}$ (cm ⁻³)	μ (cm ² V ⁻¹ s ⁻¹)
CAS-1	130	6622	7.531	5496
CAS-2	165	1623	4.575	2217
CAS-3	266	2268	4.392	3227
Ni-doped CAS-2	165	5603	7.631	4589
Co-doped CAS-2	165	5996	4.938	7589
Zn-doped CAS-2	165	5696	7.699	4624

4.3 Results and discussion

Room temperature powder XRD data of samples are shown in Fig. 4.1a. All samples exhibited nearly the same XRD patterns as JCPDS (PDF#25-1180 and PDF#10-0451) and the previous report [17]. The observations demonstrate that we obtained single-phase β -CAS. No distinct impurity peaks were found within the detection limit of the XRD instrument. As shown in Fig. 4.1b, the (110) and (111) diffraction peaks slightly shifted towards a higher angle in the presence of Ni and Co, while no significant shifts were observed with the introduction of Zn. The peak shifts for the Ni- and Co-doped CAS are due to the substitutions of smaller ionic radius Ni²⁺ (0.7 Å) and Co²⁺ (0.7 Å) ions into the larger ionic radius Cu⁺ (0.77 Å) ion sites, in agreement with [18,19]. For the Zn-doped CAS, the behavior of the peaks was attributed to the substitution of a small amount of Zn²⁺ ions for Cu⁺ ions whose ionic radii are quite similar

(0.74 Å and 0.77 Å for Zn²⁺ and Cu⁺ ions, respectively). These observations indicated that the Ni, Co, and Zn dopants were successfully doped into the CAS lattice. The determined lattice constants (a, b, and c) of all samples are presented in Table 4.2.

Table 4.2 Lattice parameters of CAS-1, CAS-2, CAS-3, and Ni-, Co-, Zn-doped CAS-2 samples.

	a (Å)	b (Å)	c (Å)
JPCDS #25-1180	4.105	4.070	6.310
CAS-1	4.102	4.056	6.335
CAS-2	4.096	4.050	6.326
CAS-3	4.103	4.056	6.337
Ni-doped CAS-2	4.091	4.044	6.319
Co-doped CAS-2	4.095	4.049	6.324
Zn-doped CAS-2	4.096	4.049	6.327

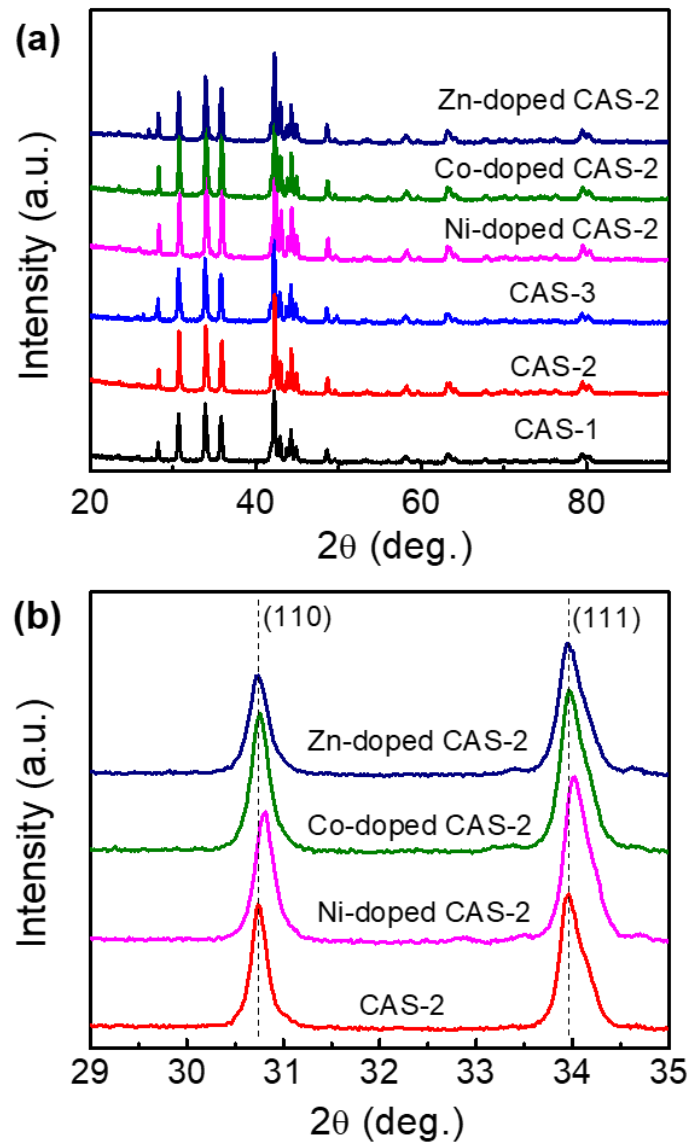


Fig. 4.1 (a) Powder XRD patterns of all CAS samples and (b) enlarged XRD patterns in the 2θ angle range from 31° to 34° for the CAS-2 sample and the Ni-, Co-, Zn-doped CAS-2 samples.

The temperature-dependent Seebeck coefficient (S), electrical conductivity (σ), and power factor (PF) of all samples are shown in Fig. 4.2. The temperature-dependent Seebeck coefficient curves of all samples showed consistent behavior with previous reports [11,12], where a sudden change in S occurred at the phase transition temperature, 470 K. As can be seen in Fig. 4.2a, Seebeck coefficients at near room temperature of all un-doped samples are negative, indicating their n-type dominant conducting mechanism. This behavior is reasonable

due to the low-temperature semimetallic β -CAS, where both electron and hole charge carriers are presented. The Seebeck coefficient of this material can be calculated as in Eq. (1);

$$S = \frac{p\mu_p S_p - n\mu_n S_n}{n\mu_n + p\mu_p} \quad (1)$$

where S is the total Seebeck coefficient, n and p are the electron and the hole concentrations, μ_p and μ_n are the hole and the electron mobility, S_p and S_n are the contributions of the hole and the electron to S . The electron's mobility is much higher than that of the hole due to its much smaller effective mass; thus, negative S is achieved.

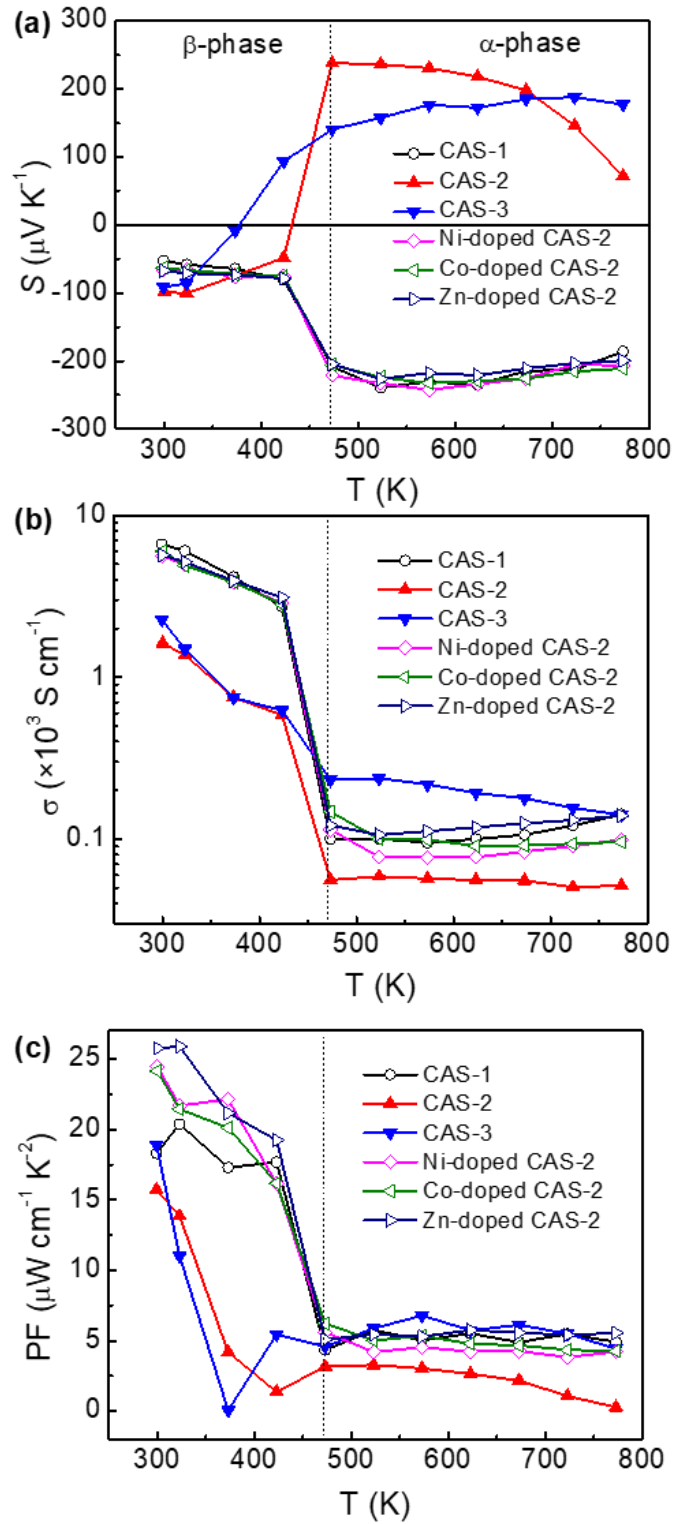


Fig. 4.2 Temperature dependence of (a) Seebeck coefficient (S), (b) electrical conductivity (σ), and (c) power factor (PF) of the CAS-1, CAS-2, CAS-3, and the Ni-, Co-, Zn-doped CAS-2 samples.

For the undoped samples, the sample CAS-1 still showed n-type conduction, while samples CAS-2 and CAS-3 transitioned from n-type to p-type conduction with increasing temperature. The sign change of S in the CAS system has been thoroughly studied using various growth conditions by Wang et al. [9] and Zuo et al. [10]. The n-type conduction CAS can be obtained in stoichiometric CAS [9] or Se and Ag deficient conditions [10]. In contrast, the p-type conduction CAS can be obtained in slightly Ag deficient, Cu deficient, or excess Se (equal to Ag and Cu deficient) conditions [9] as well as excess Se /Ag deficient conditions [10]. Except for the stoichiometric CAS growth condition, all growth conditions resulted in secondary phases such as CuSe, Ag₂Se, and Ag [9]. The behavior of S in our samples can be explained by their different growth conditions (soaking time). For the ‘growth from the melt’ method, chemical reactions between powders occurred in the heat up from room temperature. They then were further completed at high temperature (soaking temperature) depending on the soaking time. Note that Se is a volatile element that is in the vapor phase at our soaking temperature. We used the soaking time as a control parameter for these chemical reactions. Insufficient soaking time leads to poor Se growth conditions. Subsequently, some Se deficiencies were generated in the obtained sample. Our CAS-1 sample with a 130 h soaking time showed n-type conduction over the whole temperature range, in agreement with observations in [10].

Meanwhile, the reactions progressed as the soaking time increased. In this case, more Se participated in the reactions, leading to a reduction in Se deficiencies. On the other hand, the probability of forming secondary phases, such as CuSe, Ag₂Se also increased with soaking time, resulting in compound defects (Ag deficient and Cu deficient) in the sample [9,10]. The Ag and Cu deficiencies acted as acceptor dopants and provided extra holes to the crystal [9].

We recall here that all our samples were obtained in a single phase. This observation is a typical advantage of the ‘growth from the melt’ method. Unlike other methods, the ‘growth

from the melt' method provides enough time for complete chemical reactions. If some elements are excessive, they are exhibited on the top of the ingot. Therefore, no secondary phases were obtained in our samples. On the other hand, we can see from Fig. 4.2a that the transition temperature decreased with soaking time, 440 K for CAS-2 (165 h) and 373 K for CAS-3 (266 h). Similar results have been observed in [9]. Other n- to p-type transition temperatures have been reported, 445 K in non-stoichiometric CAS [10] and 400 K in CAS [12]. This behavior can be explained due to the change of hole and electron contributions to the Seebeck coefficient in the bi-polar transport regime.

The temperature-dependent S curves for the Ni-, Co-, and Zn-doped CAS- 2 samples showed negative S values in the whole temperature range, indicating the n-type conduction of these samples. As discussed above, the Ni, Co, and Zn elements were substituted into the Cu-sites in the CAS lattice. The elements (i.e., Ni, Co, and Zn) with two outermost electrons substituted into the site of Cu (with one outermost electron), resulting in extra electrons in the crystal. This substitution led to n-type conduction. Based on the above results, we conclude that the carrier type in the CAS was effectively controlled by either changing soaking time during growth or doping.

The temperature-dependent electrical conductivity behaviors of all samples are shown in Fig. 4.2b. As shown, the electrical conductivity decreases with temperature in the low-temperature β -phase, indicating the semi-metallic behavior of all samples. The electrical conductivity drops significantly above the phase transition temperature (470 K) in the high-temperature semiconducting α -phase, consistent with the trends of S . In the low-temperature β -phase, the electrical conductivities of the samples CAS-2 and CAS-3 are smaller than those of CAS-1 and Ni-, Co-, and Zn-doped CAS-2. Smaller electrical conductivities have also been reported in

non-stoichiometric CAS compared to those of stoichiometric CAS [9]. Details related to the carrier concentration and carrier mobility of all samples at 300 K are indicated in Table 4.1.

The calculated values of the power factor (PF) as a function of temperature for all samples are shown in Fig. 4.2c. The PF values of all samples in the low-temperature β -phase were much higher than that in the high-temperature α -phase due to the higher values of S and σ . Our n-type Ni-, Co-, and Zn-doped CAS-2 samples showed higher PF values than those of undoped samples over the whole temperature range. A maximum PF value of $26 \mu\text{W cm}^{-1} \text{K}^{-2}$ at 323 K was obtained for Zn-doped CAS-2.

Figure 4.3 shows the temperature dependence of thermal diffusivity (D) and thermal conductivity (κ) for all the samples. Low values of thermal diffusivity and thermal conductivity were observed. A deviation in D and κ values was observed in the low-temperature β -phase. As mentioned above, our samples exhibited semi-metallic behavior in the low-temperature β -phase, where the contribution of electrons to thermal transport is dominant. The deviations in D and κ values are due to the difference in the carrier mobility of the samples (Table 4.1). In the high-temperature α -phase, all samples showed lower values of D and κ than those in the low-temperature β -phase. This behavior was ascribed to the random distribution of the mixed Cu and Ag atoms over tetrahedral sites in the liquid-like lattice structure of the α -phase, which weakens the thermal transport of the material. The thermal conductivity of the sample CAS-1 decreased from $3.06 \text{ W m}^{-1} \text{K}^{-1}$ at 300 K to $2.61 \text{ W m}^{-1} \text{K}^{-1}$ at 423 K. After the phase transition, the thermal conductivity of the sample CAS-1 rapidly decreased with temperature to the lowest value of $0.45 \text{ W m}^{-1} \text{K}^{-1}$ at 523 K and then slightly increased to $0.83 \text{ W m}^{-1} \text{K}^{-1}$ at 773 K.

Interestingly, the thermal conductivity value of the α -phase CAS-1 was significantly lower than that of α -Cu₂Se in this temperature range ($1.0 \text{ W m}^{-1} \text{ K}^{-1}$ at $T \sim 550 \text{ K}$) [6].

The temperature-dependent behaviors of the dimensionless TE figure of merit (ZT) values for

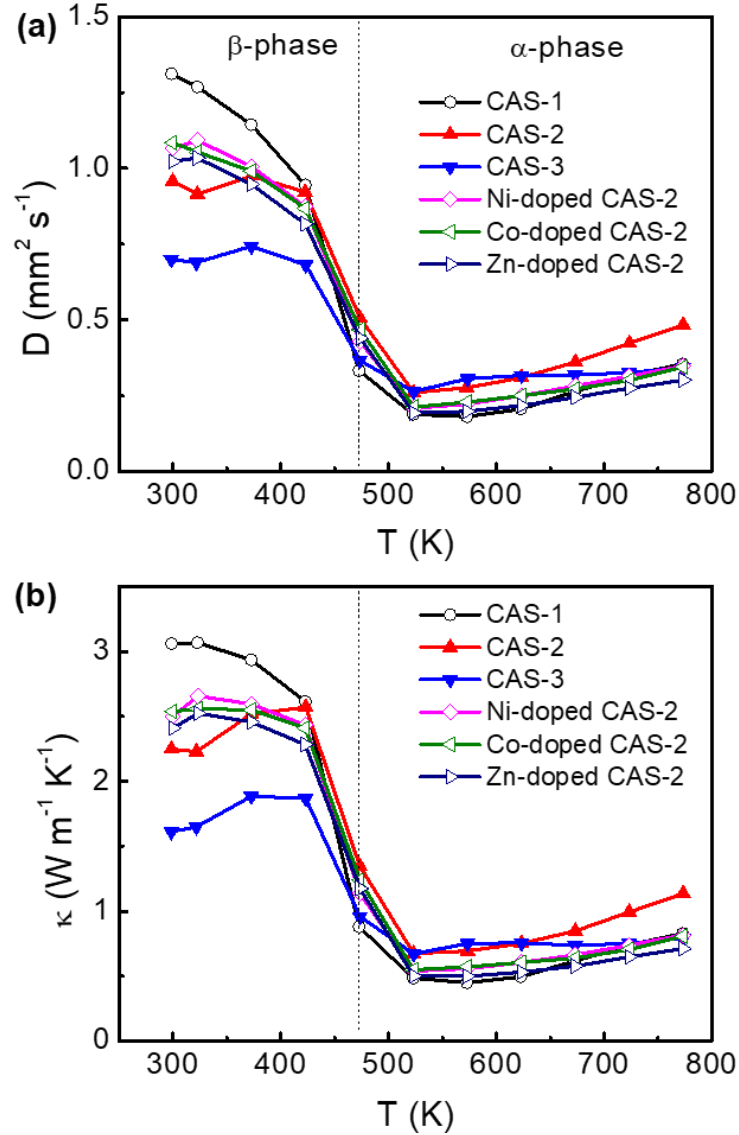


Fig. 4.3 Temperature dependence of (a) thermal diffusivity (D) and (b) thermal conductivity (κ) of the CAS-1, CAS-2, CAS-3, and the Ni-, Co-, Zn-doped CAS-2 samples.

all samples are shown in Fig. 4.4a. Much higher ZT values were observed in the high-temperature α -phase than those in the low-temperature β -phase due to the lower thermal conductivities of the α -phase. We obtained a maximum ZT value of 0.69 at 623 K in the n-type CAS-1 sample. The curves show that Zn is a promising dopant for n-type CAS with enhanced

ZT values of 0.68 at 623 K and 0.6 at 773 K, respectively. Since we did not focus on determining the doping concentration and effect of soaking time on thermoelectric properties of CAS, a study of the effects of doping concentration and soaking time is left for future work.

To enhance the conversion efficiency and working temperature range of TE devices, different n-type (p-type) TE materials with different working temperature ranges were segmented together in the n-type (p-type) leg. These devices are called segmented thermoelectric devices [20]. In order to determine suitable segmentation partners for a TE material, the thermoelectric compatibility factor of a TE material was calculated using Eq. (2) [21],

$$\alpha = \frac{\sqrt{1 + ZT} - 1}{ST} \quad (2)$$

where S is the Seebeck coefficient, and T is the absolute temperature.

Two TE materials are suitable for segmentation if their TE compatibility factor ratio is smaller than 2. Smaller TE compatibility factor ratios indicate that the materials are more suitable for segmentation. The calculated compatibility factor values as a function of temperature for all samples calculated using Eq. (2) are shown in Fig. 4.4b. As shown, the compatibility factors of all samples are nearly independent of temperature in the mid-temperature range (α -phase) with average absolute values of 1.7 V^{-1} . Thus, our samples are suitable for segmentation with other TE materials in the high-temperature range, such as $\text{Si}_{0.78}\text{Ge}_{0.22}$ and La_3Te_4 for the n-type leg and SiGe and half-Heusler alloy for the p-type leg.

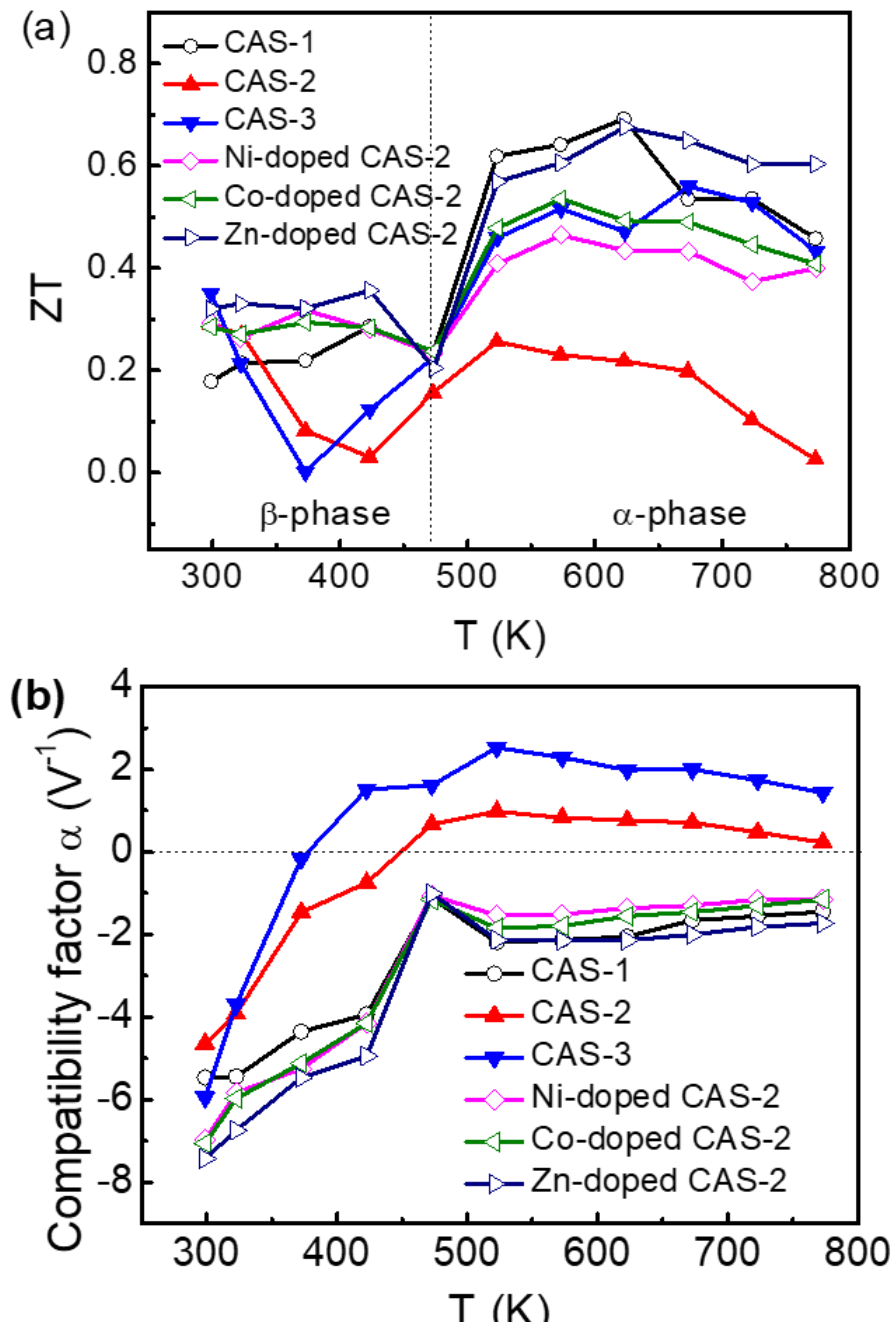


Fig. 4.4 (a) Thermoelectric figure of merit (ZT) value and (b) the thermoelectric compatibility factor as a function of temperature for the CAS-1, CAS-2, CAS-3, and the Ni-, Co-, Zn-doped CAS-2 samples.

4.4 Conclusions

In this study, single-phase undoped and Ni-, Co-, and Zn-doped CuAgSe were successfully grown using the ‘growth from the melt’ method. We experimentally showed that the carrier type in the CuAgSe semiconductor could be effectively controlled by changing soaking time or doping. The carrier type of CuAgSe was switched from the native n-type to the non-stoichiometric p-type by increasing the soaking time during growth. In contrast, when Ni, Co, and Zn were doped into the host lattice, the samples always retained their n-type behavior. We also obtained a maximum thermoelectric figure of merit (ZT) value of 0.69 at 623 K in undoped n-type CuAgSe. Zn is a promising dopant for n-type CuAgSe with a ZT value of 0.68 at 623 K.

4.5 References

- [1] G. Tan, M. Ohta, M.G. Kanatzidis, Thermoelectric power generation: From new materials to devices, *Philos. Trans. R. Soc. A Math. Phys. Eng. Sci.* 377 (2019) 20180450. <https://doi.org/10.1098/rsta.2018.0450>.
- [2] I. Petsagkourakis, K. Tybrandt, X. Crispin, I. Ohkubo, N. Satoh, T. Mori, Thermoelectric materials and applications for energy harvesting power generation, *Sci. Technol. Adv. Mater.* 19 (2018) 836–862. <https://doi.org/10.1080/14686996.2018.1530938>.
- [3] G. Slack, *New Materials and Performance Limits for Thermoelectric Cooling*, CRC Handb. Thermoelectr. (1995). <https://doi.org/10.1201/9781420049718.ch34>.
- [4] B.C. Sales, D. Mandrus, R.K. Williams, Filled skutterudite antimonides: A new class of thermoelectric materials, *Science* 272 (1996) 1325–1328. <https://doi.org/10.1126/science.272.5266.1325>.

- [5] L.M. Daniels, S.N. Savvin, M.J. Pitcher, M.S. Dyer, J.B. Claridge, S. Ling, B. Slater, F. Corà, J. Alaria, M.J. Rosseinsky, Phonon-glass electron-crystal behaviour by A site disorder in n-type thermoelectric oxides, *Energy Environ. Sci.* 10 (2017) 1917–1922. <https://doi.org/10.1039/c7ee01510k>.
- [6] H. Liu, X. Shi, F. Xu, L. Zhang, W. Zhang, L. Chen, Q. Li, C. Uher, T. Day, G. Snyder Jeffrey, Copper ion liquid-like thermoelectrics, *Nat. Mater.* 11 (2012) 422–425. <https://doi.org/10.1038/nmat3273>.
- [7] Y. He, T. Day, T. Zhang, H. Liu, X. Shi, L. Chen, G.J. Snyder, High thermoelectric performance in non-toxic earth-abundant copper sulfide, *Adv. Mater.* 26 (2014) 3974–3978. <https://doi.org/10.1002/adma.201400515>.
- [8] C. Han, Q. Sun, Z.X. Cheng, J.L. Wang, Z. Li, G.Q. Lu, S.X. Dou, Ambient scalable synthesis of surfactant-free thermoelectric CuAgSe nanoparticles with reversible metallic-n-p conductivity transition, *J. Am. Chem. Soc.* 136 (2014) 17626–17633. <https://doi.org/10.1021/ja510433j>.
- [9] X. Wang, P. Qiu, T. Zhang, D. Ren, L. Wu, X. Shi, J. Yang, L. Chen, Compound defects and thermoelectric properties in ternary CuAgSe-based materials, *J. Mater. Chem. A* 3 (2015) 13662–13670. <https://doi.org/10.1039/c5ta02721g>.
- [10] Y. Zuo, Y. Liu, Q.P. He, J.M. Song, H.L. Niu, C.J. Mao, CuAgSe nanocrystals: colloidal synthesis, characterization and their thermoelectric performance, *J. Mater. Sci.* 53 (2018) 14998–15008. <https://doi.org/10.1007/s10853-018-2676-7>.
- [11] P.F. Qiu, X.B. Wang, T.S. Zhang, X. Shi, L.D. Chen, Thermoelectric properties of Te-doped ternary CuAgSe compounds, *J. Mater. Chem. A* 3 (2015) 22454–22461. <https://doi.org/10.1039/c5ta06780d>.

- [12] A.J. Hong, L. Li, H.X. Zhu, X.H. Zhou, Q.Y. He, W.S. Liu, Z.B. Yan, J.M. Liu, Z.F. Ren, Anomalous transport and thermoelectric performances of CuAgSe compounds, *Solid State Ionics*. 261 (2014) 21–25. <https://doi.org/10.1016/j.ssi.2014.03.025>.
- [13] K. Chrissafis, N. Vouroutzis, K.M. Paraskevopoulos, N. Frangis, C. Manolikas, Phase transformation in CuAgSe: A DSC and electron diffraction examination, *J. Alloys Compd.* 385 (2004) 169–172. <https://doi.org/10.1016/j.jallcom.2004.04.119>.
- [14] S. Ishiwata, Y. Shiomi, J.S. Lee, M.S. Bahramy, T. Suzuki, M. Uchida, R. Arita, Y. Taguchi, Y. Tokura, Extremely high electron mobility in a phonon-glass semimetal, *Nat. Mater.* 12 (2013) 512–517. <https://doi.org/10.1038/nmat3621>.
- [15] J.P. Fleurial, L. Gailliard, R. Triboulet, S. Scherrer, H. Scherrer, Thermal properties of high quality single crystals of Bismuth Telluride - Part I: Experimental characterization, *J. Phys. Chem. Solids*. 49 (1988) 1237–1247. [https://doi.org/10.1016/S0022-3697\(00\)00030-5](https://doi.org/10.1016/S0022-3697(00)00030-5).
- [16] Q. Guo, D. Berthebaud, J. Ueda, S. Tanabe, A. Miyoshi, K. Maeda, T. Mori, Facile p-n control, and magnetic and thermoelectric properties of chromium selenides $\text{Cr}_{2+x}\text{Se}_3$, *J. Mater. Chem. C*. 7 (2019) 8269–8276. <https://doi.org/10.1039/c9tc01634a>.
- [17] D.M. Trops, Structure and Lattice Dynamics of Copper- and Silver-based Superionic Conducting Chalcogenides, Technischen Universität Darmstadt, 2007. <http://tuprints.ulb.tu-darmstadt.de/862/>.
- [18] P. Czajka, M. Yao, C. Opeil, Low Temperature Thermoelectric Properties of Co- and Cr- doped CuAgSe, *Cond-Mat.Mtrl-Sci.* (2016). <http://arxiv.org/abs/1610.05634>.
- [19] J.Y. Zhang, J.H. Zhu, L. You, K. Guo, Z.L. Li, W.G. Lin, J. Huang, J. Luo, Enhanced and stabilized n-type thermoelectric performance in α -CuAgSe by Ni doping, *Mater.*

Today Phys. 10 (2019). <https://doi.org/10.1016/j.mtphys.2019.100095>.

- [20] P.H. Ngan, D.V. Christensen, G.J. Snyder, L.T. Hung, S. Linderoth, N. Van Nong, N. Pryds, Towards high efficiency segmented thermoelectric unicouples, Phys. Status Solidi Appl. Mater. Sci. 211 (2014) 9–17. <https://doi.org/10.1002/pssa.201330155>.
- [21] G.J. Snyder, T.S. Ursell, Thermoelectric efficiency and compatibility, Phys. Rev. Lett. 91 (2003) 148301/1-148301/4. <https://doi.org/10.1103/PhysRevLett.91.148301>.

Chapter 5. Huge anisotropy transport properties in α -In₂Se₃ single crystal

Using the temperature gradient method, α -In₂Se₃ single crystals were successfully grown. Samples prepared using this method exhibited good crystallinity and huge anisotropic properties with regard to both their electrical resistivity and Seebeck coefficient. The in-plane vs. out-of-plane electrical resistivity anisotropic-ratio was approximately 490,000 at 20 K, 43,300 at 300 K, and 3,650 at 400 K. The in-plane and out-of-plane Seebeck coefficient values were 252 $\mu\text{V}\cdot\text{K}^{-1}$ and 397 $\mu\text{V}\cdot\text{K}^{-1}$ at 400 K, respectively. This huge anisotropy was primarily due to the anisotropic activation energy and anisotropic mobility.

5.1 Introduction

Layer-structured materials have recently attracted considerable attention due to many of their intriguing properties; for example, SnSe and Cu₂Se with high figure of merit (ZT) concerning thermoelectric applications [1–4] and semiconductor transition metal dichalcogenides MX₂ (M = Mo, W; X = S, Se) for photonic and optoelectronic devices [5]. Additionally, binary chalcogenide semiconductors of type III-VI with group VI elements S, Se, and Te have been extensively studied in the last decade, and the potential of indium selenides has revived their interest [6–9]. Due to the extraordinary and tunable electrical and thermal properties of indium selenides, materials such as In₄Se₃ have been developed as highly efficient thermoelectric materials. Single crystalline and polycrystalline In₄Se₃ materials have been reported with a high ZT of 1.53 at 425 °C [10] and 1.4 at 460 °C [11]. The physical properties of indium selenides were primarily determined by their intrinsic structural characteristics such as their composition, phase, crystal structure, and structural imperfections. From a structural point of view, indium

selenides belong to a complex system with different stoichiometric ratios such as In_4Se_3 , In_2Se_3 , InSe , In_6Se_7 , and In_3Se_4 .

Furthermore, even within a particular stoichiometric ratio, different phases and crystal structures may co-exist. In_2Se_3 can exist in the form of multiple crystalline phases such as the rhombohedral α -phase, the rhombohedral β -phase, the defect wurtzite γ -phase, and the hexagonal δ -phase [12,13]. Single crystalline α - In_2Se_3 possesses a layered structure with tetrahedral covalent bonding between the In and Se of Se-In-Se-In-Se [14], which is considered to be a spontaneous superlattice along with the out-of-plane layers [12]. Since the surface of each layer is terminated with Se atoms, layers are linked to each other by weak van der Waals interactions. However, the interlayer van der Waals interactions are much weaker than in-plane covalent bonds, leading to highly anisotropic structural, electrical, optical, and mechanical properties [15–17]. Recently, many defects in In_2Se_3 crystals [18] and their effect on anisotropic charge transport properties have been reported. The anisotropic conductivity in Mn, Cd, I, and Cu-doped In_2Se_3 has also been observed by Kaminskii *et al.* [17–19] and Zaslokin *et al.* [16]. The electrical conductivity along layers is much more excellent than across layers. The anisotropy in temperature-dependent conductivity has been used to evaluate the energy barrier height between the layers in the crystal. In layer-structured In_2Se_3 nanowires, Peng *et al.* [14] observed a large anisotropy of electrical conductivity up to $10^3 - 10^6$ at room temperature. Nevertheless, the anisotropic ratio concerning the electrical resistivity of α - In_2Se_3 bulk single crystals was not high, and the anisotropic Seebeck coefficient has not been thoroughly investigated.

In_2Se_3 has been studied by many different methods such as the Bridgman method, MBE, and sputtering, etc. [17,20,21]. The temperature gradient method is well known as a simple method used to grow binary compounds. In this study, the growth of In_2Se_3 single crystals by the

temperature gradient method is presented. The crystal structure, optical properties, and anisotropic transport properties of single-crystalline α -In₂Se₃ were experimentally investigated. A strong electrical resistivity and Seebeck coefficient dependence concerning crystallographic directions were concluded to be observed.

5.2 Experiments

α -In₂Se₃ single crystals were grown by the temperature gradient method using a mixture of In (powder, 99.99%, Alfa Aesar) and Se (powder, 99.5%, Alfa Aesar). The powders were first weighed and loaded into thick-walled quartz ampules. The ampules were then evacuated and sealed under the pressure of 10^{-3} Torr. Next, they were placed into a vertical electrical furnace and slowly heated to form a single-phase In₂Se₃. The temperature was raised to 1248 K, followed by a 16-hour soak. For single crystal growth, the temperature was slowly cooled by 1 K/h to a point below the melting temperature (1153 K for In₂Se₃) and after that by 30 K/h to room temperature. Single crystals that were about 35 to 37 mm in length and 13 mm in diameter were obtained.

The crystal structure was investigated via X-ray diffraction (XRD) using Cu K_{α} radiation ($\lambda = 0.1540598$ nm) with a scan rate of 2°min^{-1} to record patterns between the angle range of $10 - 120^{\circ}$. Layered structures in the α -In₂Se₃ single crystals were observed via field emission scanning electron microscopy (FESEM) at 15 kV. The composition was determined using energy dispersive X-Ray spectroscopy (EDS). A 473 nm Ar-ion laser was used for photoluminescence studies at room temperature. Raman spectra were obtained at room temperature with a DXR Raman microscope (Thermo Scientific, USA), which was equipped with a 532 nm laser. The laser power was 5 mW to obtain a good signal to noise ratio. Both electrical conductivity and Seebeck coefficient measurements were obtained using a physical property measurement system (PPMS) within the temperature range of 20 to 400 K.

5.3 Results and discussion

The XRD pattern of a cleaved In_2Se_3 single crystal can be seen in Fig. 5.1. Peak assignments for $\alpha\text{-In}_2\text{Se}_3$ were determined with the help of powder diffraction standards (JCPDS) with file number 34-0455 (Rhombohedral, $\alpha\text{-In}_2\text{Se}_3$). All peaks were slightly shifted toward higher angles. The main $(00l)$ diffraction peaks ($l = 6, 9, 12, 15, 18\dots$) indicated single-crystal structures of the grown sample. Using powder XRD measurements of powdered $\alpha\text{-In}_2\text{Se}_3$ (Fig. S5.1, supplementary), the lattice parameters of bulk $\alpha\text{-In}_2\text{Se}_3$ single crystals were calculated as $a = 4.032 \text{ \AA}$ and $c = 28.705 \text{ \AA}$. On the other hand, we could not see any secondary phases in

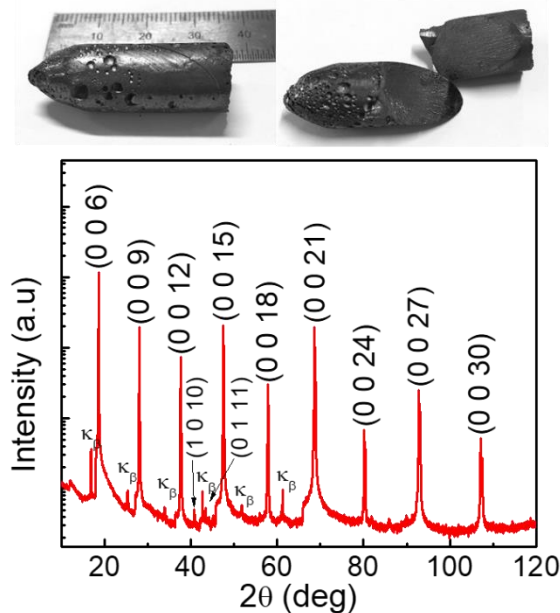


Fig. 5.1 XRD pattern of single-crystalline $\alpha\text{-In}_2\text{Se}_3$. The photo is of $\alpha\text{-In}_2\text{Se}_3$ single crystals.

our sample from the PXRD data.

The layered structures of $\alpha\text{-In}_2\text{Se}_3$ were investigated via field-emission scanning electron microscopy, as depicted in Fig. 5.2. The FE-SEM image showed an ordered layer array of $\alpha\text{-In}_2\text{Se}_3$. X-ray EDS acquired from the surface exhibited strong In and Se peaks; the atomic ratio

of In to Se was close to 2:3 as expected. We concluded that we grew rhombohedral α - In_2Se_3 single crystals using the temperature gradient method.

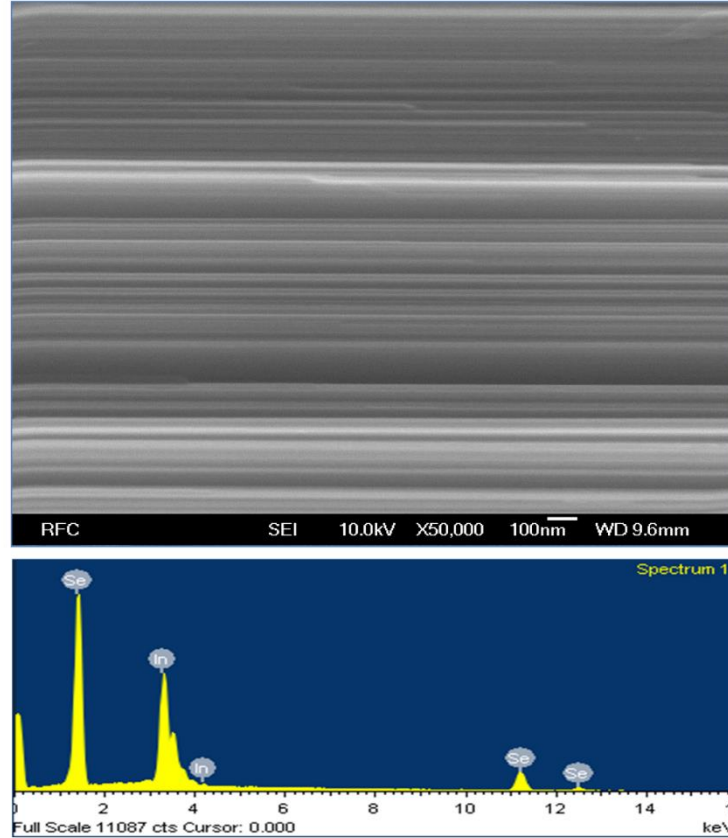


Fig. 5.2 FE-SEM image of single-crystalline α - In_2Se_3 .

The room temperature photoluminescence spectra of single-crystalline α - In_2Se_3 were obtained as seen in Fig. 5.3. Interestingly, the PL signal in single-crystalline α - In_2Se_3 was located at around 1.39 eV. The bandgap of single-crystalline α - In_2Se_3 with excess indium was reported to be 1.354 eV at 5 K by Ref.[22], which was smaller than that of our single crystal by 0.036 eV. Raman spectroscopy of laminar chalcogenide α - In_2Se_3 can be seen in Fig. 5.4. A peak appearing at the lowest frequency (107 cm^{-1}) assigned to the A^1_{1g} (LO+TO) mode was attributed to shear vibrations of one layer against others along the c-axis. The A^2_{1g} (TO) and A^2_{1g} (LO) modes observed at 186 and 196 cm^{-1} were assigned to intra-layer vibrations. This

pattern indicated the formation of single-crystalline α -In₂Se₃ structures that have been previously reported in the literature [23,24].

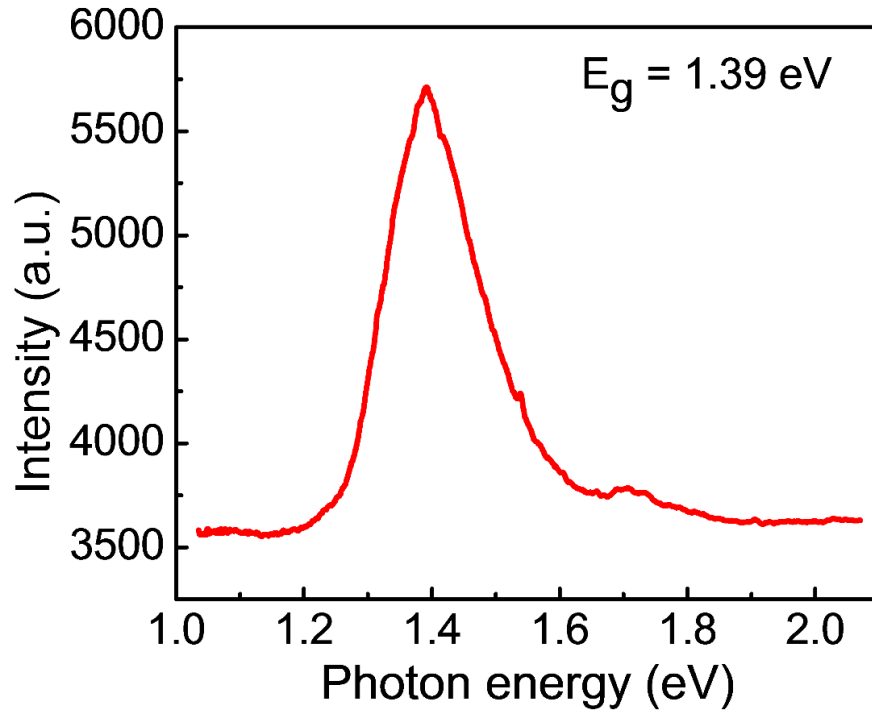


Fig. 5.3 Room temperature photoluminescence of single-crystalline α -In₂Se₃.

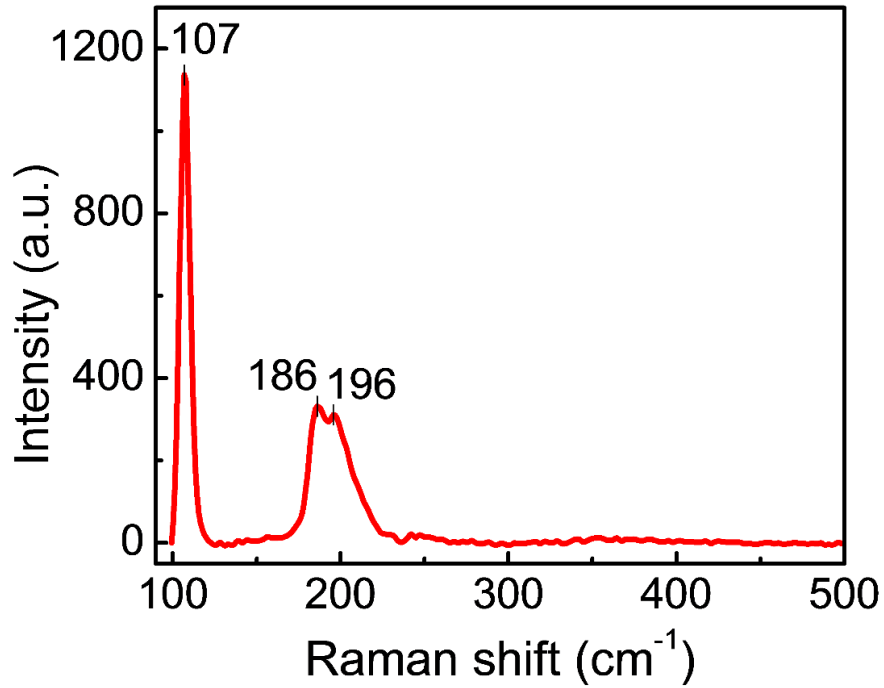


Fig. 5.4 Raman shift of single-crystalline α - In_2Se_3 .

The electrical resistivity was examined in two crystallographic directions to investigate the anisotropy of electrical resistivity in single-crystalline α - In_2Se_3 . Figure 5.5a illustrates the temperature dependence of the in-plane (ρ_a) and out-of-plane (ρ_c) electrical resistivity of single-crystalline α - In_2Se_3 . The anisotropic ratio concerning electrical resistivity was $\rho_c/\rho_a \sim 3,650$ at 400 K and increased with a reduction in temperature to about 43,300 at 300 K and 490,000 at 20 K. This huge anisotropy in the electrical resistivity of α - In_2Se_3 was greater than that of other layered structure materials. For example, the anisotropy ratio was $\rho_c/\rho_a \sim 12.80$ for SnS_2 and 6.92 for SnSe_2 at 300 K, as reported in Ref. [25]. Additionally, the anisotropy ratio of single-

crystalline Bi_2Te_3 at room temperature was around 4, smaller than that of single-crystalline $\alpha\text{-In}_2\text{Se}_3$ [26].

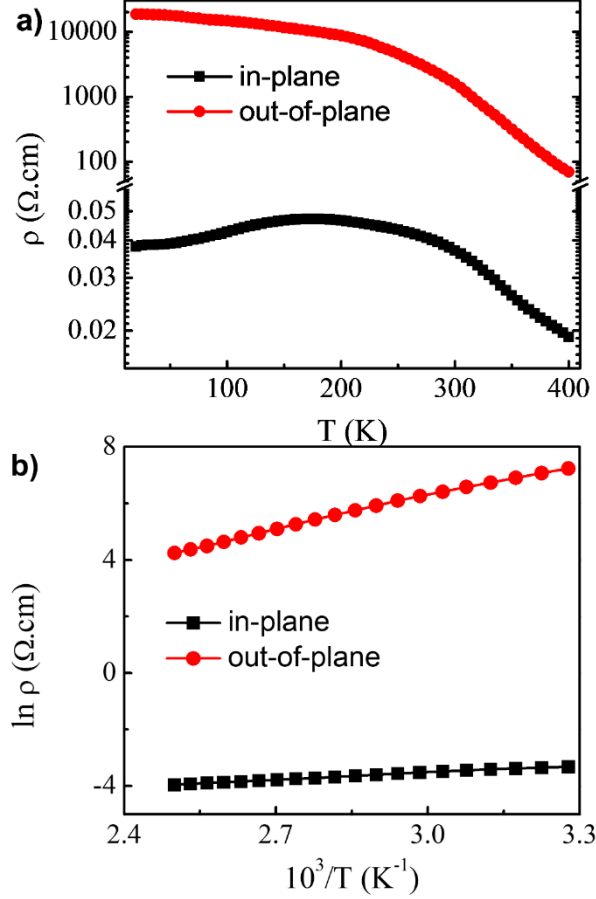


Fig. 5.5 (a) Temperature dependence of the in-plane and out-of-plane electrical resistivity of single-crystalline $\alpha\text{-In}_2\text{Se}_3$. (b) Arrhenius plot of the in-plane and out-of-plane electrical resistivity values of single-crystalline $\alpha\text{-In}_2\text{Se}_3$ from 300 to 400 K.

Both ρ_a and ρ_c exhibited a thermally activated temperature dependence of equation (1):

$$\rho = \rho_0 \exp(\Delta E_g/k_B T) \quad (1)$$

where k_B is the Boltzmann constant, ρ_0 is the temperature-independent factor, and ΔE_g is the activation energy. Figure 5.5b shows an Arrhenius plot of the in-plane and out-of-plane electrical resistivity of single-crystalline $\alpha\text{-In}_2\text{Se}_3$ from 300 to 400 K. The in-plane activation energy was calculated to be about 0.076 eV, which was different from that of the out-of-plane

direction, 0.338 eV. The observed activation energy strongly depended on the direction of the sample.

It was well known that within layered α -In₂Se₃, interlayer van der Waals interactions were much weaker than intralayer covalent bonds, resulting in a highly anisotropic electronic band structure. Additionally, the observed activation energy dependence concerning sample direction could be explained using the anisotropic electronic band structure. However, a detailed analysis of the electronic band structure properties of α -In₂Se₃ from a theoretical point of view has not yet been completed. Li *et al.* [27] calculated the electronic band structure of α -In₂Se₃ with a rhombohedral primitive cell. The α -In₂Se₃ phase was observed in an n-type semiconductor with highly dispersive conduction bands (small effective electron mass) and flat valence bands. The effective electron mass along the in-plane direction was slightly smaller than that along the out-of-plane direction. The anisotropic electrical resistivity ratio between the two directions was shown to be not far from our experimental results. Our experimental anisotropic electrical resistivity yielded the opposite side with a huge ratio. It was therefore concluded that other factors should be carefully considered to match the experimental results of the theoretical calculations for electronic band structures. Furthermore, the presence of weak van der Waals coupling between layers promotes empty indium sites. On the other hand, defects of α -In₂Se₃ were not only cationic vacancies (V_{In}) but also other defects such as interstitial In atoms (In_i) and anionic Se vacancies (V_{Se}) [18]. Thus, anisotropic electrical resistivity in the layered crystal was due to specific energy bands and structural defects in the electrical transport process, as reported in Ref. [19]. Therefore, it was believed that the high anisotropic electrical resistivity was probably due to the bonding of the layered crystal structure and the influence of defects located between layers and within the α -In₂Se₃ single crystals.

Seebeck coefficients (S) were also measured along with two crystallographic directions. A temperature gradient was applied to the sample while the voltage was measured in the same direction. Figure 5.6a shows the in-plane S_a and out-of-plane S_c . We observed that the values of S_c exceeded the values of S_a , which reflected the anisotropic nature in single-crystalline α - In_2Se_3 ; for example, $S_a = -252 \mu\text{V}.\text{K}^{-1}$, while $S_c = -397 \mu\text{V}.\text{K}^{-1}$ at 400 K. The sign of both the S_a and S_c coefficients were negative throughout the temperature range, indicating n-type dominant conduction. The magnitude of the Seebeck coefficients increased with temperatures between the range of 20 to 400 K. Interestingly, the Seebeck coefficients increased with temperature while the electrical resistivities decreased; thus, the power factors increased with temperature, as seen in Fig. 5.6b.

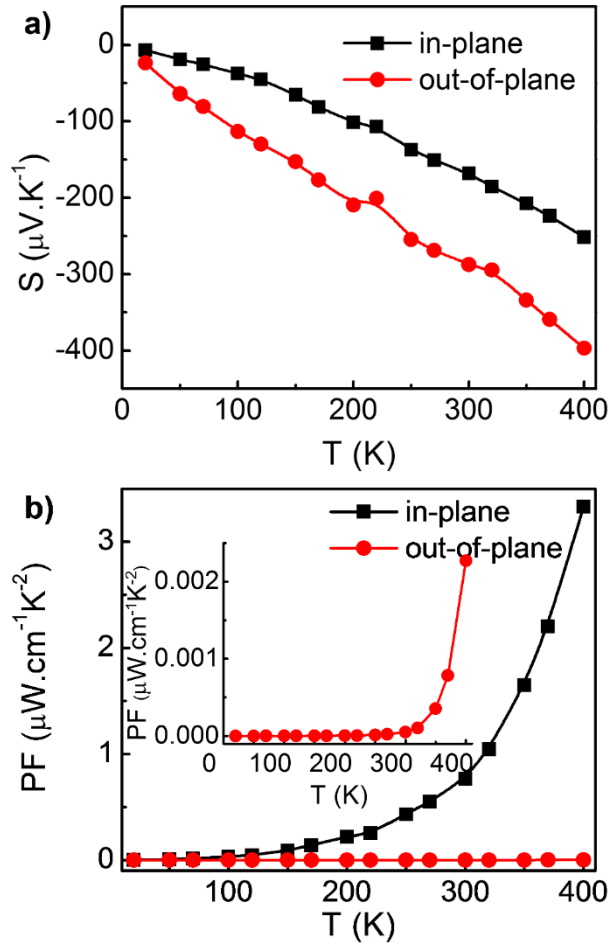


Fig. 5.6 Temperature dependence of the in-plane and out-of-plane (a) Seebeck coefficient and (b) power factor.

Figure 5.7a shows V_H/I vs. the magnetic field (H) for single-crystalline α - In_2Se_3 at selected temperatures. The Hall resistance shows that α - In_2Se_3 exhibited a negative slope in the V_H/I versus H curve, indicating that electrons were major carriers for conductivity. The carrier concentrations of the samples were calculated using equation (2), and the slope of V_H/I vs. H , as shown in Fig. 5.7b.

$$V_H/I = (1/net)H \quad (2)$$

Here, V_H is the Hall voltage, I is current, n is the number of carriers, e is the electrical charge, H is the magnetic field, and t is the thickness of the sample. The electron carrier concentration of the sample increased with temperature, as illustrated in Fig. 7b, which was typical of

semiconducting behavior; for example, 5.5×10^{17} and $8.6 \times 10^{17} \text{ cm}^{-3}$ at 300 and 400 K, respectively. Simultaneous measurements of the electrical conductivity and Hall effect permitted us to investigate the influence of carrier mobility as presented in Fig 5.7c. The electron mobility along the in-plane direction was much higher than that along the out-of-plane direction. Additionally, the mobility along the out-of-plane was enhanced more dramatically above 300 K.

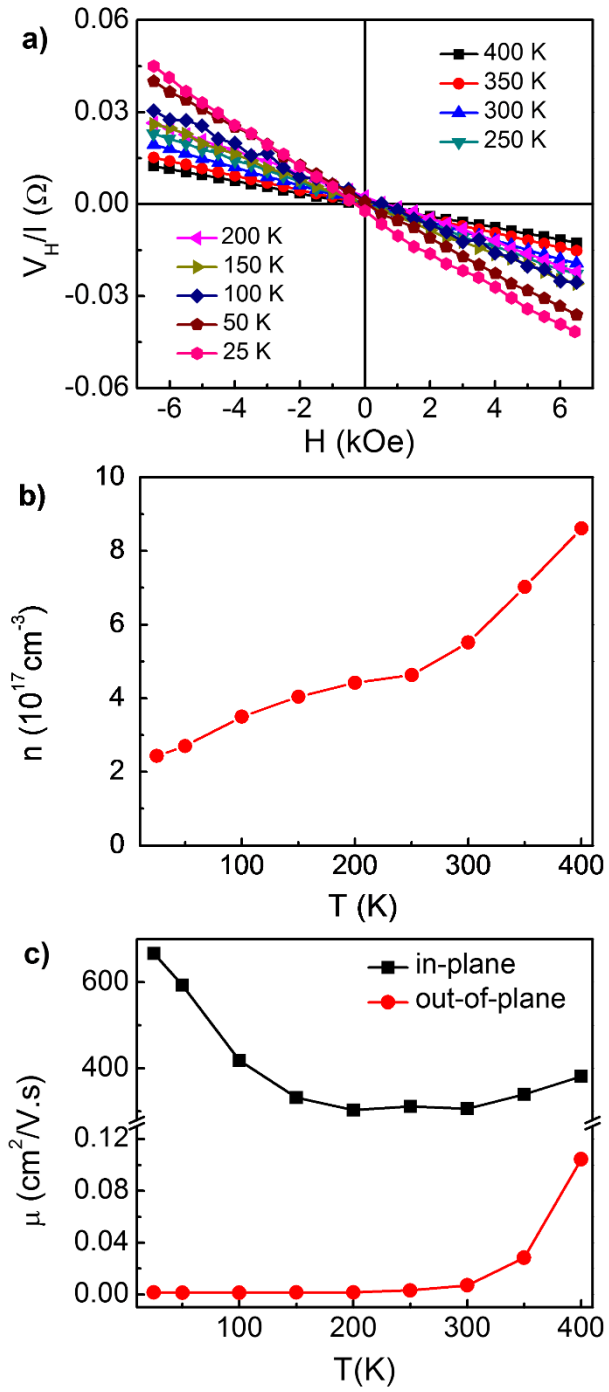


Fig. 5. 7 (a) V_H/I vs. magnetic field curves for single-crystalline α - In_2Se_3 at various temperatures. (b) The temperature-dependent carrier concentration of α - In_2Se_3 single crystals. (c) Temperature dependence of the in-plane and out-of-plane electrical mobilities.

5.4 Conclusion

In this study, α - In_2Se_3 single crystals were successfully synthesized. We observed large anisotropic transport properties in the α - In_2Se_3 single crystals. The in-plane vs. out-of-plane anisotropic-ratio in electrical resistivity was approximately 490,000 at 20 K, 43,300 at 300 K, and 3,650 at 400 K. This huge anisotropy in transport phenomena could be attributed to the anisotropic activation energy and huge anisotropic mobility in both directions.

5.5 Supplementary figures

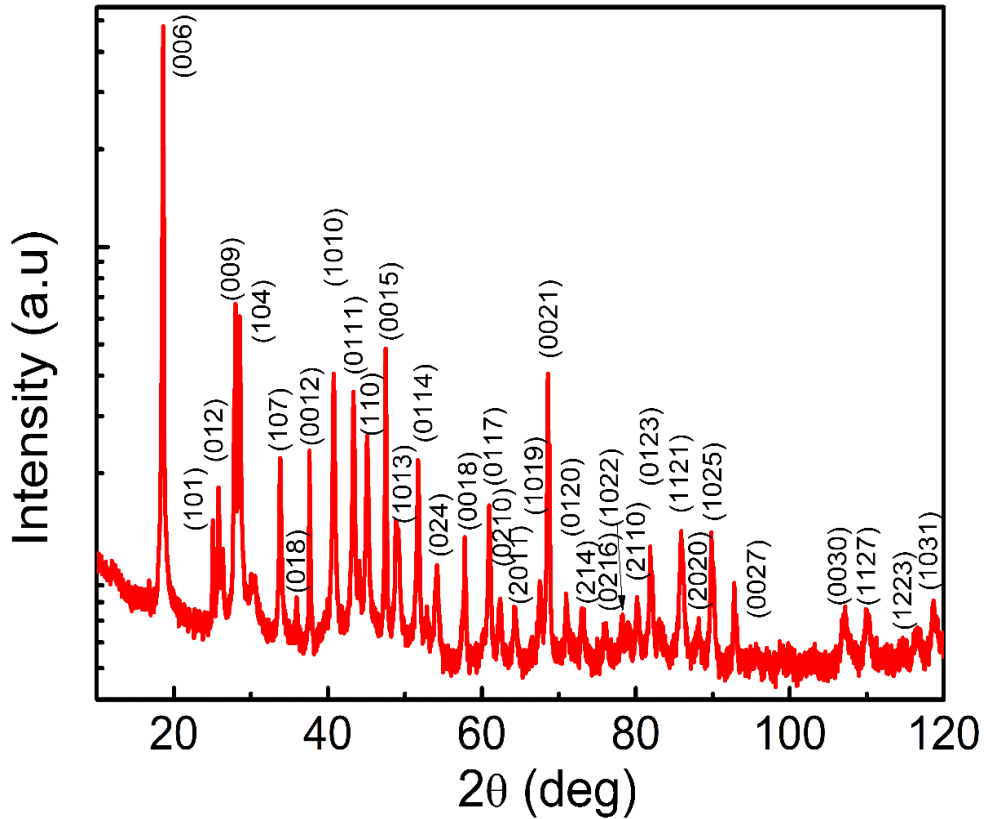


Fig. S5.1 Powder XRD of powdered α - In_2Se_3

5.6 References

- [1] A.T. Duong, V.Q. Nguyen, G. Duvjir, V.T. Duong, S. Kwon, J.Y. Song, J.K. Lee, J.E. Lee, S. Park, T. Min, J. Lee, J. Kim, S. Cho, Achieving $ZT=2.2$ with Bi-doped n-type SnSe single crystals, *Nat. Commun.* 7 (2016) 1–6.

<https://doi.org/10.1038/ncomms13713>.

- [2] L.D. Zhao, S.H. Lo, Y. Zhang, H. Sun, G. Tan, C. Uher, C. Wolverton, V.P. Dravid, M.G. Kanatzidis, Ultralow thermal conductivity and high thermoelectric figure of merit in SnSe crystals, *Nature*. 508 (2014) 373–377. <https://doi.org/10.1038/nature13184>.
- [3] B. Zhong, Y. Zhang, W. Li, Z. Chen, J. Cui, Y. Xie, Q. Hao, Q. He, High superionic conduction arising from aligned large lamellae and large figure of merit in bulk $\text{Cu}_{1.94}\text{Al}_{0.02}\text{Se}$, *Appl. Phys. Lett.* 105 (2014) 0–4. <https://doi.org/10.1063/1.4896520>.
- [4] H. Liu, X. Shi, F. Xu, L. Zhang, W. Zhang, L. Chen, Q. Li, C. Uher, T. Day, G. Snyder Jeffrey, Copper ion liquid-like thermoelectrics, *Nat. Mater.* 11 (2012) 422–425. <https://doi.org/10.1038/nmat3273>.
- [5] J.Y. Lee, J.H. Shin, G.H. Lee, C.H. Lee, Two-dimensional semiconductor optoelectronics based on van der Waals heterostructures, *Nanomaterials*. 6 (2016) 40–43. <https://doi.org/10.3390/nano6110193>.
- [6] J.R. Szczech, J.M. Higgins, S. Jin, Enhancement of the thermoelectric properties in nanoscale and nanostructured materials, *J. Mater. Chem.* 21 (2011) 4037–4055. <https://doi.org/10.1039/c0jm02755c>.
- [7] J.R. Sootsman, D.Y. Chung, M.G. Kanatzidis, New and old concepts in thermoelectric materials, *Angew. Chemie - Int. Ed.* 48 (2009) 8616–8639. <https://doi.org/10.1002/anie.200900598>.
- [8] Y. Lan, A.J. Minnich, G. Chen, Z. Ren, Enhancement of thermoelectric figure-of-merit by a bulk nanostructuring approach, *Adv. Funct. Mater.* 20 (2010) 357–376. <https://doi.org/10.1002/adfm.200901512>.
- [9] C.J. Vineis, A. Shakouri, A. Majumdar, M.G. Kanatzidis, Nanostructured

- thermoelectrics: Big efficiency gains from small features, *Adv. Mater.* 22 (2010) 3970–3980. <https://doi.org/10.1002/adma.201000839>.
- [10] J.S. Rhyee, K. Ahn, K.H. Lee, H.S. Ji, J.H. Shim, Enhancement of the thermoelectric figure-of-merit in a wide temperature range in $\text{In}_4\text{Se}_{3-x}\text{Cl}_{0.03}$ bulk crystals, *Adv. Mater.* 23 (2011) 2191–2194. <https://doi.org/10.1002/adma.201004739>.
- [11] Z.S. Lin, L. Chen, L.M. Wang, J.T. Zhao, L.M. Wu, A promising mid-temperature thermoelectric material candidate: Pb/Sn-codoped $\text{In}_4\text{Pb}_x\text{Sn}_y\text{Se}_3$, *Adv. Mater.* 25 (2013) 4800–4806. <https://doi.org/10.1002/adma.201302038>.
- [12] N.D. Raranskii, V.N. Balazyuk, Z.D. Kovalyuk, N.I. Mel’Nik, V.B. Gevik, Crystal growth and elastic properties of In_2Se_3 , *Inorg. Mater.* 47 (2011) 1174–1177. <https://doi.org/10.1134/S0020168511110203>.
- [13] K. Osamura, Y. Murakami, Y. Tomiie, Crystal structure of α - and β -Indium Selenide, In_2Se_3 , *J. Phys. Society Japan.* 21 (1966) 1848.
- [14] H. Peng, C. Xie, D.T. Schoen, Y. Cui, Large anisotropy of electrical properties in layer-structured In_2Se_3 nanowires, *Nano Lett.* 8 (2008) 1511–1516. <https://doi.org/10.1021/nl080524d>.
- [15] M. Ishikawa, T. Nakayama, Stacking and Optical Properties of Layered In_2Se_3 , *Jpn J. Appl. Phys.* 37 (1998) 1122–1124.
- [16] A. V. Zaslonskiy, Z.D. Kovalyuk, I. V. Mintyanskiy, Electrical properties of In_2Se_3 layered crystals doped with cadmium, iodine, or copper, *Inorg. Mater.* 43 (2007) 1271–1274. <https://doi.org/10.1134/S0020168507120011>.
- [17] V.M. Kaminskii, Z.D. Kovalyuk, A. V. Zaslonskiy, V.I. Ivanov, Electrical properties of

$\text{In}_2\text{Se}_3\langle\text{Mn}\rangle$ and $\text{InSe}\langle\text{Mn}\rangle$ crystals, *Inorg. Mater.* 48 (2012) 103–105.
<https://doi.org/10.1134/S0020168512020112>.

- [18] J. Cui, L. Wang, Z. Du, P. Ying, Y. Deng, High thermoelectric performance of a defect in $\alpha\text{-In}_2\text{Se}_3$ -based solid solution upon substitution of Zn for In, *J. Mater. Chem. C* 3 (2015) 9069–9075. <https://doi.org/10.1039/c5tc01977j>.
- [19] V.M. Kaminskii, Z.D. Kovalyuk, A. V. Zaslonskiy, V.I. Ivanov, Structure and electrical properties of $\text{In}_2\text{Se}_3\langle\text{Mn}\rangle$ layered crystals, *Semicond. Physics, Quantum Electron. Optoelectron.* 12 (2009) 290–293. <https://doi.org/10.15407/spqeo12.03.290>.
- [20] T. Kato, Y. Utsugi, T. Ohara, T. Muranaka, Y. Nabetani, T. Matsumoto, Dependence of In_2Se_3 crystal structures grown on GaAs (001) substrates on growth temperature and VI/III ratio, *J. Cryst. Growth.* 311 (2009) 847–850. <https://doi.org/10.1016/j.jcrysgro.2008.09.128>.
- [21] Y. Yan, S. Li, Z. Yu, L. Liu, C. Yan, Y. Zhang, Y. Zhao, Influence of indium concentration on the structural and optoelectronic properties of indium selenide thin films, *Opt. Mater. (Amst.)* 38 (2014) 217–222. <https://doi.org/10.1016/j.optmat.2014.10.033>.
- [22] N.O. Kim, H.G. Kim, H.J. Lim, C. Il Lee, M.S. Jin, C.S. Yoon, W.T. Kim, Electrical and optical properties of $\alpha\text{-In}_2\text{Se}_3$ single crystals with an indium excess, *J. Korean Phys. Soc.* 38 (2001) 405–408.
- [23] J. Zhou, Q. Zeng, D. Lv, L. Sun, L. Niu, W. Fu, F. Liu, Z. Shen, C. Jin, Z. Liu, Controlled Synthesis of High-Quality Monolayered $\alpha\text{-In}_2\text{Se}_3$ via Physical Vapor Deposition, *Nano Lett.* 15 (2015) 6400–6405. <https://doi.org/10.1021/acs.nanolett.5b01590>.

- [24] R. Lewandowska, R. Bacewicz, J. Filipowicz, W. Paszkowicz, Raman scattering in α - In_2Se_3 crystals, *Mater. Res. Bull.* 36 (2001) 2577–2583.
- [25] B.Z. Sun, Z. Ma, C. He, K. Wu, Anisotropic thermoelectric properties of layered compounds in SnX_2 ($X = \text{S}, \text{Se}$): A promising thermoelectric material, *Phys. Chem. Chem. Phys.* 17 (2015) 29844–29853. <https://doi.org/10.1039/c5cp03700j>.
- [26] M.M. Nassary, H.T. Shaban, M.S. El-Sadek, Semiconductor parameters of Bi_2Te_3 single crystals, *J. Optoelectron. Adv. Mater.* 11 (2009) 180–185.
- [27] W. Li, F.P. Sabino, F. Crasto De Lima, T. Wang, R.H. Miwa, A. Janotti, Large disparity between optical and fundamental band gaps in layered In_2Se_3 , *Phys. Rev. B.* 94 (2018) 165134. <https://doi.org/10.1103/PhysRevB.98.165134>.

Chapter 6. Growth & Un-stability characteristic of β -InSe single crystal

(TO BE CONTINUED)

We report on the un-stability characteristic of InSe single crystal, grown by using a temperature gradient technique. The sample was crystallized in the hexagonal β -InSe phase with a layered structure, confirmed by X-ray diffraction, Raman scattering, and scanning electron microscopy studies. Intriguingly, we observed a discontinuous decrease in electrical resistivity with the temperature. Temperature-dependent structural and specific heat capacity studies indicated that no phase transition occurred. Using a scanning tunneling microscopy study, we have found that the number and size of defects in the β -InSe single-crystal increased with temperature. On the other hand, the cleaved surface and defects were changed under an applied bias voltage. This un-stability characteristic of β -InSe is attributed to the weak In-Se bond in the quadruple slab of β -InSe. The un-stability characteristic leads to a discontinuity variation of electrical resistivity of InSe with temperature. Our work provided extremely important information for realizing InSe in applications such as in devices using an electric field, FET. The origination of the un-stability characteristic will be discussed since this work is not finished yet.

6.1 Introduction

Two dimensional (2D) materials offer fascinating opportunities in the field of microelectronic and optoelectronic devices due to their novel properties such as finite bandgap and flexibility. On the other hand, for some indirect bandgap 2D semiconductors, it is possible to convert to a direct bandgap by reducing thickness, enabling them for optoelectronics and photodetection applications. After discovering graphene, various 2D materials have been experimentally and

theoretically explored, including transition metal dichalcogenides (TMDCs), hexagonal boron nitride (hBN), black phosphorus, and III-VI semiconductors, etc. The TMDCs, such as MoS₂ and WSe₂, are undesirable material for high mobility devices because of a heavy electron effective mass ($m^* = 0.45m_0$)[1] and a low room temperature mobility of $200 \text{ cm}^2 \text{ V}^{-1} \text{ s}^{-1}$ for monolayer TMDCs[2]. Black phosphorus shows higher carrier mobility at room temperature, about $1995 \text{ cm}^2 \text{ V}^{-1} \text{ s}^{-1}$ for a few-layer[3], but it is less stable than graphene and MoS₂ due to its rapid oxidation in ambient conditions. For applications, indirect to direct bandgap conversions have been successfully realized in monolayer and few layers of some TMDCs such as MoS₂, WS₂, MoSe₂, and WSe₂[4,5].

Among these 2D materials, InSe is a new promising platform for developing high-speed electronic devices due to its small effective mass ($m^* = 0.14m_0$), high electron mobility (exceeds $10^3 \text{ cm}^2 \text{ V}^{-1} \text{ s}^{-1}$ and $10^4 \text{ cm}^2 \text{ V}^{-1} \text{ s}^{-1}$ at room and liquid-helium temperatures, respectively)[6], flexibility, and ambient stability[7]. InSe exhibits a layered structure, where each layer contains sublayers, closely packed with two In and two Se in a stacking sequence Se-In-In-Se, whereas the bonding between two adjacent layers is the weak Van der Waals type[8]. Therefore, InSe usually presents a strong anisotropy characteristic. On the other hand, InSe can crystallize in hexagonal (β - and ϵ -InSe) or rhombohedral (γ -InSe) layered crystal structures that differ stacking of the quadruple-layers[9]. The crystal structure of β - and ϵ -InSe shows ABAB stacking, while the ABCABC stacking exists in the rhombohedral γ -InSe structure. The hexagonal β - and ϵ -InSe phases show similar lattice parameters of $a = 4.005 \text{ \AA}$ and $c = 16.640 \text{ \AA}$. They can be distinguished by using the Raman technique[9,10]. The rhombohedral γ -InSe belongs to the R3m space group with lattice parameters of $a = 4.005 \text{ \AA}$ and $c = 24.960 \text{ \AA}$ [11]. Furthermore, the β and γ -InSe phases exhibit direct bandgap ($E_g = 1.25$ and 1.29 eV), which is of vital interest for InSe-based optoelectronic devices[12–15]. Recently, InSe has been reported with outstanding efficiency optoelectronic devices[16,17]. InSe-based

photodetectors have been reported as the most efficient among 2D materials[18]. So far, β -InSe has been known as the most stable phase of InSe. The ambient stability of InSe-based FETs has been demonstrated. The FET with uncapped InSe active channel exhibits a p-type transport due to environmental doping (H_2O) at defects sites, while FET with hBN capped InSe active channel exhibit ambipolar transport[7]. However, more insightful investigations on this issue under different applied extreme conditions are needed to be revealed. For the growth of InSe single crystal, molecular beam epitaxy (MBE)[19], flash evaporation[20], chemical vapor deposition[21], Czochralski[22], and Bridgman-Stockbarger[23] techniques, etc., have been mostly used.

In this work, we provide more insight investigations from macroscopic to microscopic scale on InSe single-crystal stability, grown by using a temperature gradient technique. The temperature gradient technique provided excellent InSe ingot, which crystallized in the hexagonal β -InSe phase. Scanning tunneling microscopy (STM) studies demonstrated an un-stability characteristic of the β -InSe single crystal where defects and surface of InSe can be modified under an applied bias voltage and a change of temperature. This un-stability characteristic of β -InSe led to a discontinuity in its transport property. This information is extremely important for InSe-based devices, concerning the electric field or temperature change such as FETs, thermoelectric modules, etc., as well as for understanding the intrinsic properties of InSe.

6.2 Experimental

InSe single crystals were grown by the temperature gradient technique using a mixture of In (powder, 99.99%, Alfa Aesar) and Se (powder, 99.5%, Alfa Aesar) raw materials without any further treatment. The raw powders were weighed in an appropriate stoichiometry. After that, the materials were loaded into a thick-walled quartz ampoule, evacuated, and sealed under the pressure of $\sim 10^{-4}$ Torr. The ampoule was then loaded into another bigger quartz ampoule,

evacuated, and sealed to prevent the sample from oxidation when the inner ampoule was broken due to different thermal expansion coefficients between materials and quartz. Subsequently, the ampoules were placed in a vertical electrical furnace. The furnace was slowly heated up to 1023 K in 100 h, soaked at this temperature for 16 h to ensure a complete reaction. The furnace was then slowly cooled down from 1023 to 723 K at a rate of 1 K h⁻¹. Note that the melting point of InSe is 873 K. This slowly cool down across the compound's melting point process ensures a high-quality single crystal growth in an equilibrium state. Finally, it was cooled down to room temperature at a rate of 20 K h⁻¹. Excellence InSe ingot was obtained with about 25 mm in length and 13.5 mm in diameter.

The crystal structure of the sample at some selected temperatures was investigated by using the X-ray diffraction (XRD) taken on a cleaved plane along with small-angle X-ray diffraction operating at 40 kV and 30 mA. Cu K_α radiation ($\lambda = 0.154060$ nm) with a scanning rate of 2° min⁻¹ was used to record the patterns in the angle range of 10 to 80°. For phase determination, powder XRD of the ground sample was taken at room temperature. Field emission scanning electron microscopy (FE-SEM) at 10 kV was used to investigate the sample's microstructure. The actual composition was determined by the Energy Dispersive X-Ray Spectroscopy (EDS). Room temperature Raman spectroscopy was used for better phase verification using the DXR Raman Microscope (Thermo Scientific, USA), which was equipped with a laser wavelength of 532 nm. To obtain a good signal-to-noise ratio, the necessary laser power of 1.5 mW was used. The electrical resistivity was measured along in-plane direction using a colinear four-probe configuration in the temperature range of 20 – 400 K. Specific heat capacity of the sample was carried out by using PPMS system in the temperature range of 20 – 300 K. For the STM study, a single crystal InSe sample was transferred into the home-built low-temperature STM system (base pressure of $\sim 7 \times 10^{-11}$ Torr) and cleaved *in-situ* to obtain clean surfaces. Tungsten tips

were prepared via electrochemical etching and cleaned with electron beam heating inside the UHV chamber. STM measurements were carried out at 280 K and 80 K.

6.3 Results

Figure 6.1a shows the XRD pattern of the sample, taken on a cleaved plane at room temperature. All diffraction peaks can be indexed, corresponding to the hexagonal crystal structure of β - and ε -InSe with space group $P6_3/mmc$ (JCPDS-34-1431), and the rhombohedral crystal structure of γ -InSe with space group $R3m$ (JCPDS-42-0919). The existence of only sharp $(00l)$ -oriented peaks with the full width at half maximum of less than 0.2° is the hallmark of the high-quality single-crystalline InSe. The powder XRD pattern confirms that our sample was crystallized in a hexagonal phase since the presence of (118) peak located at 64.5° angle[9], as shown in Fig. 6.1b. The determined lattice parameters of the sample are $a = 4.012 \text{ \AA}$ and $c = 16.576 \text{ \AA}$, in agreement with previous reports[9,10]. On the other hand, no impurity peaks were observed within the detection limit of the XRD technique, confirming the high quality of our sample.

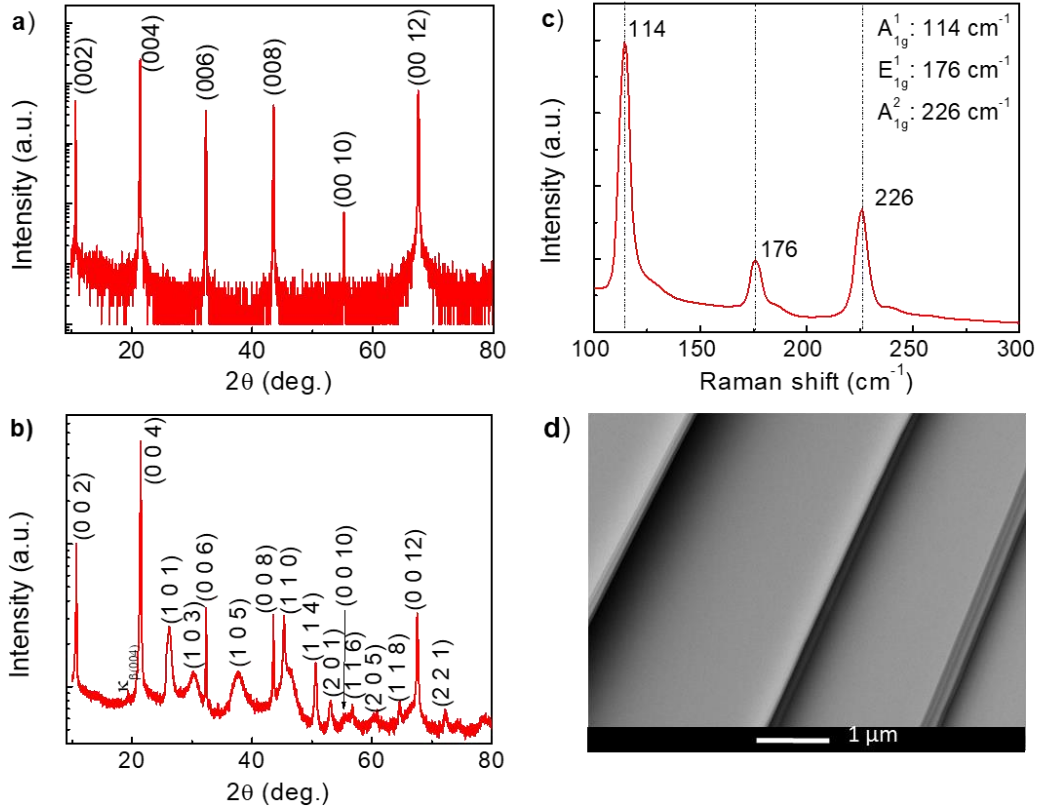


Fig. 6.1 (a) X-ray diffraction pattern taken on the β -InSe cleaved plane; (b) Powder X-ray diffraction pattern of ground β -InSe sample; (c) Raman spectrum taken on the β -InSe cleaved plane; (d) FE-SEM image of the cleaved β -InSe single crystal.

Raman spectroscopy is a powerful technique for structural and phase identifications, room temperature Raman spectroscopy has been conducted and presented in Fig. 6.1c. The Raman spectrum of InSe single-crystal exhibits three Raman active modes, namely, A_{1g}^1 mode at 114 cm^{-1} , E_{1g}^1 mode at 176 cm^{-1} , and A_{1g}^2 mode at 226 cm^{-1} . The E_{1g} mode corresponds to in-plane vibration modes, while the A_{1g} modes belong to out-of-plane vibration modes of the Se-In-In-Se planes. No Raman peak at about 202 cm^{-1} was observed, which has been known as a characteristic peak of the non-centrosymmetric ϵ and γ phases[9,17]. This observation indicates that our sample is crystallized in a single β -phase of InSe. Based on the XRD and Raman data, we conclude that we have successfully grown the high-quality β -InSe single crystal.

Figure 6.1d shows the FE-SEM image of our β -InSe single crystal. The image indicates a lamellar micro-structure of InSe, resulted from the stacking of exfoliated nano-sheets. EDS data (not shown) confirms that our sample is indeed InSe composition.

Figure 6.2a illustrates the temperature dependence of the in-plane electrical resistivity of the single-crystalline β -InSe. The electrical resistivity decreases with temperature, indicating the semiconducting behavior of our sample. Interestingly, the electrical resistivity discontinuously decreases with the temperature at 80 K and 235 K. With the cooling and heating measurements, and we observed that the discontinuity is reversible, as shown in Fig. 6.2b. The abnormal change in the electrical resistivity with temperature has been mostly attributed to phase transition (first- or second-order). On the other hand, it has been well known that defects play a dominant role in semiconductor's physical properties. Thus, the discontinuity in the transport properties of our β -InSe single crystal may also be due to a change of defects.

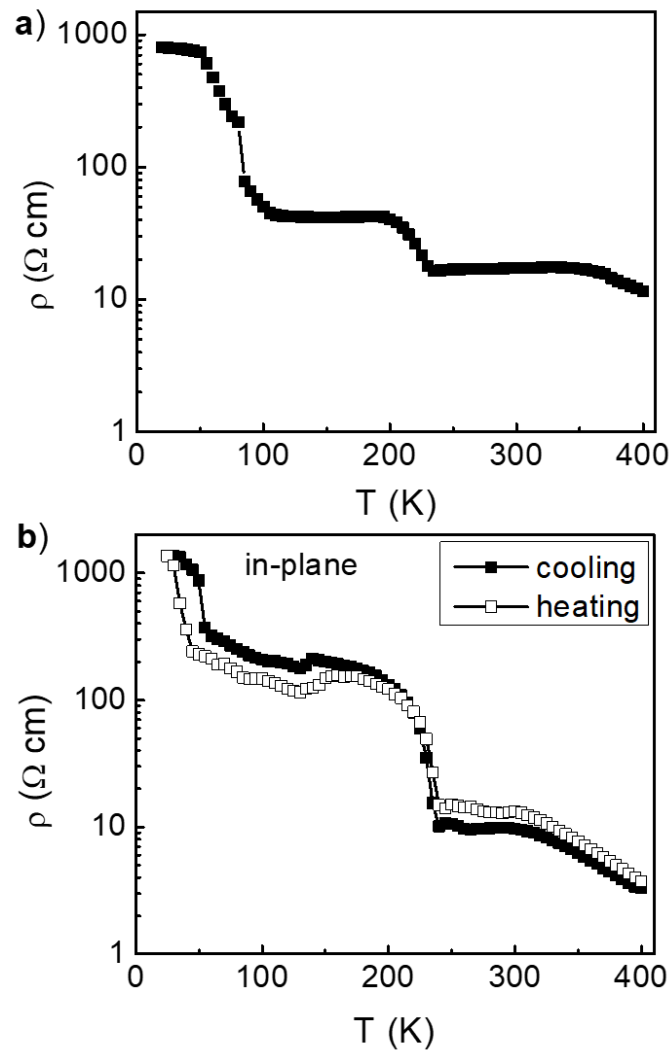


Fig. 6.2 (a) Temperature dependence of the in-plane electrical resistivity; (b) the reversibility of the in-plane electrical resistivity with the temperature of the β -InSe single crystal.

To investigate any phase transition that occurred at 80 and 235 K, we conducted temperature-dependent XRD and specific heat capacity measurements, as shown in Fig. 6.3. Figure 6.3a shows XRD patterns, taken on the sample's cleaved plane, at some selected temperatures; 150 K, 250 K, and 300 K. The sample shows almost similar XRD patterns at different temperatures. The slight variation in peak position is assigned to the thermal expansion of InSe. The temperature dependence of the specific heat capacity of the β -InSe single crystal is presented in Fig. 6.3b. The specific heat capacity continuously varies with temperature. Thus, InSe has

no phase transition in the investigated temperature range. These observations indicate that the discontinuity in the temperature-dependent in-plane electrical resistivity is not originated from the first/second-order phase transition.

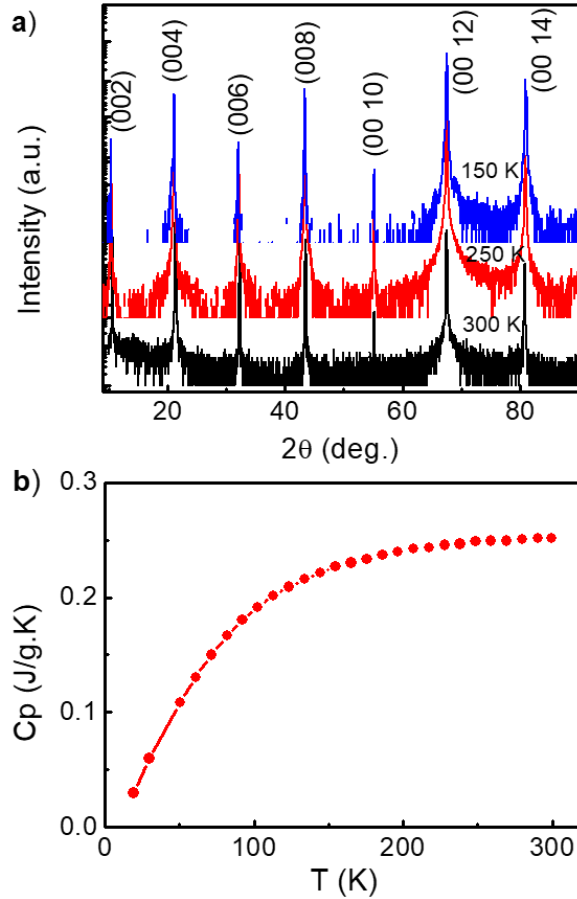


Fig. 6.3 Temperature dependence of (a) XRD patterns taken on the β -InSe cleaved plane and (b) specific heat capacity of the β -InSe single crystal.

To further clarify the discontinuous change in the in-plane electrical resistivity at 235 K and 80 K, we carried out a microscopic study on the β -InSe single crystal using a STM operating at 280 K and 80 K under an ultra-high vacuum environment ($<10^{-10}$ Torr). The sample was cleaved *in-situ* to obtain a clean surface of the β -InSe single crystal. Figure 6.4a exhibits a typical STM topographic image for the β -InSe single crystal at 280 K. The spots indicate Se atoms, while In atoms located underneath are invisible. As shown in the STM image, there are dark areas present on the surface. Figure 6.4a also shows a high-resolution STM image at the

atomistic scale of a typical dark area, marked by a black square. The size of the dark area is about 5 nm. Inside this area, Se atoms are observed at lower positions compared to surrounding Se atoms. This observation can only be understood as the missing underneath atoms in the Se-In-In-Se tetra layer, i.e., In atoms. Therefore, these dark areas represent In multi-vacancies. Interestingly, when the sample is cooled down to 80 K, the defects are eliminated and become smaller, as presented in Fig. 6.4b. The typical size of the defects is less than 3 nm at 80 K. Note that the STM images have been scanned at the same broad area at each temperature. This change of defects may be due to the movement of In interstitial atoms located in the sample from high energy interstitial positions to lower energy positions at In multi-vacancies when the temperature decreases. This hypothesis is possible because of the weak In-Se bond, which allows In atoms to be easily removed or added when the bond is broken by thermal energy. It has been reported that In interstitial is a source of the n-type characteristic in InSe[24]. We believe that the number of In interstitials is significant in our sample since it shows a negative Seebeck coefficient (Supplementary Fig. 6. S1). We attributed this defect evolution under temperature change as a reason for the discontinuity in the in-plane electrical resistivity of β -InSe single crystal, mentioned above.

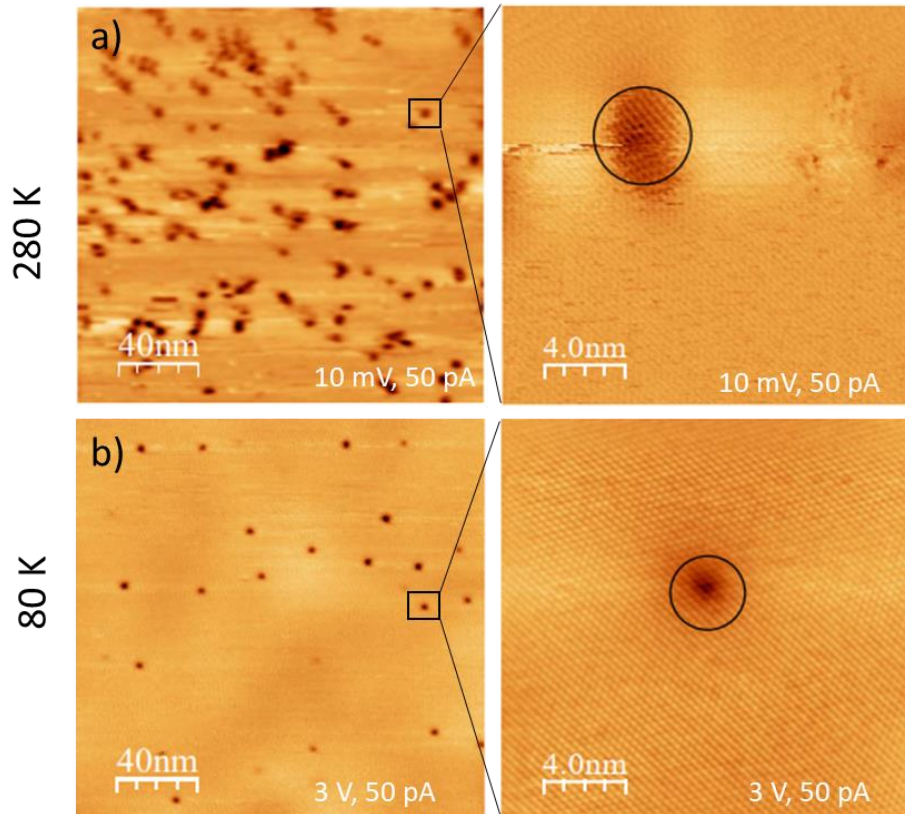


Fig. 6.4 STM images taken on the cleaved plane of the β -InSe single crystal and high-resolution STM image taken at one of the defects (marked with a dotted ellipse) at (a) 280 K and (b) 80 K.

Figure 6.5 shows STM images of the sample taken at the same positions using the same scanning conditions at 280 and 80 K. As shown in the figure, and the surface shows many different images between the first and the second scan (Fig. 6.5a and 6.5b). Figure 6.5b shows an abnormal change of exfoliated edges marked by black dash lines. As shown in the right figure, the relative distance between edges decreases, and the upper edge becomes bright. Figure 6.5c and 6.5d show high-resolution STM images at defects position at 280 and 80 K, respectively. The contrast at defect position changes, indicating the change in number In missing atoms, leading to a change in Se atoms' height. This change may be attributed to the movement of In interstitial atoms, mentioned above, under applied bias voltage. However, we cannot explain the movement of exfoliated edges at this moment.

Based on the above observations, we conclude that β -InSe is an unstable material under a temperature change or an applied bias voltage.

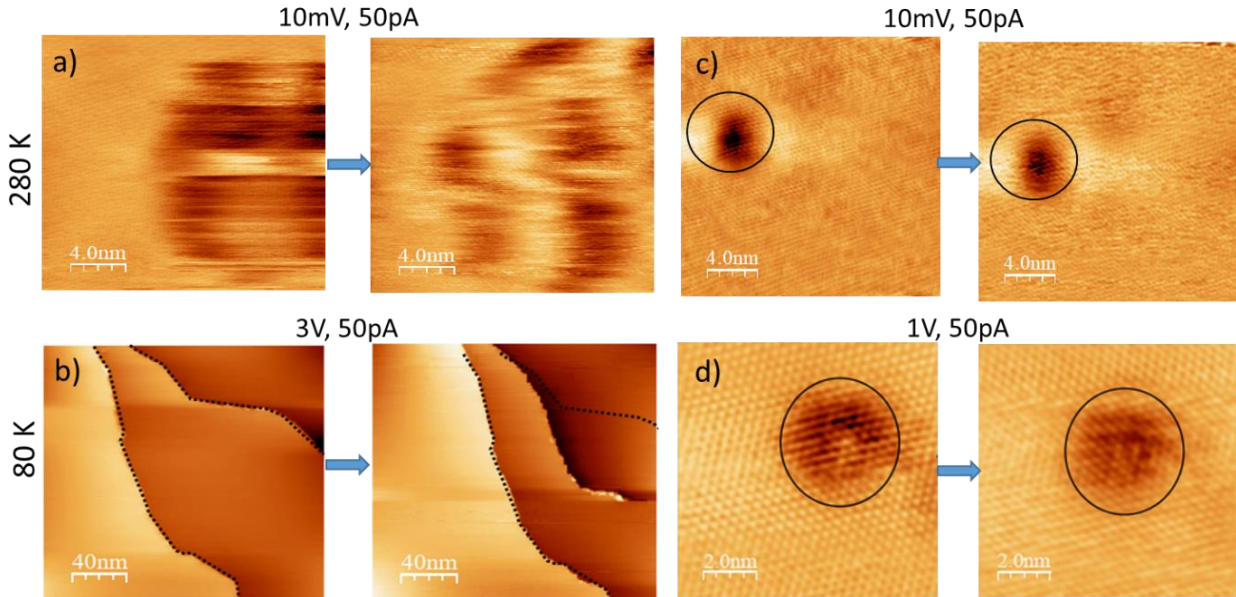


Fig. 6.5 STM images of sample taken at same positions using the same scanning conditions at (a) 280 K ($V = 10$ mV, $I_t = 50$ pA); (b) 80 K ($V = 3$ V, $I_t = 50$ pA); (c) 280 K ($V = 10$ mV, $I_t = 50$ pA); and (d) 80 K ($V = 1$ V, $I_t = 50$ pA).

6.4 Conclusion

In conclusion, the high-quality single-crystalline β -InSe was successfully grown by using the temperature gradient technique. We have provided insight investigations on the stability of the β -InSe single crystal. Scanning tunneling microscopy (STM) studies demonstrated an un-stability characteristic of β -InSe single crystal under an applied bias voltage and a change of temperature due to the weak In-Se bonds. This un-stability characteristic of β -InSe was attributed to the discontinuity in its transport property. More detail about the un-stability characteristic of β -InSe will be discussed. By this work, we temporarily conclude that β -InSe is an unstable material that is good for InSe-based devices, concerning the electric field or temperature change such as FETs, thermoelectric modules, etc., as well as for understanding intrinsic properties of InSe.

6.5 Supplementary figures

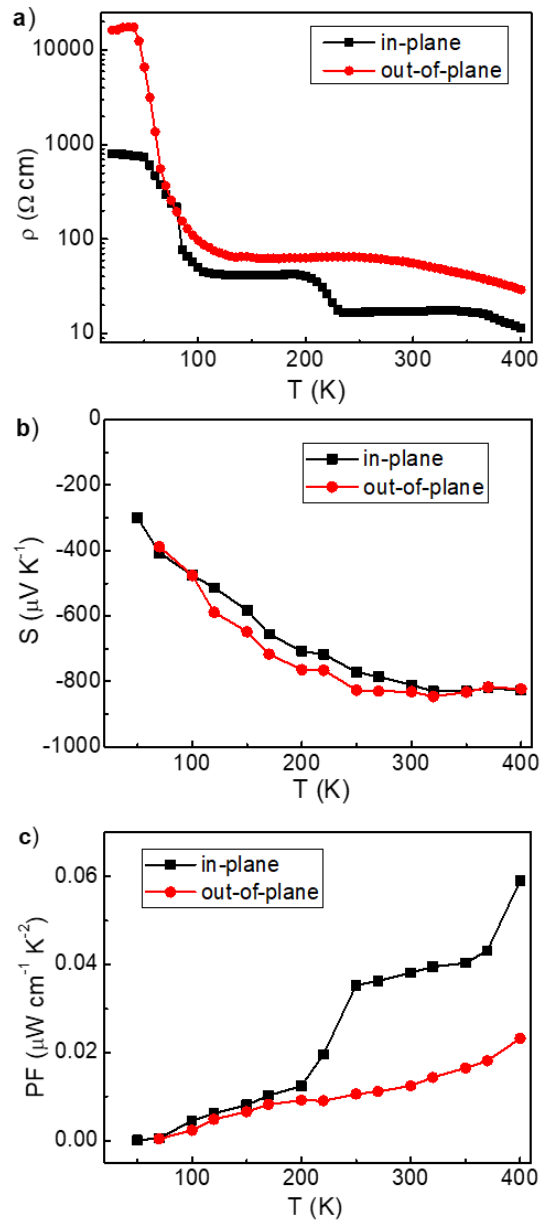


Fig. S6.1 Temperature dependence of the in-plane and out-of-plane (a) electrical resistivity, (b) Seebeck coefficient, and (c) power factor of the β -InSe single crystal.

6.6 References

- [1] S. Lebègue, O. Eriksson, Electronic structure of two-dimensional crystals from ab initio theory, Phys. Rev. B - Condens. Matter Mater. Phys. 79 (2009) 4–7. <https://doi.org/10.1103/PhysRevB.79.115409>.

- [2] B. Radisavljevic, A. Radenovic, J. Brivio, V. Giacometti, A. Kis, Single-layer MoS₂ transistors, *Nat. Nanotechnol.* 6 (2011) 147–150. <https://doi.org/10.1038/nnano.2010.279>.
- [3] W.C. Tan, Y. Cai, R.J. Ng, L. Huang, X. Feng, G. Zhang, Y.W. Zhang, C.A. Nijhuis, X. Liu, K.W. Ang, Few-Layer Black Phosphorus Carbide Field-Effect Transistor via Carbon Doping, *Adv. Mater.* 29 (2017) 1–7. <https://doi.org/10.1002/adma.201700503>.
- [4] W.S. Yun, S.W. Han, S.C. Hong, I.G. Kim, J.D. Lee, Thickness and strain effects on electronic structures of transition metal dichalcogenides: 2H-MX₂ semiconductors (M = Mo, W; X = S, Se, Te), *Phys. Rev. B - Condens. Matter Mater. Phys.* 85 (2012) 1–5. <https://doi.org/10.1103/PhysRevB.85.033305>.
- [5] Y. Ding, Y. Wang, J. Ni, L. Shi, S. Shi, W. Tang, First principles study of structural, vibrational and electronic properties of graphene-like MX₂ (M=Mo, Nb, W, Ta; X=S, Se, Te) monolayers, *Phys. B Condens. Matter.* 406 (2011) 2254–2260. <https://doi.org/10.1016/j.physb.2011.03.044>.
- [6] D.A. Bandurin, A. V. Tyurnina, G.L. Yu, A. Mishchenko, V. Zólyomi, S. V. Morozov, R.K. Kumar, R. V. Gorbachev, Z.R. Kudrynskyi, S. Pezzini, Z.D. Kovalyuk, U. Zeitler, K.S. Novoselov, A. Patané, L. Eaves, I. V. Grigorieva, V.I. Fal'Ko, A.K. Geim, Y. Cao, High electron mobility, quantum Hall effect and anomalous optical response in atomically thin InSe, *Nat. Nanotechnol.* 12 (2017) 223–227. <https://doi.org/10.1038/nnano.2016.242>.
- [7] A. Politano, G. Chiarello, R. Samnakay, G. Liu, B. Gürbulak, S. Duman, A.A. Balandin, D.W. Boukhvalov, The influence of chemical reactivity of surface defects on ambient-stable InSe-based nanodevices, *Nanoscale.* 8 (2016) 8474–8479.

<https://doi.org/10.1039/c6nr01262k>.

- [8] M. Küpers, P.M. Konze, A. Meledin, J. Mayer, U. Englert, M. Wuttig, R. Dronskowski, Controlled Crystal Growth of Indium Selenide, In_2Se_3 , and the Crystal Structures of α - In_2Se_3 , *Inorg. Chem.* 57 (2018) 11775–11781. <https://doi.org/10.1021/acs.inorgchem.8b01950>.
- [9] I. Grimaldi, T. Gerace, M.M. Pipita, I.D. Perrotta, F. Ciuchi, H. Berger, M. Papagno, M. Castriota, D. Pacilé, Structural investigation of InSe layered semiconductors, *Solid State Commun.* 311 (2020) 113855. <https://doi.org/10.1016/j.ssc.2020.113855>.
- [10] S. Lei, L. Ge, S. Najmaei, A. George, R. Kappera, J. Lou, M. Chhowalla, H. Yamaguchi, G. Gupta, R. Vajtai, A.D. Mohite, P.M. Ajayan, Evolution of the electronic band structure and efficient photo-detection in atomic layers of InSe, *ACS Nano.* 8 (2014) 1263–1272. <https://doi.org/10.1021/nn405036u>.
- [11] J. Felton, J. Felton, E. Blundo, S. Ling, J. Glover, Z.R. Kudrynskyi, O. Makarovskiy, Z.D. Kovalyuk, E. Besley, G. Walker, A. Polimeni, A. Patané, The interaction of hydrogen with the van der Waals crystal γ -InSe, *Molecules.* 25 (2020) 1–16. <https://doi.org/10.3390/molecules25112526>.
- [12] G. Han, Z.G. Chen, J. Drennan, J. Zou, Indium selenides: Structural characteristics, synthesis and their thermoelectric performances, *Small.* 10 (2014) 2747–2765. <https://doi.org/10.1002/sml.201400104>.
- [13] X. Hou, S. Chen, Z. Du, X. Liu, J. Cui, Improvement of the thermoelectric performance of InSe-based alloys doped with Sn, *RSC Adv.* 5 (2015) 102856–102862. <https://doi.org/10.1039/c5ra23023c>.

- [14] M. Alidoosti, D.N. Esfahani, R. Asgari, Charge density wave and superconducting phase in monolayer InSe, (2020) 1–10.
- [15] H. Henck, D. Pierucci, J. Zribi, F. Bisti, E. Papalazarou, J.C. Girard, J. Chaste, F. Bertran, P. Le Fèvre, F. Sirotti, L. Perfetti, C. Giorgetti, A. Shukla, J.E. Rault, A. Ouerghi, Evidence of direct electronic band gap in two-dimensional van der Waals indium selenide crystals, *Phys. Rev. Mater.* 3 (2019) 1–6. <https://doi.org/10.1103/PhysRevMaterials.3.034004>.
- [16] S. Sucharitakul, N.J. Goble, U.R. Kumar, R. Sankar, Z.A. Bogorad, F.C. Chou, Y.T. Chen, X.P.A. Gao, Intrinsic Electron Mobility Exceeding $10^3 \text{ cm}^2/(\text{V s})$ in Multilayer InSe FETs, *Nano Lett.* 15 (2015) 3815–3819. <https://doi.org/10.1021/acs.nanolett.5b00493>.
- [17] Z. Chen, J. Biscaras, A. Shukla, A high performance graphene/few-layer InSe photo-detector, *Nanoscale*. 7 (2015) 5981–5986. <https://doi.org/10.1039/c5nr00400d>.
- [18] F.H.L. Koppens, T. Mueller, P. Avouris, A.C. Ferrari, M.S. Vitiello, M. Polini, Photodetectors based on graphene, other two-dimensional materials and hybrid systems, *Nat. Nanotechnol.* 9 (2014) 780–793. <https://doi.org/10.1038/nnano.2014.215>.
- [19] J.Y. Emery, L. Brahim-Ostmane, C. Hirlimann, A. Chevy, Reflection high-energy electron diffraction studies of InSe and GaSe layered compounds grown by molecular beam epitaxy, *J. Appl. Phys.* 71 (1992) 3256–3259. <https://doi.org/10.1063/1.350972>.
- [20] C. Julien, I. Samaras, M. Tsakiri, P. Dzwonkowski, M. Balkanski, Lithium insertion in InSe films and applications in microbatteries, *Mater. Sci. Eng. B.* 3 (1989) 25–29. [https://doi.org/10.1016/0921-5107\(89\)90174-8](https://doi.org/10.1016/0921-5107(89)90174-8).

- [21] J.H. Park, M. Afzaal, M. Helliwell, M.A. Malik, P. O'Brien, J. Raftery, Chemical Vapor Deposition of Indium Selenide and Gallium Selenide Thin Films from Mixed Alkyl/Dialkylselenophosphorylamides, *Chem. Mater.* 15 (2003) 4205–4210. <https://doi.org/10.1021/cm0310420>.
- [22] A. Chevy, A. Gousskov, J.M. Besson, Growth of crystalline slabs of layered InSe by the Czochralski method, *J. Cryst. Growth.* 43 (1978) 756–759. [https://doi.org/10.1016/0022-0248\(78\)90157-4](https://doi.org/10.1016/0022-0248(78)90157-4).
- [23] C. De Blasi, G. Micocci, S. Mongelli, A. Tepore, Large InSe single crystals grown from stoichiometric and non-stoichiometric melts, *J. Alloys Compd.* 57 (1982) 482–486. <https://doi.org/10.1017/CBO9781107415324.004>.
- [24] K.J. Xiao, A. Carvalho, A.H. Castro Neto, Defects and oxidation resilience in InSe, *Phys. Rev. B.* 96 (2017) 1–8. <https://doi.org/10.1103/PhysRevB.96.054112>.

Chapter 7. Conclusions

The single-phase undoped and Ni-, Co-, and Zn-doped poly-crystalline CuAgSe, the single crystalline α -In₂Se₃, and β -InSe, which were grown by using the temperature gradient technique, were carried out. The carrier type of CuAgSe was switched from the native n-type to the p-type by increasing the soaking time during growth. In contrast, when Ni, Co, and Zn were doped into the host lattice, the samples always retained their n-type behavior. The maximum ZT value of 0.69 (0.56) at 623 K (673 K) in undoped n-type (p-type) CuAgSe was obtained. Zn is a promising dopant for n-type CuAgSe with a ZT value of 0.68 at 623 K. The effects of the doping concentration and the soaking time on thermoelectric properties will be studied in the next steps of the research. It is also found that a large anisotropic transport property in the α -In₂Se₃ single crystal was approximately 490,000 at 20 K, 43,300 at 300 K, and 3,650 at 400 K. This huge anisotropy in transport phenomena could be attributed to the anisotropic activation energy and huge anisotropic electron mobility between two directions. Additionally, a modification of the cleaved surface and defects by a temperature change or an applied voltage was observed in β -InSe, indicating an un-stability characteristic of β -InSe due to the weak In-Se bond in the quadruple slab. The un-stability characteristic of β -InSe leads to a discontinuity variation of electrical resistivity with temperature. I will continue this work to find the origination of un-stability characteristics of β -InSe. Also, optimizing the TE performance for the α -In₂Se₃ and β -InSe single crystals is necessary for future work.